LORENZ CENTER
MASSACHUSETTS INSTITUTE OF TECHNOLOGY

Assessing the Risk of Compound Hazards from Hurricanes in a Changing Climate

Prepared by: Ali Sarhadi
Supervised by: Kerry Emanuel
Date: July 31, 2024

Contents

Report 1

Contribution of Climate Change to Hurricane Compound Hazards and Monetary Losses in New York City

1 Overview

Tropical Cyclones (TCs) and Extratropical Cyclones (ETCs) cause significant monetary losses in the eastern part of the United States every year. The effect of anthropogenic warming on these storms has led to changes in the risk and damages associated with them in recent decades, and it is expected to intensify in the future. This research aims to develop a physics-based methodology to better understand the extent to which climate change has altered and will change the risk of multiple hazards associated with these storms, including compound surge and rainfall-driven flooding and high-speed surface winds.

The first section of the research focuses on developing a physics-based methodology to quantify the risk of compound flooding from TCs and ETCs in current and future decades in New York City (NYC). Due to the limited availability of instrumental hurricane records in NYC, a physics-based statistical-deterministic downscaling approach is used to estimate the climatology and evolution of hurricanes under both current and future climates. A high-resolution statistical-deterministic tropical cyclone model is employed, which uses time-evolving boundary conditions derived from the output data of General Circulation Models (GCMs) to downscale synthetic hurricanes. By generating a large set of synthetic hurricanes that are consistent with the ERA-Interim reanalysis and GCM climates, the climatology and evolution of hurricanes in NYC are estimated. The research also uses dynamically downscaled extratropical cyclones and their main drivers to simulate compound flooding. Using hydrodynamic models forced by large sets of synthetic TCs from four Coupled Model Intercomparison Project Phase 6 (CMIP6) climate models and ETC events downscaled using Weather Research and Forecasting (WRF) model forced by CMIP5 simulations, the contribution of the primary drivers to increasing risk of spatially-varying compound flooding is quantified in current and future warming decades in NYC.

The second section of the research uses the same physics-based model to simulate high spatial resolution maximum wind speed during the landfalling of historical hurricanes. A computational intelligence model is developed using conditional random field theory to optimize wind-driven damage functions in grid cells with the size of 5 in 5 km in NYC. By applying these optimized wind-driven damage functions on future synthetic hurricanes' maximum wind speed, the monetary losses from maximum sustained wind of hurricanes are projected in the future warming climate. By using a probabilistic model, the risk of monetary losses from hurricanes' wind speed in the future warming climate is quantified to the portfolio of Homesite in the NYC area.

Overall, this research presents a physics-based methodology to better understand the risks of multiple hazards from TCs and ETCs in a warming climate. The study demonstrates that this methodology can be used to quantify the multiple hazards involved with TCs and ETCs and the associated losses caused by these storms in the current and future warming decades in NYC. Although the study does not quantify the effect of climate change on the losses arising from compound flooding, it does provide insight into the risk of monetary losses from high-speed winds of these storms. As an insurance company, Homesite can use these results to better project the potential impacts of TCs and ETCs in a warming climate to develop new policies, set premiums, and respond to claims related

to these multiple hazards from these intensifying storms in a future warming climate.

2 Risk Assessment of Compound Flooding from tropical and extratropical cyclones

TCs and ETCs are among the deadliest and most destructive natural hazards, causing substantial fatalities and economic damages (US$26 billion from TCs and US$2 billion from winter ETCs each year in the United-States alone) Bakkensen and Mendelsohn [2019], Smith et al. [2020]. Among multiple hazards associated with these cyclones, many of the fatalities and much of the damage are caused by coastal flooding from storm surge (generated by high-speed winds), and inland flooding rain-driven in coastal and inland communities Zhang et al. [2018], Rappaport [2014]. During destructive cyclones, each of these flooding hazards may play a role, either separately or in combination. For example, strong winds during Hurricane Sandy in October 2012 caused devastating surge-driven flooding across heavily populated coastal areas in New York City (NYC), resulting in more than $64 billion (2017 USD) in damages Strauss et al. [2021]. Hurricane Harvey in August 2017, instead, stalled over an inland area and poured an unprecedented heavy rainfall for many days over the Houston metropolitan area, causing catastrophic inland flooding and costing $125 billion (2017 USD) in damages Zhang et al. [2018]. However, storm surge driven flooding may co-occur with inland heavy rainfall-driven flooding resulting in a compound flooding event, whose destructive potential is often much greater than that of either of the individual flooding hazards. During Hurricane Katrina, a destructive category 5 TC, a significant storm surge coincided with record-breaking heavy inland rainfall along the Gulf coast. The compound flooding devastated coastal areas in Louisiana and caused one of the costliest natural disasters in U.S. history, with at least 1,833 deaths and more than $160 billion in damages (adjusted to 2017 USD to compare with the rainfall dominant Hurricane Harvey) Patricola and Wehner [2018]. Recently, a destructive compound flooding event during Hurricane Ian had devastating impact in western Florida, and cost between $50 billion and $65 billion in insured losses. In densely populated coastal areas, such flood hazard compounding in TCs or ETCs can thus lead to extreme impacts even if, individually, these flooding hazards are not extreme Wahl et al. [2015].

Past and future changes in the risk of compound flooding from these cyclones depend on how the warming atmosphere and oceans have influenced and will influence the structural characteristics, intensity, frequency, and movement of these cyclones Emanuel [2021b]. There is confidence that anthropogenic warming has intensified the activity and destructiveness of major TCs in the North Atlantic basin in recent decades Bender et al. [2010], Emanuel [2005, 2021a, 2013]. This trend is expected to accelerate in the future as ocean temperatures increase Trenberth et al. [2018], Saunders and Lea [2008], Emanuel [2005], Huang et al. [2015], and the troposphere warms Patricola and Wehner [2018], Emanuel [2021b], Walsh et al. [2015], Priestley and Catto [2022]. Despite our understanding of the future changes of multiple individual drivers of TC and ETC flooding under a warming climate —including intensifying rainfall, poleward migration, slowdown of cyclone translation speed, Sea Level Rise (SLR), and deceleration of ETCs due to atmospheric blocking Emanuel [2021b], Kossin et al. [2014], Booth et al. [2021], Strauss et al. [2021]—quantifying the risk of compound flooding in response to these changes in highly populated

coastal cities, like NYC, remains elusive.

In recent years, much effort has been devoted to modeling the complex hydrodynamics of compound flooding from TCs and ETCs and their corresponding risk in highly populated coastal areas. The majority of these studies model risk statistically, based on individual predictors such as surge height and rainfall intensity verified using local observations Gori et al. [2021], Wahl et al. [2015]. Recent studies have introduced physically based computational models to supplement statistical risk assessment approaches Garner et al. [2017], Reed et al. [2015], Emanuel [2017], Lin et al. [2016], Marsooli et al. [2019], Gori et al. [2022], Bates et al. [2021]. Most of these have been used to predict rainfall, not flooding, or focus on surge-only flooding. In this study, we introduce a physically based computational approach to model compound flooding and address how human-induced climate change and SLR may affect flooding and flood risk in NYC from TCs and ETCs.

First, we estimate the climatology and evolution of TCs in the current and future climates by using a physics-based statistical-deterministic downscaling approach Emanuel et al. [2008]. This method generates a large number of synthetic TCs consistent with the ERA-Interim reanalysis and General Circulation Model (GCM) climates to emulate a long record of historical and future TC events. We downscale a large set of storms from ERA-Interim reanalysis from the late 20th century (1979-1999), and the early 21st century (2000-2020) climates. We also downscale a large set of synthetic tracks from four bias corrected GCMs of the Coupled Model Intercomparison Project phase 6 (CMIP6), to represent the evolution of TCs in the current climate (2000-2014), and at the middle (2041-2060) and end of the century (2081-2100) under the SSP3 7.0 scenario. The Tropical Cyclone Rainfall (TCR) algorithm is used to estimate evolving, high spatial resolution (almost $\sim 20\ m$) hourly rainfall from the synthetic TCs in and near NYC Feldmann et al. [2019]. Second, for ETC events, we use a dynamically downscaled dataset of hourly rainfall, wind, and pressure fields over the Northeastern U.S., with 3-km spatial resolution, driven by CESM v1.0 under Representative Concentration Pathway 8.5 (RCP8.5). The downscaling data comes from convection-permitting Weather Research and Forecasting (WRF) model simulations for almost the same three climate periods Komurcu Bayraktar et al. [2018]. We then use an extensively evaluated hydrodynamic model (GeoCLAW) driven by atmospheric pressure and surface wind speed to compute surge height associated with TCs and ETCs, along a vast segment of coastline near NYC Mandli and Dawson [2014]. The hydrodynamic model also accounts for SLR from the ensemble mean of CMIP6 projections, incorporated to the model as a 'bathtub' approach (see more details on the data sets in Appendix). We then apply a pluvial hydraulic model Neal et al. [2012], driven by the simulated storm surges and downscaled heavy rainfall events simultaneously as boundary conditions. The hydraulic model then simulates high spatio-temporal resolution compound flooding during the landfalling of each synthetic TC and downscaled ETC in the current and future climates (see more details in Appendix). Finally, we quantify the extent to which changes in storm climatology and SLR from anthropogenic forcing may change the spatial risk of compound flooding events in NYC.

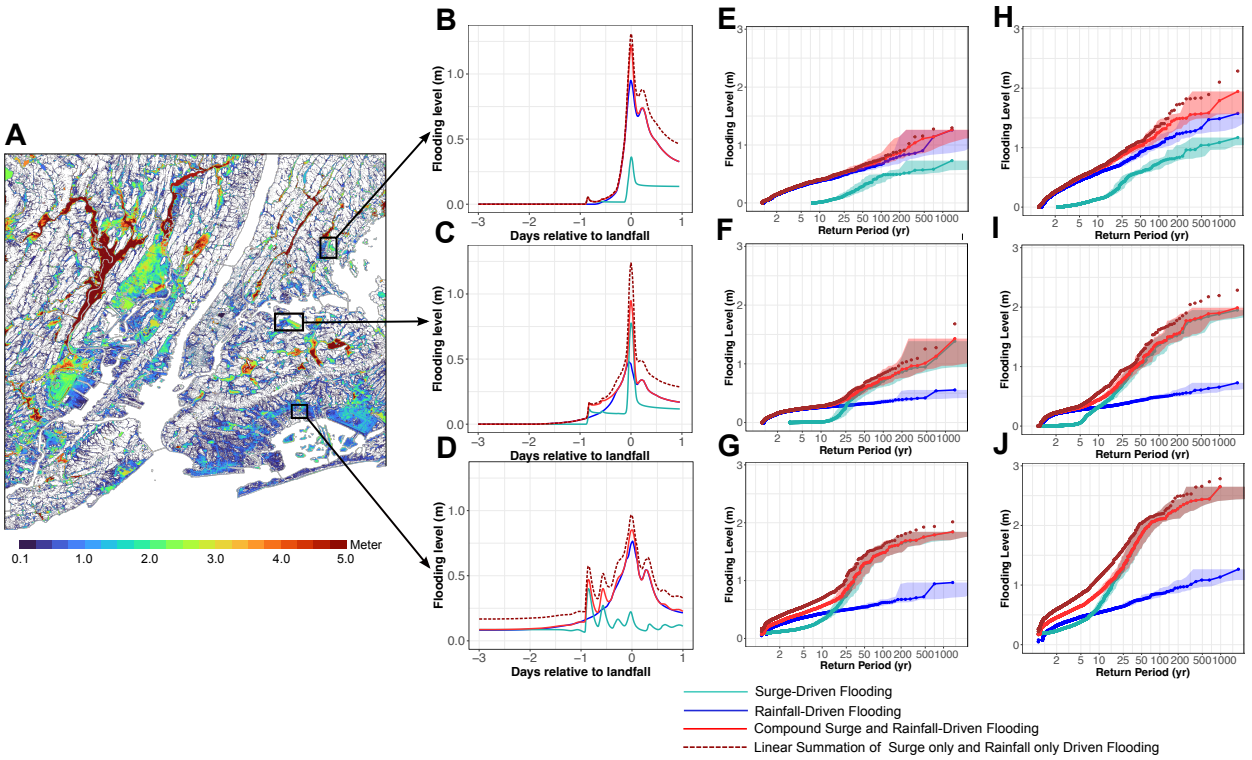

Figure 1: (A) Maximum compound flooding level for a downscaled synthetic track (#260) from CESM2 model under the current climate. (B-D) Compounding effect from nonlinear mechanical interaction between surge and rainfall driven flooding through landfalling the synthetic TC in the three depicted areas in NYC. (E-G) Flooding levels as a function of return period from the three flooding hazard sources. The results are based on synthetic TCs generated from CESM2 model over the current climate (the results are calculated based on the mean of flooding levels for each depicted area). The shading part in the figure represents sampling uncertainty bounds calculated based on the 5th and 95th percentiles of a Poisson distribution (H-J) Similar to the previous section, but for the end of the century.

2.1 Compound flooding effect

Figure 1 (A-D) compares the behavior of compound flooding with the individual surge and rainfall driven flooding in different locations in NYC (coastal and inland areas), based on the simulations from a randomly selected synthetic track in the current climate in NYC. The combination of the individual surge and rainfall driven flooding is nonlinear (Figure 1 (B-D)). This nonlinear effect depends on different factors, including the nature of the storm (whether it is wind or rainfall dominant), topography and the distance from coastline, and the lag time between surge and rainfall driven flooding. Although the contribution of surge driven flooding dominates in coastal areas, in inland areas rainfall driven flooding is the dominant factor. In both coastal and inland areas, however, the compound flooding levels are higher than the individual hazards at the time of landfalling. We also show that a linear summation of the individual surge and rainfall-driven flooding (red dashed line) cannot represent the level of compound flooding. Summing the two individual flooding levels overestimates the level of 'actual' compound flooding.

This effect of compounding will also affect risk assessments in the current and future warming climate. In assessing TC flood risk, different studies typically consider the risk of one individual hazard Lin et al. [2016, 2012], Reed et al. [2015] and may use statistical

algorithms to account for other hazard components Bates et al. [2021], Gori et al. [2022]. These approaches, however, ignore the spatiotemporal nonlinear mechanical interactions between the surge and rainfall driven flooding, which can lead to higher potential for compound flooding across the coastal and inland areas. For example, Figure 1 (E) shows that relying on only surge driven flooding in inland areas underestimates the risk of actual compound flooding up to 62.6% (51.0-61.6%) in the current climate, and up to 59.0% (55.8-56.5%) in the late 21st century for the events which occur once in 100 y (Figure 1 (H)). In coastal areas, however, relying on only rainfall driven flooding underestimates the risk of compound flooding by up to 40.0% (41.8-42.2%) in the current climate, and by up to 40.6% (39.3-41.7%) in the late 21st century for the same events (Figure 1 (G and J)). On the other hand, the linear summation of the individual surge and rainfall-driven flooding overestimates the risk of flooding, comparing to the actual compound flooding. This misestimation of the risk occurs more from the low frequency events in the upper tail in both current and future climates. Therefore, accounting for the spatiotemporal nonlinear compound effects of surge and rainfall driven flooding during landfalling and their responses in coastal and inland areas is crucial in assessing coastal flooding risk.

2.2 Sandy's compound flooding

We begin by looking at a single TC event, one that resembles Hurricane Sandy, which affected NYC in 2012. In addition to constructing a map of the flooding, we examine the individual and combined contributions of rainfall and surge to the flooding. Figure 2 summarizes this particular event, showing the maximum wind speed experienced at each point during the event (A), and the accumulated hourly rainfall from this event (B). Figures 2 (C) and (D) show, respectively, the maximum surge height, and rainfall-driven flooding from this event, while Figure 2 (E) shows the compound flooding driven by both sources. This simulated maximum compound flooding from the Sandy-like synthetic event is similar to the actual Federal Emergency Management Agency (FEMA) flood inundation record from Sandy in 2012 (Figure S1). Figure 2 (C-E) shows that the individual rainfall and surge hazards, as well as the compound hazard, may affect different areas. Figure 2 (F) also shows under-estimation of the property value exposure under different levels of flooding from the individual hazards comparing to the one from compound flooding during Hurricane Sandy. It is clear that accounting only for individual flooding hazards mis-estimates the magnitude, damage, and spatial consequences of flooding relative to compound flooding. In addition, the spatial information provided by our physics-based model, which identified the most at-risk zones, is crucial for adaptation measures and cannot be well simulated using statistical methods alone.

2.3 Tropical Cyclones compound flooding risk in today's climate

Next, we quantify the extent to which anthropogenic warming has already changed the risk of compound flooding via changes in TC climatology and SLR in and near NYC. To do so, we simulate the maximum compound flooding level from 1250 synthetic TCs downscaled from ERA-Interim reanalysis under the late 20th century climate, and another 1250 events in the climate of the early 21st century. Figure 3 (A) shows the changes in the risk of compound flooding between the late 20th century and the early 21st century. The return period is calculated as the inverse of the annual exceedance probability defined over each of the two time periods. The results show that anthropogenic warming already has increased significantly the risk for events with return periods between 2 and 20 yr in today's climate for the selected area. Sampling uncertainty prevents us from distinguishing trends at larger return periods.

Figure 3 (B) shows that climate change has increased the spatial risk of compound flooding by 100 yr return period events. The flood levels of such events have increased in inland areas by up to $\sim$0.5 m, caused mostly by more intense rainfall. However, there is a decreasing trend along the coastlines up to $\sim$-0.2 m. This decrease might be related to the decrease in the frequency or changes in tracks of intense TCs in the region, which generate lower surge height and compound flooding along the coastlines for such events in the more recent climate. A comparison of figure 3 to Figure S2, which neglects SLR, also confirms that SLR does not appear to have contributed significantly to the change in compound risk in recent years. The compound flooding results for events with return periods 25 to 500 yr are provided in Figures S3. The risk of compound flooding, especially for the low frequency events, follows a pattern similar to that of the 100 yr return period shown in Figure 3 (B), and the changes are not statistically significant in coastal areas.

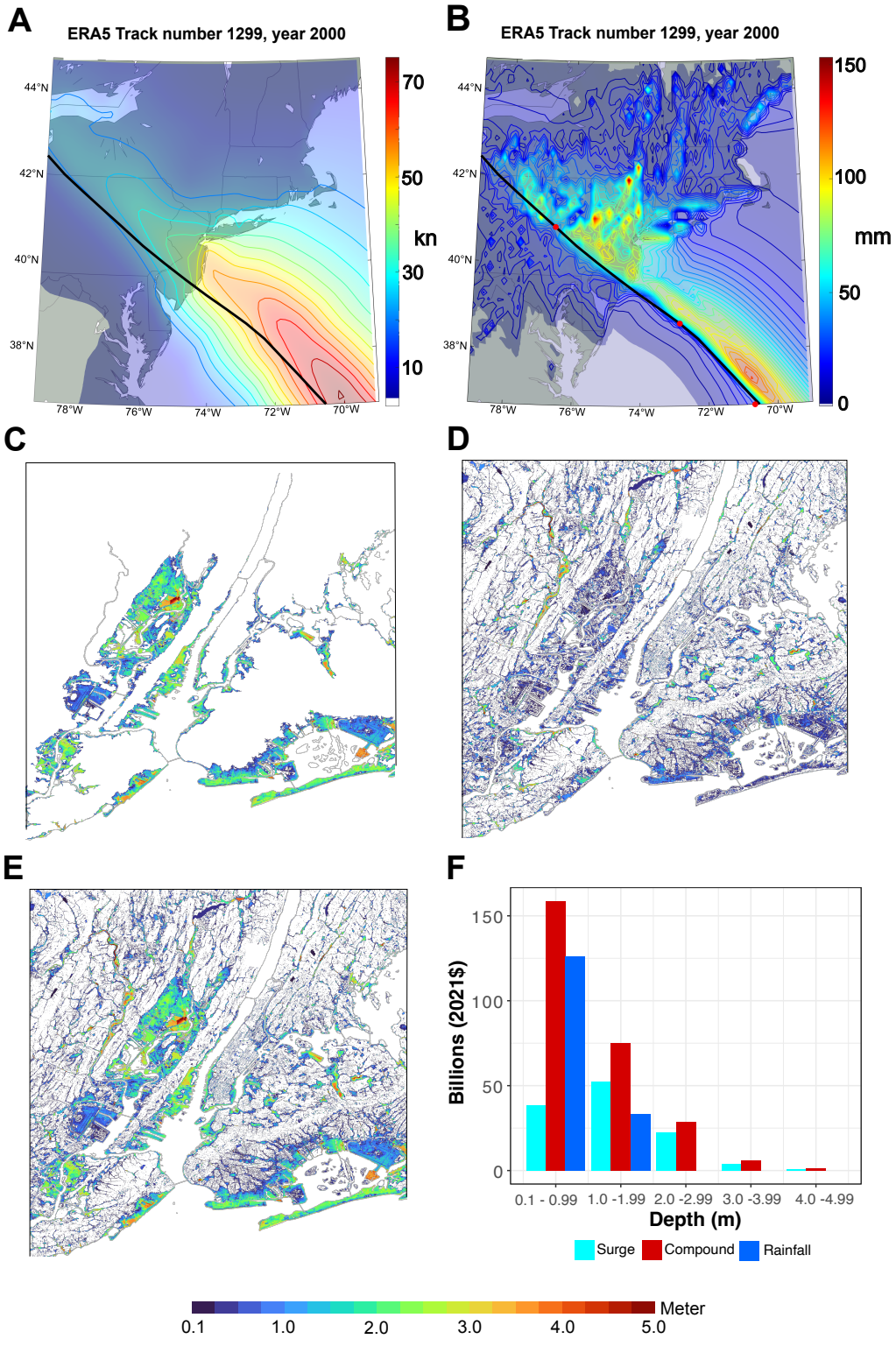

Figure 2: (A) Max. wind speed swath of a Sandy-like synthetic track (#1299) downscaled from ERA5. (B) Same as (A) but for rainfall intensity. (C) Surge driven flooding for the Sandy-like event (#1299), (D) Rainfall driven flooding for the Sandy-like event (#1299), (E) Compound surge and rainfall driven flooding for the Sandy-like event (#1299). (F) Property value exposure to different levels of flooding from each flooding hazard during Hurricane Sandy in NYC.

2.4 Future Compound flooding risk

By simulating compound flooding levels from a large set of synthetic TCs downscaled from the four climate models (i.e., CESM2, CNRM6, ECEARTH6, and UKMO6) for the current and future climates, we quantify how the risk of compound flooding may evolve. Figure 4 (A and B) shows the respective contributions to compound flooding risk intensification arising from storm climatology changes and SLR. Each curve represents the simulated TC compound flooding events generated from each of the four CMIP6 models. Based on the results, the return period of the Sandy-like event (depicted in dash-line) is about $\sim$215 yr based on the ensemble mean of the four CMIP6 climate models neglecting SLR in the current climate. Going forward in time while still neglecting changes in SLR, the return period of Sandy-like events decreases to $\sim$170 yr by the middle of the century, and to $\sim$130 yr by the end of the century. With the joint effect of changes in TC climatology and SLR, the Sandy-like event occurs around once in $\sim$150 yr in the present climate. The risk of such a damaging event will also increase and become a $\sim$65 yr event by the middle of the century, and a $\sim$30 yr storm by the end of the century. TC climatology changes arising from anthropogenic warming alone will thus increase the risk of a Sandy-like storm by up to 1.26 times by the middle of the century and 1.7 times by the end of the century, relative to the current climate. The joint contribution of TC climatology and SLR will, however, increase the risk of Sandy-like floods by up to almost 2.3 times by the middle of the century, and 5 times by the end of the century. The projected SLR alone will intensify the risk of Sandy's compound flooding by 1.05 times by the middle of the century and 3.3 times by the end of the century relative to the current climate. SLR thus makes a significant contribution to the increased risk of destructive compound flooding events from TCs.

Figure 4 (C-F) shows the contribution of each primary driver to the change in 100 yr flooding by the middle and end of the century. The results show that, by the middle of the century, anthropogenic warming will intensify the level of spatial flooding, mostly in inland areas and arising mostly from increased rainfall. A comparison between Figure 4 (C) and (D) shows the contribution of SLR to changes in compound flooding by the mid-century. For example, TC climatology change increases the spatial compound flooding level, on average, up to $\sim$0.35 m, while the joint contribution of TC changes and SLR will increase flood levels by up to $\sim$0.7 m in coastal areas.

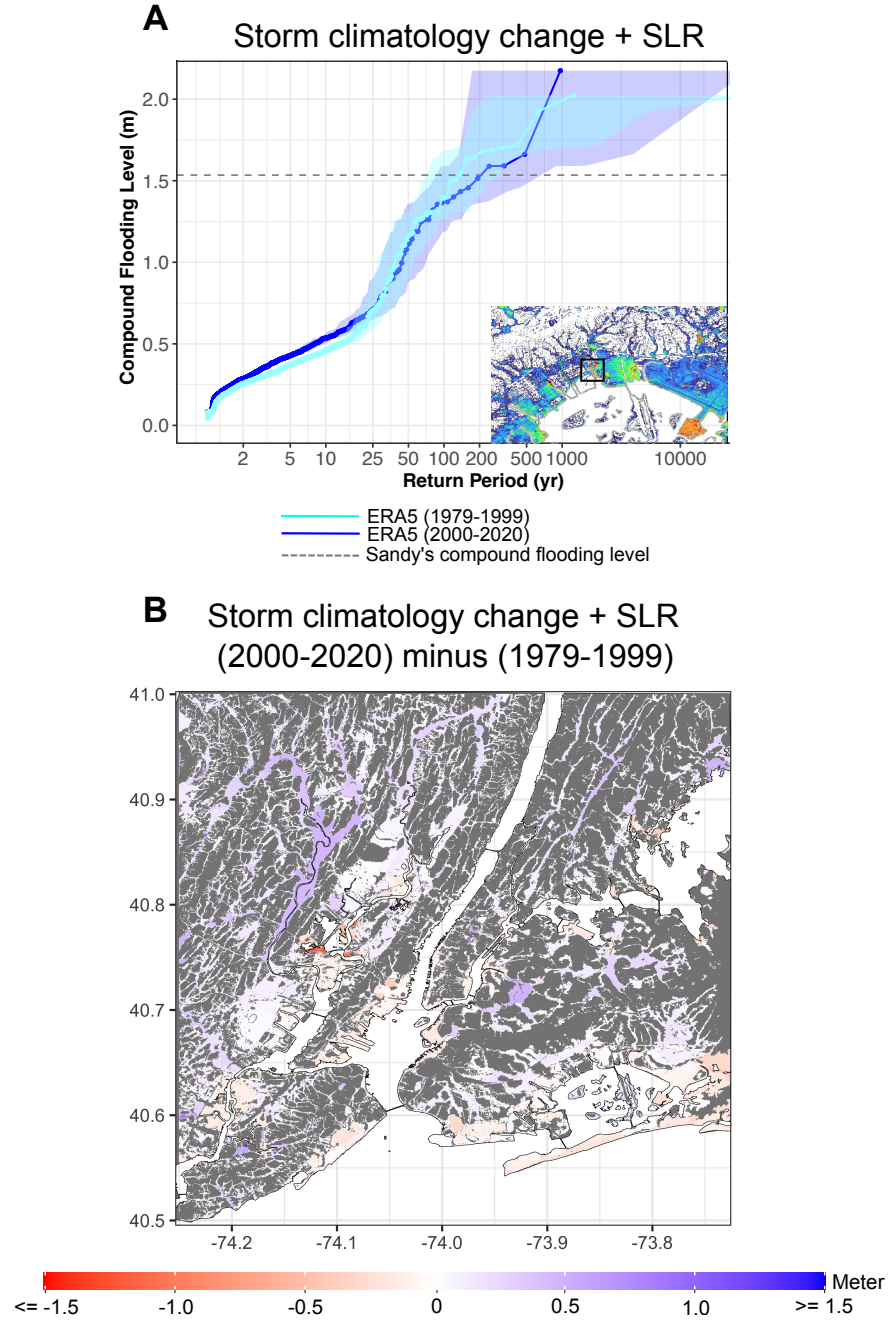

Figure 3: Impact of TC climatology change and SLR on the risk of compound flooding in today's climate (2000-2020) relative to the end of the 20th century (1979-1999) in NYC. (A) TC compound flooding level as a function of return period, for today's climate and the end of the 20th century (the results are calculated based on the mean of compound flooding for the depicted area). Each line shows compound flooding results from synthetic TCs generated from re-analysis ERA5 over each time period. The shading in the figure represents sampling uncertainty bounds calculated based on the 5th and 95th percentiles of a Poisson distribution. The gray dashed line shows the mean of Sandy compound flooding level, calculated from the Sandy-like event (#1299) for the depicted area (shown in a black rectangle). (B) Impact of TC climatology change and SLR on the spatial risk of 100 *yr* return period compound flooding events in today's climate relative to the late 20th century (blue color shows increasing trend, and red color shows decreasing trend).

Similarly, TC climatology changes increase rainfall intensity by the end of century, resulting in more increased flooding in inland areas, especially along the Passaic River. This contribution alone increases the level of spatial compound flooding by up to almost $\sim$0.5 m by the end of the century in coastal areas (Figure 4-E). The joint impact including SLR, however, increases the level of flooding on average by up to $\sim$1.3 m in the majority of coastal areas by the end of the century (Figure 4-F). These results show the significant impact of SLR in increasing flood risk in NYC. The contributions of both drivers to increasing flood risk for other return periods from 50 yr to 500 yr are given in Figure S(4-6).

2.5 Compound flooding risk of ETCs

Figure 5 (A and B) show the contributions of ETC climatology changes and SLR to changes in compound flooding risk over the depicted area. The results cover only high frequency events (return periods of 20 yr or less), due to the limited number of ETCs available in the downscaled data. With ETC climatology change only, the risk of compound flooding is projected to increase 1.7 times by the middle of the century, and 2.4 times more by the end of the century. The combined impact of ETC climatology change and SLR will, however, increase the risk by a factor of about 5.4 by the middle of the century, and about 9 by the end of the century. Considering only SLR, the risk increases by a factor of 3.7 by the middle of the century, and by 6.6 by the end of the century. In this case, SLR is more important than changes in ETC climatology change in driving increased flooding.

The impacts of ETC storm changes and SLR on the spatial risk of compound flooding for 15 yr return period events are shown in Figure 5 (C and D) for the middle of the century, and in Figure 5 (E and F) for the end of the century. The results indicate the dominant role of SLR in increasing the risk of ETC-related compound flooding of coastal areas. The results for the impact of ETC climatology changes and SLR on the risk of compound flooding for other return periods (5 yr to 10 yr) are shown in Figure S(7-8).

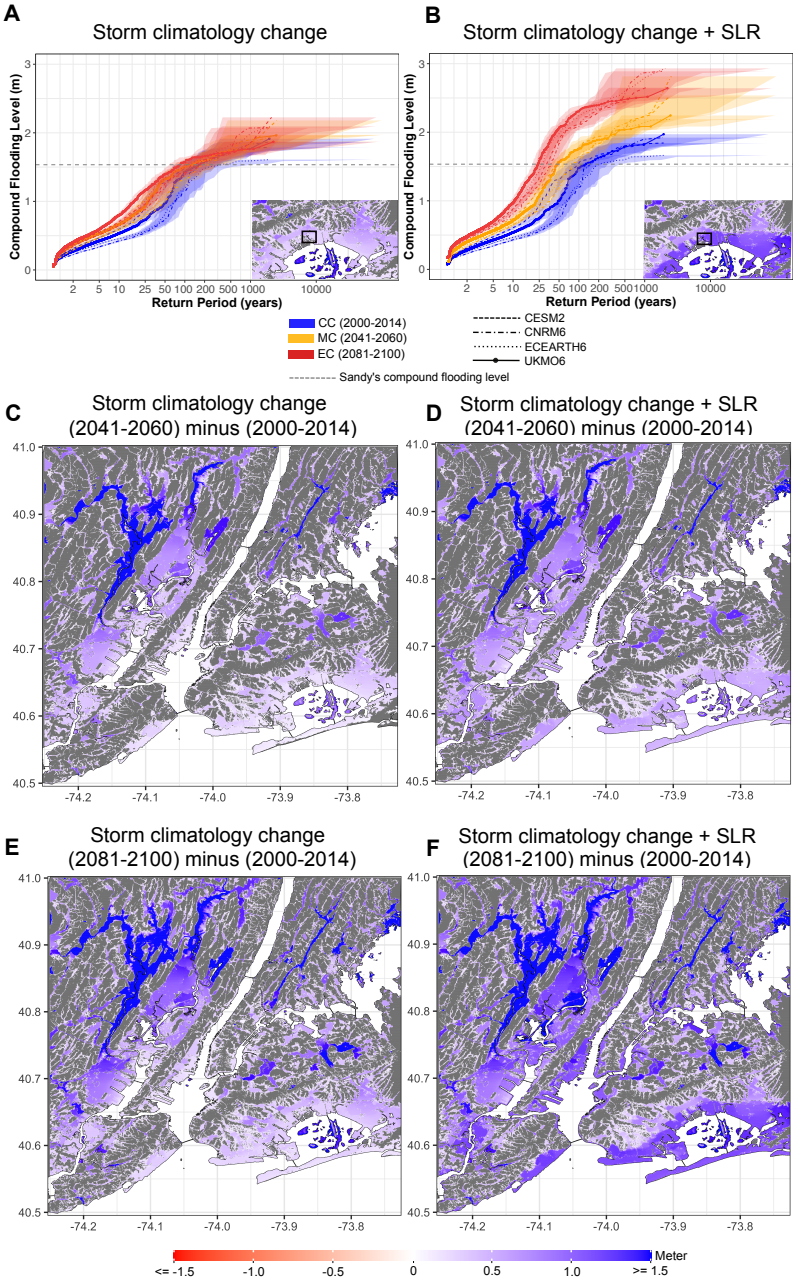

Figure 4: Impact of future TC climatology change and SLR on the risk of compound flooding in NYC. (A) Contribution of TC climatology change alone, and (B) contribution of both TC climatology change and SLR to the future risk of compound flooding. The results are based on the mean of compound flooding level (calculated for the depicted coastal area) in the current and future climates. Each line shows the results from synthetic TCs downscaled from each climate model in the current and future climates. The shading in the figure represents confidence intervals calculated based on the 5th and 95th percentiles of a Poisson distribution for each model. The gray dashed line shows the magnitude of compound flooding from Sandy (calculated from the Sandy-like event (#1299) for the depicted area. (C and D) Impact of TC climatology change and SLR on the spatial risk of 100 yr return period compound flooding by the middle of the century relative to the current climate, and (E and F) by the end of the century relative to the current climate. Note that the spatial results are based on the ensemble mean of the four CMIP6 climate models calculated in each climate.

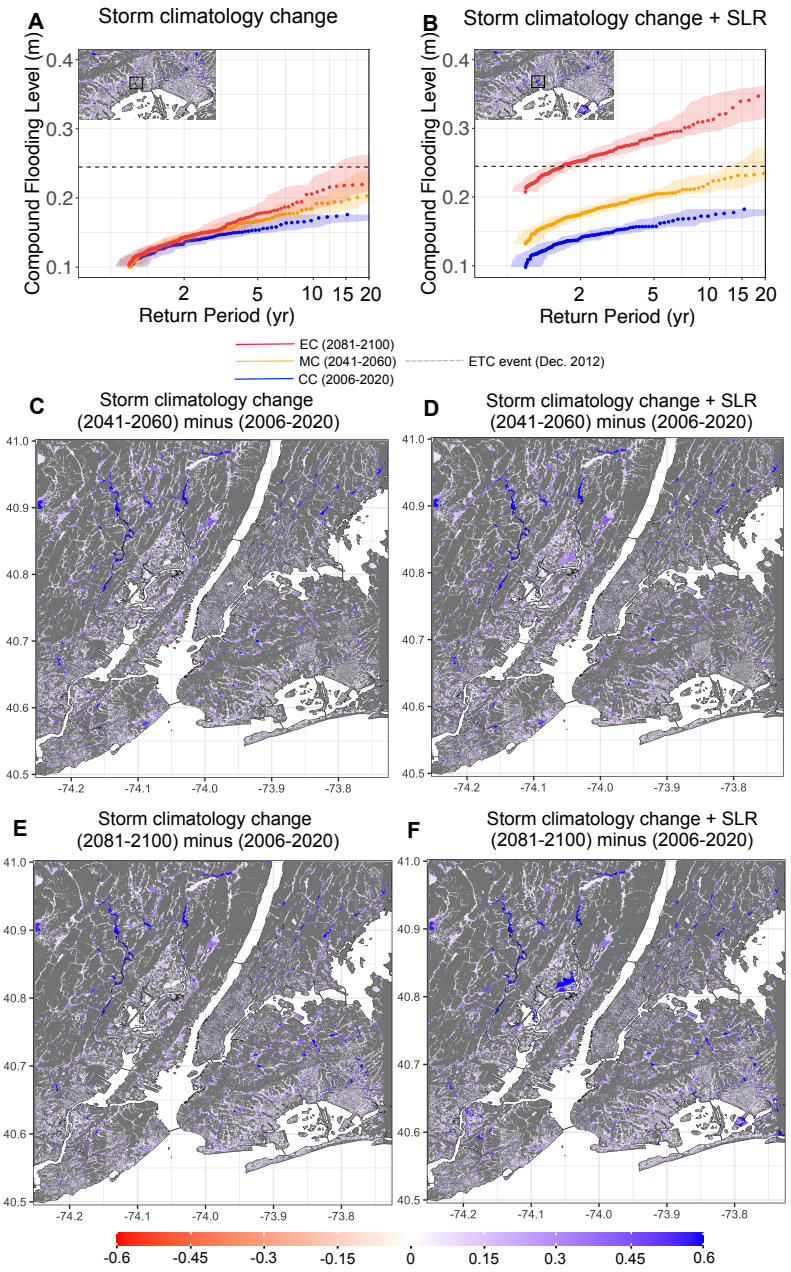

Figure 5: Impact of current and future changes in storm climatology and SLR on the risk of ETC compound flooding in NYC. (A and B) Individual and joint contribution of storm climatology changes and SLR on the risk of ETC compound flooding in the current and future climates. The results are based on the mean of compound flooding level calculated for the depicted area. Each line shows the results for ETC events dynamically downscaled by WRF in the current and future climates. The gray dashed line shows the magnitude of compound flooding from the ETC which occurred in December 2012 for the depicted area.(C and D) Impact of storm climatology changes and SLR on the spatial risk of 15 *yr* return period ETC compound flooding events by the middle of the century relative to the current climate, and (E and F) by the end of the century relative to the current climate.

2.6 Discussion

In this study we demonstrated the contribution of SLR and TC and ETC climatology changes to intensifying flooding hazard in NYC. We found that anthropogenically induced changes to TC activity have already increased flood risk in NYC. This risk increase translates to more damage from upper tail events, consistent with previous studies on the effect of anthropogenic warming on the risk and damages of extreme storms Strauss et al. [2021], Garner et al. [2017], Lin et al. [2016]. Our findings reveal that the effect of SLR on flooding from TCs and ETCs has been underestimated, relative to the impact of storm climatology changes in previous studies Lin et al. [2016, 2012]. Most previous studies did not employ spatially-detailed hydrodynamic simulations of compound surge and rainfall driven flooding. Simpler, often statistical methods used in previous studies are not well suited to quantifying spatially and temporally varying flood risk or the contributions of the individual drivers to the net flooding. This information is essential to designing robust adaptation and mitigation measures. By ignoring the mechanical and nonlinear hydrodynamics of compound flooding, they underestimate the risk of extreme storms such as Hurricane Sandy. According to our physics-based approach, Sandy-like compound flooding occurs around once every $\sim$150 yr compared to previous estimates of $\sim$400-500 yr Lin et al. [2016, 2012], Reed et al. [2015], and will occur once every $\sim$65 yr by the middle of the century, and once every $\sim$30 yr by the end of the century under the SSP3-7.0 scenario. We believe that the current risk of compound flooding from ETCs has also been underestimated in prior studies. We thus provide evidence that the frequency and intensity of compound flooding in NYC from both TCs and ETCs could increase, with rapidly growing risk to communities and infrastructure. Our results are also consistent with the work of Gori et al. [2022], showing that SLR is the most dominant driver of the joint rainfall-surge hazard in the future in NYC.

The approach we use to quantify TC risk is capable of assessing risks from very low frequency events, since we can generate an almost unlimited number of synthetic cyclones. By contrast, our assessment of ETC-associated risk is severely circumscribed by the low number of events one can afford to simulate with embedded, three-dimensional models like WRF. Future research should explore better and more efficient ways of downscaling extratropical cyclones. It may be that the only practical way forward is to run ensembles of high-resolution global models in present and future climates and infer ETC climatology directly from the output. This would require extraordinary resources to carry out the simulations and to analyze the resulting output. We did not include astronomical tides in our calculations; these should be included in future surge and compound flood risk assessments. Finally, our TC downscaling is not ideally suited to extratropical transitioning storms like Sandy. As such storms can be very destructive, more work needs to be done on assessing their risks and how they might evolve under climate change.

Overall, this study emphasizes how vulnerable coastal communities are and should serve as a guide to how they might assess and adapt to increasing flooding risk from tropical and extratropical cyclones. Our physics-based methodology can be easily transferred to other tropical and extratropical vulnerable coastal regions with no instrumental records to provide critical insight on the role of human-made global warming in changing the risk of TC and ETC induced compound flooding in the current and future decades. Our findings could help decision makers adapt coastal cities and infrastructure to mitigate

adverse consequences arising from intensifying compound flooding risk. Human-made climate change and SLR can be viewed as threat multipliers to the risk of compound flooding from TCs and ETCs. Along with the greenhouse gas emission reductions needed to mitigate climate change, further work that informs adaptation, such as the present study, is critical to limiting the risk and damage associated with a warming climate. It should be noted that data related to flooding damage may not always be readily available to the public, particularly with respect to quantifying the monetary losses to properties resulting from compound flooding and the anticipated damage from SLR in the current and future decades within a given study area. If a proprietary dataset containing this information were to become available, it could enable the generation of estimates for the monetary losses caused by both high and low frequency tropical and extratropical storms in both current and future climates.

3 Risk Assessment of Wind-Driven Damage from hurricanes

In this section, we present a model that accurately assesses the impact of climate change on wind-driven monetary losses caused by hurricanes in both present and future decades in NYC. Our approach involves several steps that we outline in the following sections:

3.1 Downscaling of hurricanes and their corresponding wind events

In this section, we used the high-resolution statistical-deterministic tropical cyclone model to generate a large set of synthetic hurricanes, consistent with the ERA-Interim reanalysis and GCM climates, similar to the previous section. This approach allowed us to estimate the climatology and evolution of hurricanes' high-speed winds in the current and future decades in NYC. To represent the evolution of hurricanes under the SSP3 7.0 scenario, we used the large set of storms using three bias-corrected CMIP6 GCMs and the ERA-Interim reanalysis explained in the previous section. The downscaled surface maximum wind speed (with ∼20 m spatial resolution) during landfall of these synthetic hurricanes was used to quantify the associated monetary losses from wind hazard of hurricanes under the current and future warming climate.

3.2 Optimizing damage function using conditional random field theory

The damage to properties caused by windstorms, such as hurricanes, increases rapidly with the wind speed. To model this relationship, we developed a damage function that expresses the fractional property losses as a function of the cube of the wind speed over a threshold value. The function also saturates at high wind speeds. We can represent this damage function mathematically as follows Emanuel [2011]:

$$f = \frac{\upsilon_n^3}{1 + \upsilon_n^3} \tag{1}$$

$$\upsilon_n = \frac{\max[(V - V_{\text{thresh}}), 0]}{V_{\text{half}} - V_{\text{thresh}}} \tag{2}$$

Here, f represents the fractional property value lost, and V is the surface maximum wind speed. V_{thresh} is the wind speed at or below which no damage occurs, and V_{half} is the wind speed at which half of the property value is lost. The damage function presented here is in line with previous studies that have used both theoretical and insurance claim data for damage calculations Watson Jr and Johnson [2004]. However, accurate quantification of damages and reduction of uncertainties in monetary losses for different building types and specific locations requires optimization of the damage function. This optimization can be achieved by tuning the parameters V_{thresh} and V_{half} using the Homesite wind damage claims and exposure database, which account for building codes and property strength in various coastal and inland regions.

To optimize the damage function, a grid-based approach with a spatial resolution of 5 km $\times$ 5 km is employed (Figure 6-A). Within each grid cell, historical hurricane maximum wind speeds are simulated using the physics-based model forced by re-analysis ERA5 data for Hurricanes Fay (2020), Henri (2021), Ida (2021), Isaias (2020), and Elsa (2021). The total fractional property losses to insured properties during the landfall of these hurricanes are calculated from the Homesite claim dataset. However, due to the limited number of available hurricane losses, it is not possible to extend the method to other historical hurricanes that occurred in the past. Therefore, to increase the number of samples and improve the optimization of the damage function in each grid cell, a physics-based augmentation technique is utilized . This technique generates multiple synthetic hurricanes for each historical hurricane, thereby increasing the number of wind samples per grid cell (Figure 6-A). In addition to generating multiple synthetic hurricanes, a small amount of noise is added to the damage part of each augmented historical hurricane to make the damages unique for each synthetic hurricane. By utilizing these augmented wind speed simulations and loss claims, the damage function is empirically derived for each grid cell. This empirically derived damage function includes a lower onset threshold and an upper damage threshold (Figure 6-B).

To improve the prediction of wind losses in each grid cell using equation 1, we developed an empirical function that incorporates information about wind speed and losses in each cell, as well as spatial information from surrounding grid cells, using the theory of conditional random fields (CRFs) Sutton et al. [2012]. The CRFs utilize unary and pairwise functions to model the relationship between wind speed and losses in each grid cell. The unary function captures the relationship between wind speed and losses in a given grid cell, while the pairwise function incorporates prior information from eight adjacent grid cells to account for the spatial correlation between wind speeds and losses (Figure 6-C). We describe the probability of a loss sequence in each grid cell given a maximum wind speed sequence using the following equation:

$$P(Y|X) = \frac{1}{Z} \exp\left(- \sum_{i=1}^{m} \lambda_i f_i(X, Y_c) \right) \tag{3}$$

$$Y_c = y_i x_i \quad \text{or} \quad Y_c = y_i y_j \tag{4}$$

The equation represents a conditional probability distribution, where Y represents the output variable (wind driven losses) and X represents the input variable (maximum wind speed). The model is based on the conditional random field (CRF) framework, which provides a way to model complex dependencies between these two variables. In this equation, Z is the normalization constant that ensures that the probabilities sum up to 1 over all possible values of Y. The λ_i are weights associated with each feature function f_i, which are defined over pairs of maximum wind speed and damage variables.

The feature functions capture the effect of wind speed (x_i) on damage (y_i), as well as the interaction between neighboring outputs (y_i and y_j) on the probability of the current output (Figure 6-C). The term $-\sum_{i=1}^{m} \lambda_i f_i(X, Y_c)$ represents the weighted sum of the feature functions over all pairs of maximum wind speed and damages in grid cells. The model assigns higher probabilities to damage sequences with lower energy, meaning sequences

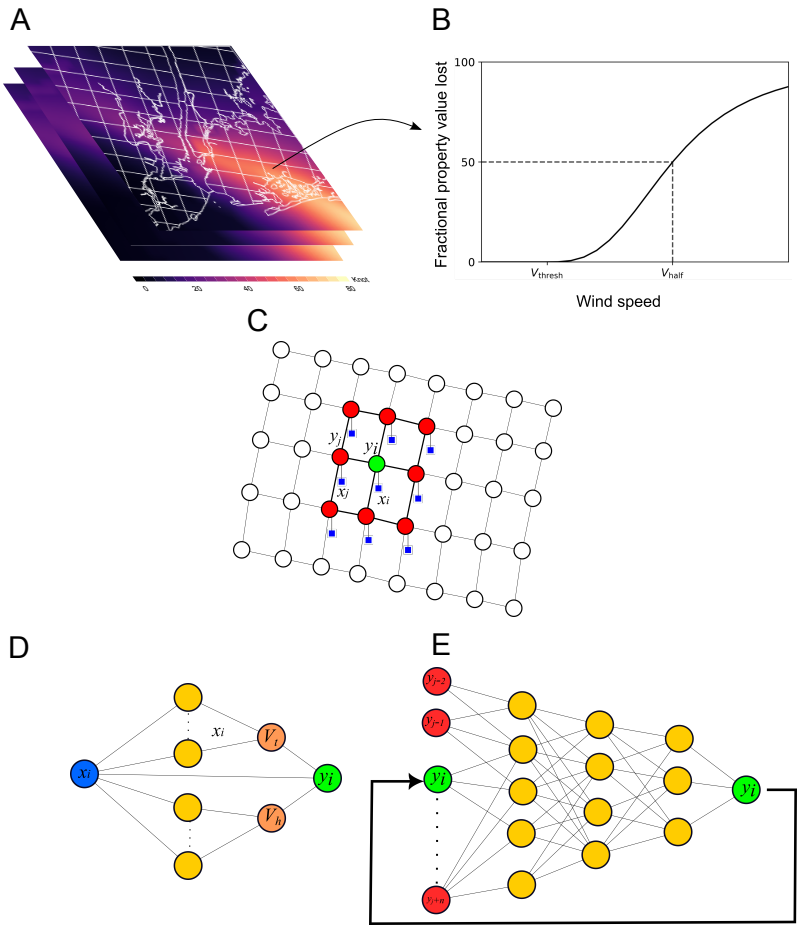

Figure 6: The process involves optimizing the damage function for each grid cell of size 5 km × 5 km. (A) augmenting the maximum surface wind speed from historical hurricanes, (B) creating an empirical model of the damage function that represents the relationship between maximum wind speed and fractional property value lost, (C) developing a Conditional Random Fields (CRFs) model to capture the relationship between wind speed and losses in each grid cell (unary function) and eight surrounding grid cell (pairwise function), (D) employing a simple neural network for the unary function to model the relationship between maximum wind speed and losses, to optimize the two wind thresholds (V_{thresh} and V_{half}) in each target grid cell, and (E) using a Deep Learning model to learn the weights associated with each unary and pairwise feature function f_i in the CRF model.

that are more consistent with the maximum wind speed data. In other words, the model predicts the likelihood of different damages given a set of maximum wind speeds. Overall, this CRF model provides a powerful framework for modeling the complex relationships between wind speed and damages, which can have important applications in predicting monetary losses caused by severe weather events.

To accurately optimize the damage outputs in each grid cell, it is important to account for the complex relationship between wind speed and damages between different grid cells. To achieve this, we developed a deep learning model that learns the weights associated with each unary and pairwise feature function f_i in the CRF model. The deep learning model consists of input layers that represent the damage in the target grid cell and the eight surrounding cells, and an output layer that represents the predicted damage in the target cell (Figure 6, D and E). This structure is applied to all the grid cells

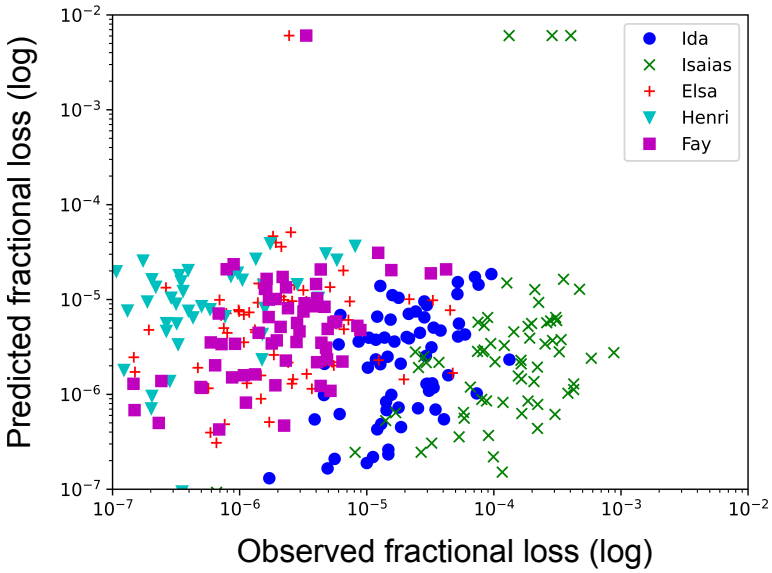

Figure 7: Evaluation of fractional property damage using Leave-One-Out process for the five observed hurricanes. (Results for each grid cell represented by dots).

in the study area simultaneously to train the λ_i weights associated with each feature function f_i. The number of hidden layers, neurons, and activation functions for each layer are specified. To train the model, we used a stochastic gradient descent optimization algorithm that minimizes the loss function between predicted and actual damage in each grid cell simultaneously. The weights of the model are updated iteratively to improve prediction accuracy.

This deep learning model provides an effective approach to capture the intricate relationship between wind speed and damages among neighboring grid cells within the study area. By adjusting the weights assigned to each feature function f_i, we can precisely optimize the two thresholds outlined in equation 2 and subsequently the damage function for each grid cell. The optimized damage function has the potential to predict monetary losses resulting from future hurricanes.

The performance of our model was assessed using leave-one-out cross-validation to evaluate its performance on five historical hurricanes. The results of this evaluation are presented in Figure 7, which shows the model's performance on each of the five historical hurricanes. We found that the model was effective in capturing the complex relationships between wind speed and damages, and its predicted fractional damages were aligned with the observed damages from each hurricane. Figure 7 illustrates these findings by demonstrating that the model effectively modeled the complex relationships between wind speed and damages. These results provide evidence that our model can accurately predict wind-driven financial losses caused by hurricanes.

Figure 8 shows the optimized damage function for each grid cell in our study area. We found that integrating spatial information through Conditional Random Fields (CRFs) improves the accuracy of predicting wind-driven financial losses when compared to conventional techniques. These optimized damage functions were specifically tailored to the insured portfolio of Homesite in this study area. We then utilized these optimized

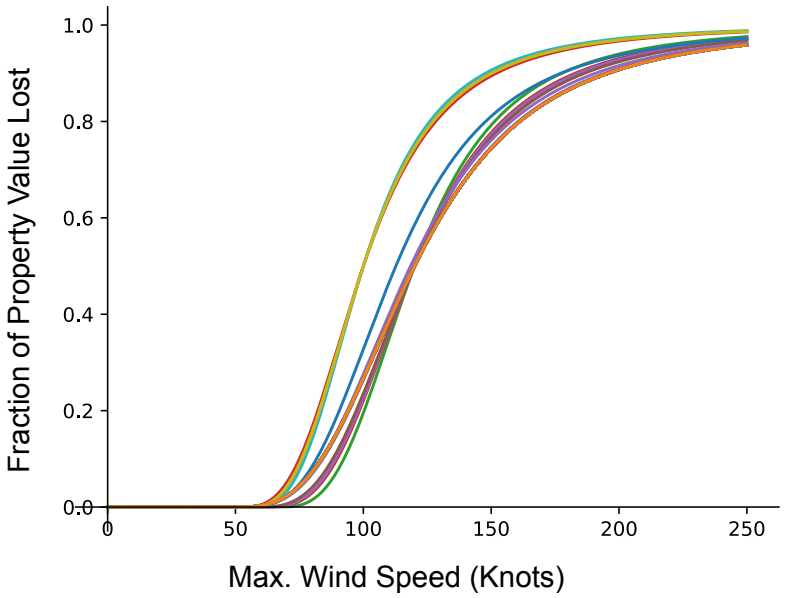

Figure 8: Optimized damage functions for each grid cell in the study area

functions and pair-wise CRF functions to quantify the monetary losses from wind-driven damages that may arise from future intensifying hurricanes in the coming decades. To achieve this, we employed the physics-based model to simulate a large set of synthetic hurricanes that are projected to pass through NYC by the middle and end of the century. These simulations were obtained from the three CMIP6 climate models under the SSP3-7.0 scenario.

By replacing the maximum wind speed of these synthetic hurricanes in the optimized damage functions, we can calculate the monetary losses that may arise from each hurricane in each specific grid cell. Summing up the total monetary losses for the entire area enables us to generate a large set of monetary losses from different weak and strong hurricanes in the past, current, and future decades. These total monetary losses are then used to assess the risk of monetary losses caused by hurricanes' strong winds under a warming climate in the future decades.

3.3 Quantifying the risk of monetary losses from intensifying storms in current and future climates

To assess the potential impact of future intensifying storms on monetary losses, we utilized optimized damage functions that were tailored to each grid cell. By incorporating the maximum wind speed projections from downscaled future storms into these damage functions, we calculated the fractional damages to insured properties. This approach enables us to generate a large dataset of fractional property value losses that can be multiplied by the total property values to estimate the property monetary losses resulting from the past, current, and future storms. This methodology allows for a more comprehensive and accurate assessment of the potential economic impacts of intensified storms in the future.

To assess the potential increase in the risk of monetary losses resulting from intensifying

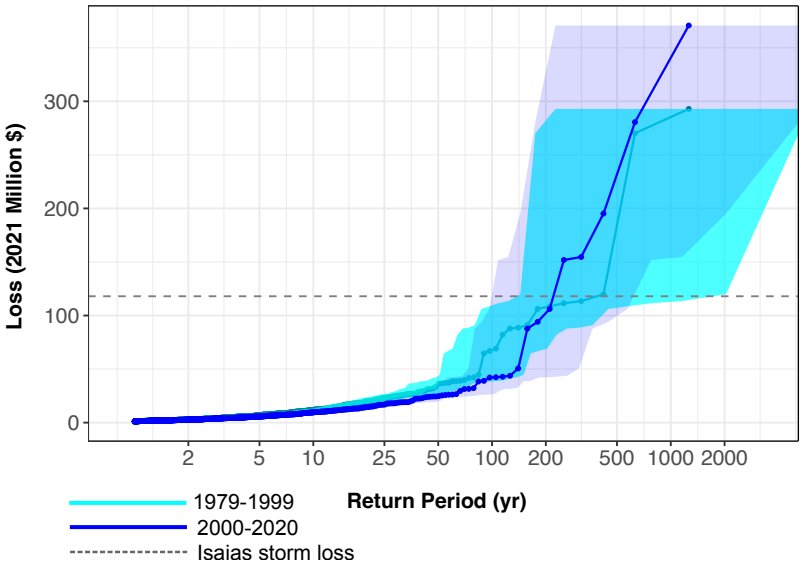

Figure 9: Monetary Loss Risk from Wind Damage of Hurricanes to Homesite Insured Properties in the Late 20th Century and Current Climate based on ERA5 Reanalysis Data: Uncertainty Bounds Calculated using 5th and 95th Percentiles of a Poisson Distribution

storms due to climate change, we employed a probabilistic analysis across different return periods in past, current and future decades. The return periods are calculated based on annual exceedance probability. We account for the inherent uncertainty in the monetary losses by utilizing multiple climate model simulations and sampling uncertainty for low and high frequency storms.

Figure 9 displays the monetary losses associated with hurricanes in the late 20th century and the current climate, as a function of different return periods. Each dot on the plot represents the monetary losses for Homesite insured properties from each hurricane in the two time periods in the study area. The loss results are probabilistic and indicate the likelihood of such losses occurring. For instance, storms similar to Hurricane Isaias (which caused a monetary loss of $117 million) would be expected to occur once every $\sim$400 yr years in the late 20th century and every $\sim$200 yr years in the current climate, indicating a doubling of the risk of monetary losses for such a hurricane in the current climate. This translates to a probability of such a monetary loss occurring from such a hurricane every year of 0.25 percent in the late 20th century and 0.5 percent every year in the current climate. The same presented values of monetary losses correspond to different likelihoods of occurrence in the late 20th century and current climates. For instance, the monetary losses with a likelihood of 2% in each given year amount to $24 million, while the losses with a likelihood of 1% are valued at $42 million in the current climate. Similarly, the losses with a likelihood of 0.5% amount to $106 million, and those with a likelihood of 0.1% are valued at $340 million. These values indicate the increasing probability of higher monetary losses associated with lower likelihoods of occurrence.

Figure 10 presented here shows the monetary losses caused by wind damage from hurricanes in the study area for three different time periods - current, mid-century and end of century. The risk of monetary losses is also quantified in a probabilistic manner and is presented as a function of return periods.

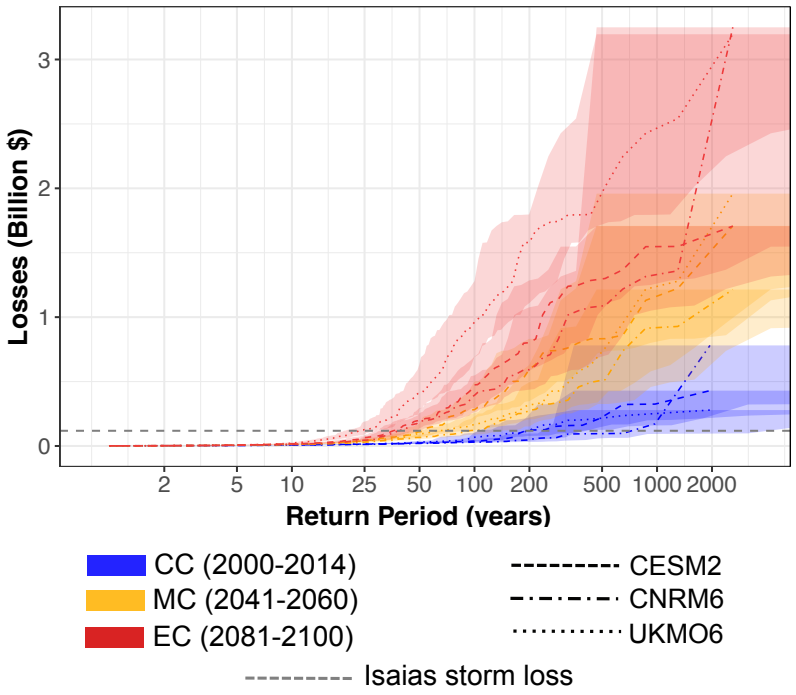

Figure 10: Monetary Loss Risk from Wind Damage of Hurricanes to Homesite Insured Properties in current and future decades from three climate model simulations. Uncertainty Bounds Calculated using 5th and 95th Percentiles of a Poisson Distribution

For example, the ensemble mean of monetary losses that occur once every 100 years or with a probability of 1% in each given year in the current climate is approximately $45 million. This value increases to $190 million by the mid-century and $610 million by the end of century. This implies that the risk of monetary losses for such storms will increase up to 4 times by the mid-century and 13.5 times by the end of century. Another way to interpret the monetary risk results is by quantifying the return period or likelihood of occurrence for a specific monetary loss. For instance, the frequency of monetary losses similar to those caused by extreme storms like Isaias (valued at $117 million) in the study area based on ensemble mean of the three climate models is once every $\sim$350 yr in the current climate, once every $\sim$70 yr years by the mid-century, and once every $\sim$30 yr years by the end of century. This means that the likelihood of occurrence for such a monetary loss from an Isaias-like storm for each given year in the current climate is 0.29%, and it increases to 1.4% by the mid-century and 3.3% by the end of century. Similarly, the likelihood of occurrence for other high frequency and low frequency wind-driven monetary losses from hurricanes can also be estimated for the study area. The results demonstrate that climate change increases the monetary losses from wind-driven damage resulting from hurricanes in the study area.

3.4 Discussion

Our study showed that incorporating physics-based methodology can significantly improve the accuracy of predictions of wind-driven monetary losses caused by hurricanes. By integrating a range of factors, including wind speed, losses during landfalling of historical hurricanes, and spatial information from surrounding cells, our empirical damage functions have provided a robust foundation for accurate predictions. Furthermore, the

use of conditional random field and deep learning models enabled us to capture the complex relationship between wind speed and damages, making our model highly effective in predicting monetary losses to Homesite insured properties given a set of maximum wind speeds from future intensifying storms under the impact of climate change.

Our findings have significant implications for the insurance industry and emergency management agencies. Accurate predictions of monetary losses resulting from hurricanes can inform pricing strategies, enabling insurers to prepare for future intensifying losses from these storms. Additionally, the methodology we have developed can be extended to vulnerable areas in the U.S., providing valuable insights into the locations that are most vulnerable to monetary losses from intensifying storms and their potential increase in vulnerability in the future under the effect of climate change.

As an insurance company, Homesite can leverage these results to develop new policies, set premiums, and respond to claims related to the hazards from these intensifying storms in a future warming climate. Overall, our study provides a powerful tool for predicting wind-driven financial losses caused by hurricanes, and we believe that it has the potential to make a significant impact in the field of risk management, as well as contribute to our understanding of the effects of climate change on extreme weather events.

4 Appendix

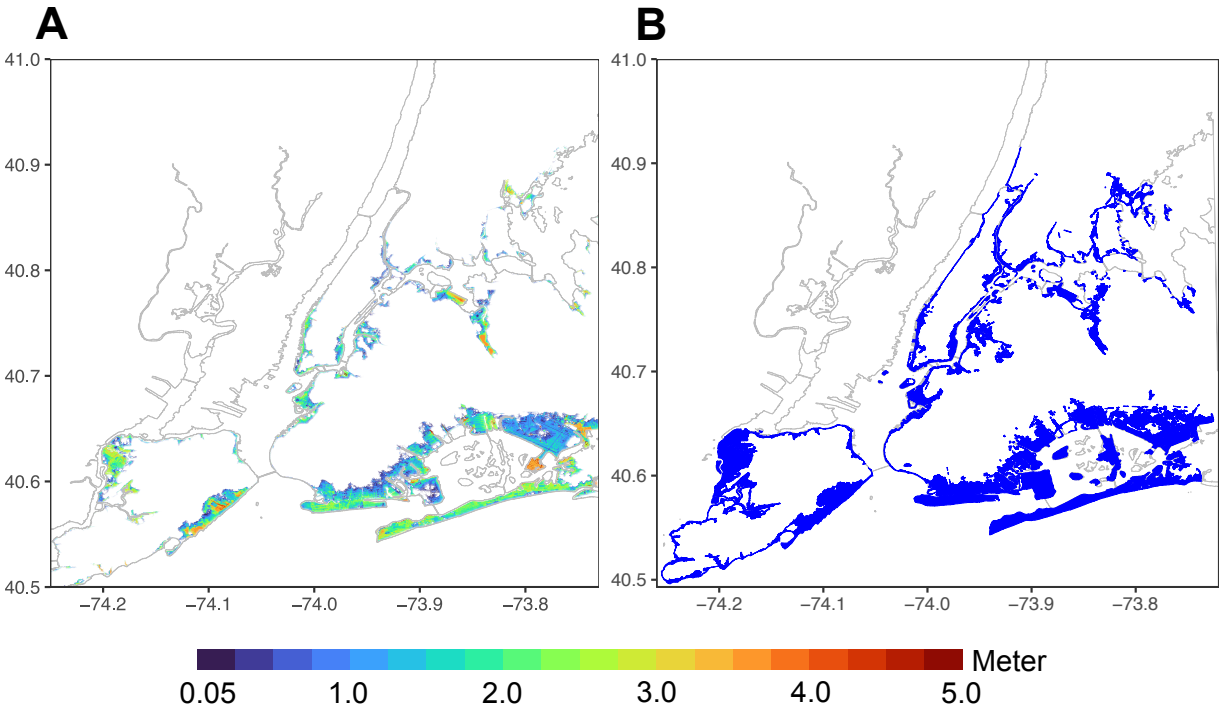

Figure 1: Performance evaluation of the LISFLOOD hydraulic model in simulating Sandy's surge driven flooding occurred in October 2012 in NYC. (A) Simulated surge driven flooding map from the Sandy-like event (synthetic track 1299 downscaled from ERA-Interim reanalysis) restricted to NYC. (B) Sandy's surge driven flooding extent map recorded from FEMA in NYC. Note that the FEMA map does not show flood levels but only areas inundated. The FEMA flood inundation map is downloadable from: https://data.cityofnewyork.us/Environment/Sandy-Inundation-Zone/uyj8-7rv5

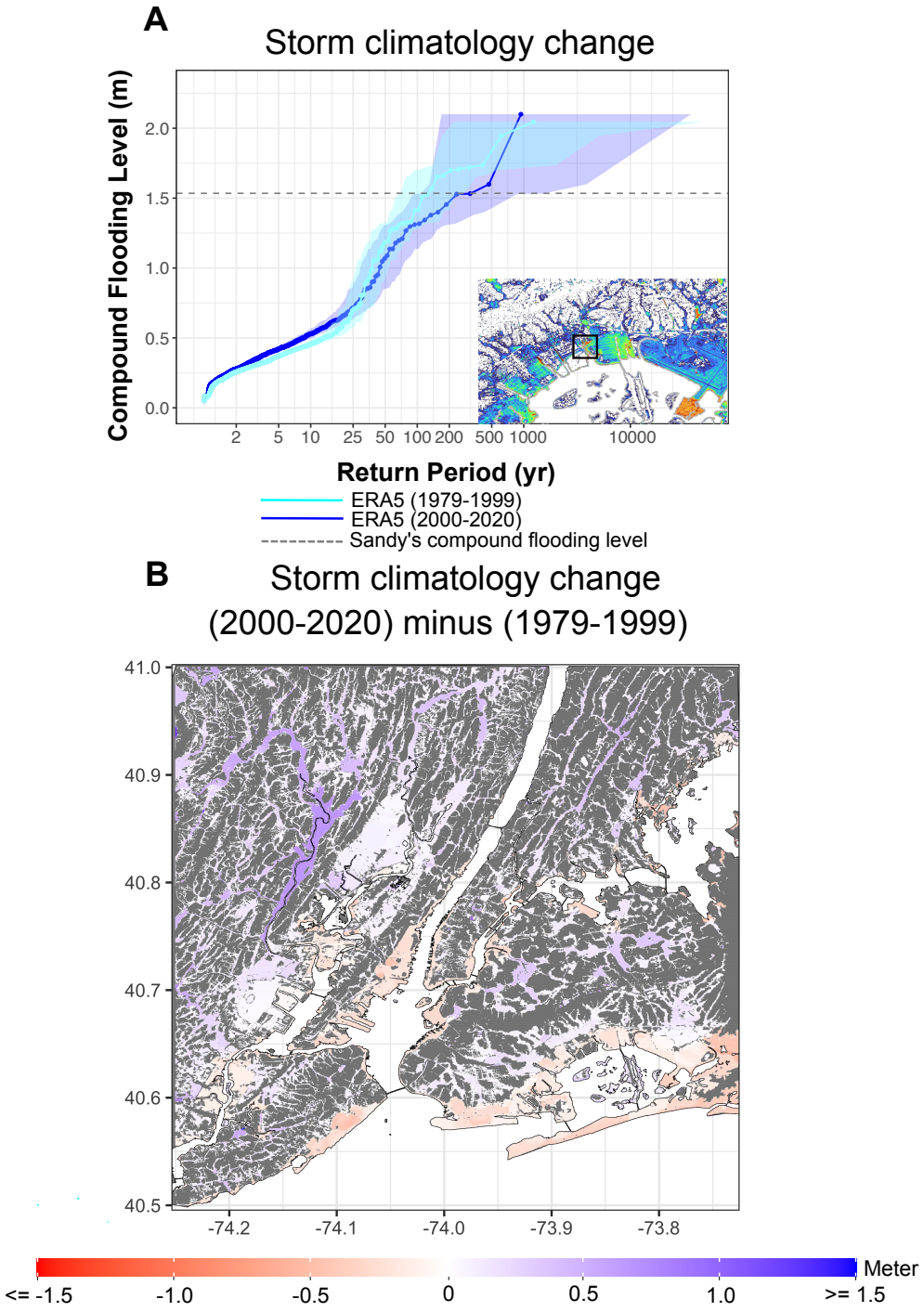

Figure 2: Impact of only TC climatology changes on the risk of compound flooding in today's climate (2000-2020) relative to the end of the 20$^{\text{th}}$ century (1979-1999) in NYC. (A) TC compound flooding level as a function of return period for today's climate and the end of the 20$^{\text{th}}$ century (the results are calculated based on the mean of compound flooding for the depicted area). Each line shows compound flooding results from synthetic TCs generated from ERA-Interim reanalyses over each time period. The gray dashed line shows the mean of Sandy compound flooding level calculated from the Sandy-like event (#1299) for the depicted area (shown in a black rectangle). (B) Impact of only TC climatology changes on the spatial risk of 100 y return period compound flooding events in today's climate relative to the 20$^{\text{th}}$ century (blue color shows increasing trend, and red color shows decreasing trend).

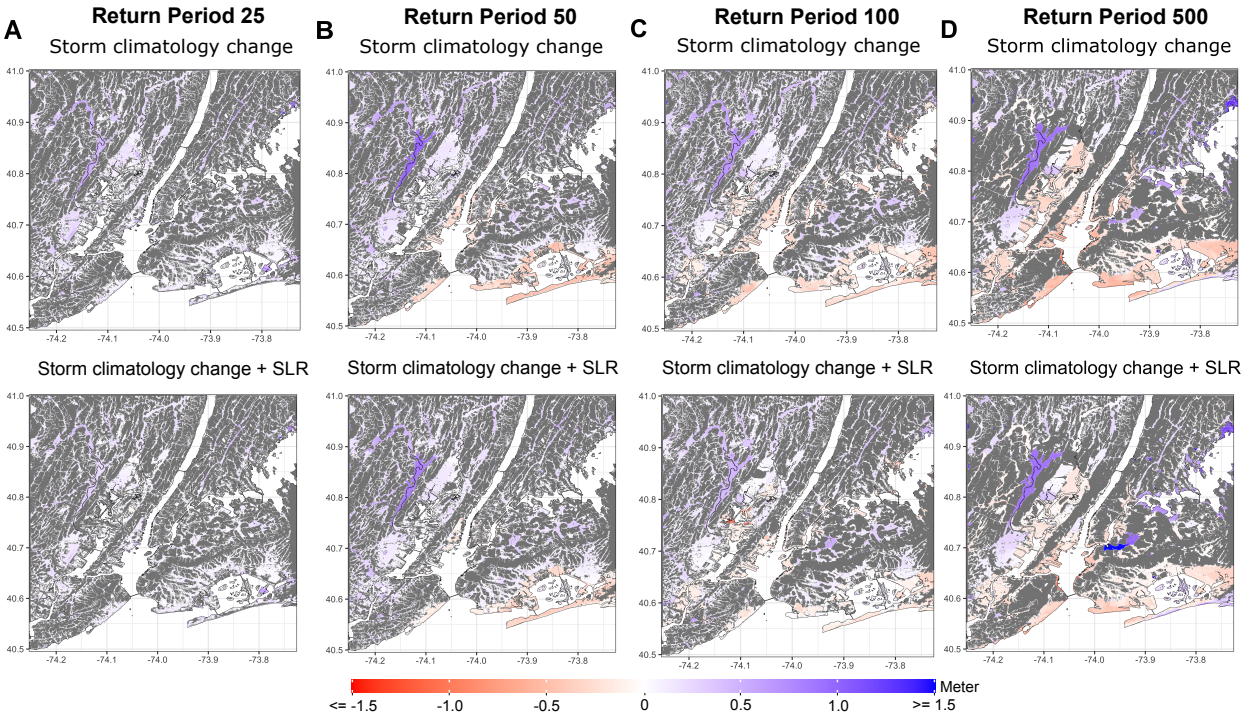

Figure 3: (A-D) Individual and joint contribution of storm climatology changes and SLR on the spatial risk of TC compound flooding events in today's climate (2000-2020) relative to the late 20$^{\text{th}}$ century (1979-1999) at different return periods. Blue color represents increasing trend, and red color represents decreasing trend.

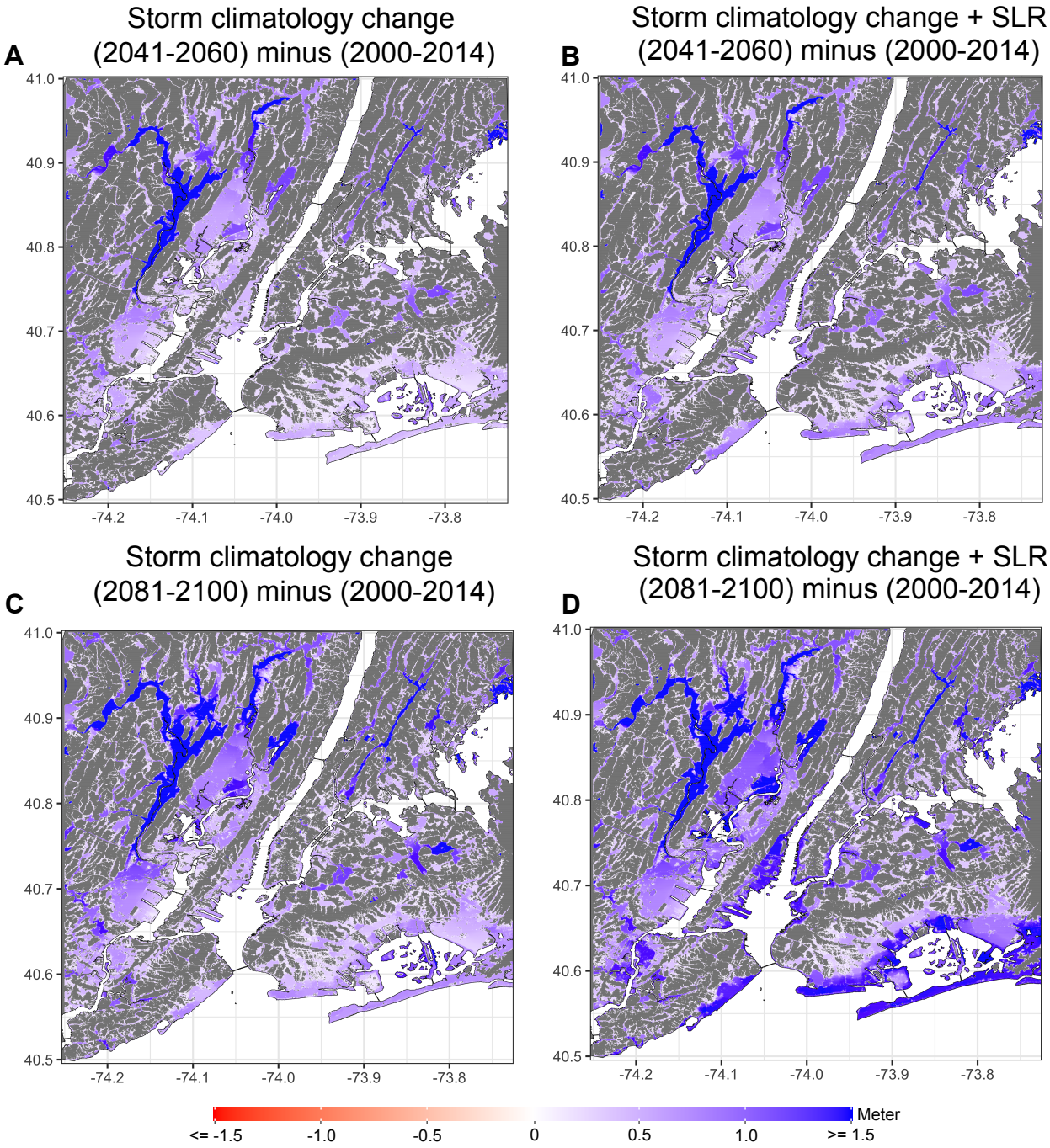

Figure 4: (A and B) Impact of storm climatology changes on the spatial risk of 50 y return period TC compound flooding events by the middle of the century relative to the current climate (upper left) and by the end of the century relative to the current climate (upper right). (C and D) Impact of storm climatology changes and SLR on the spatial risk of 50 y return period TC compound flooding events by the middle of the century relative to the current climate (lower left) and by the end of the century relative to the current climate (lower right).

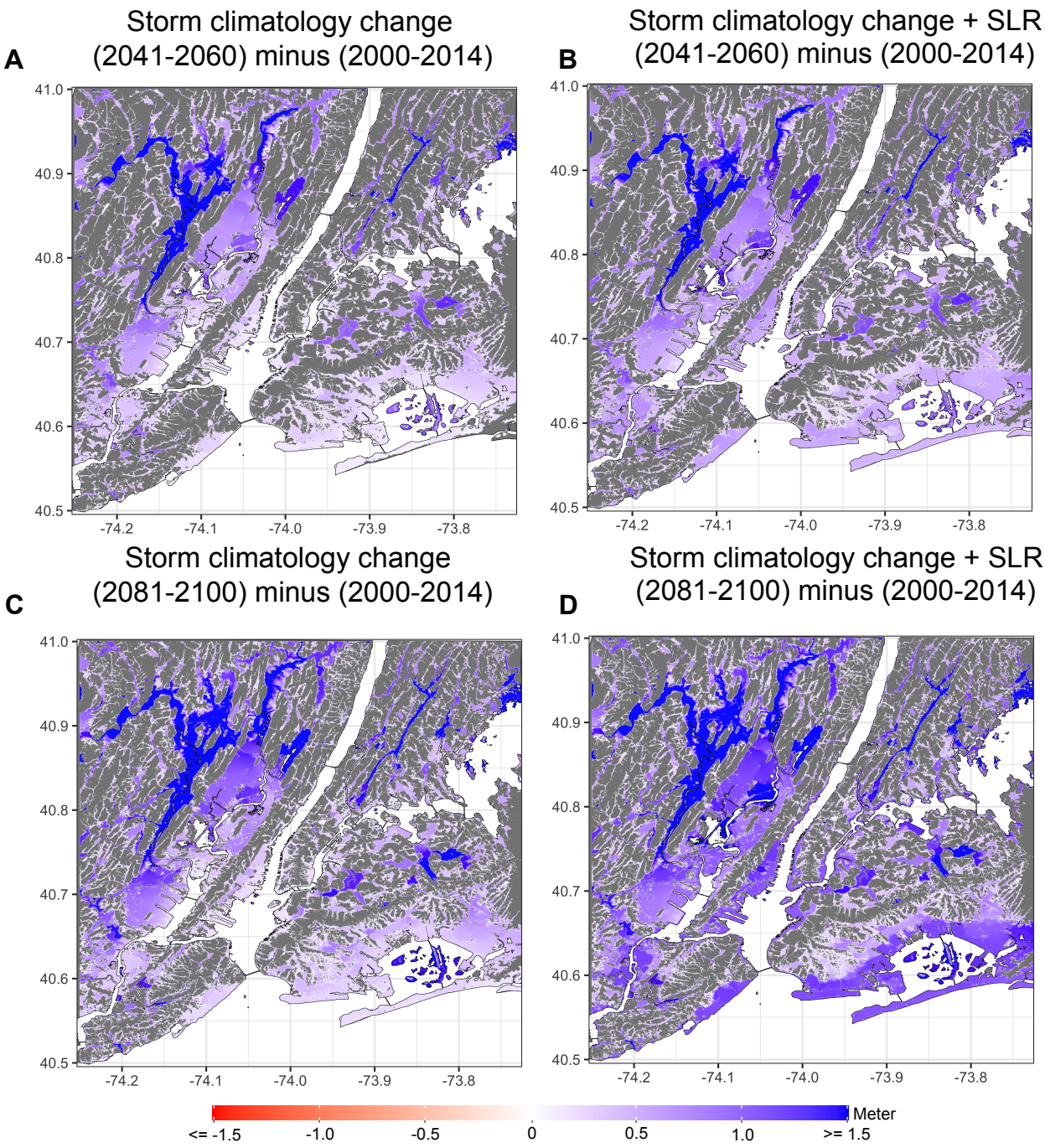

Figure 5: Similar to Fig. S4, but for 100 y return period.

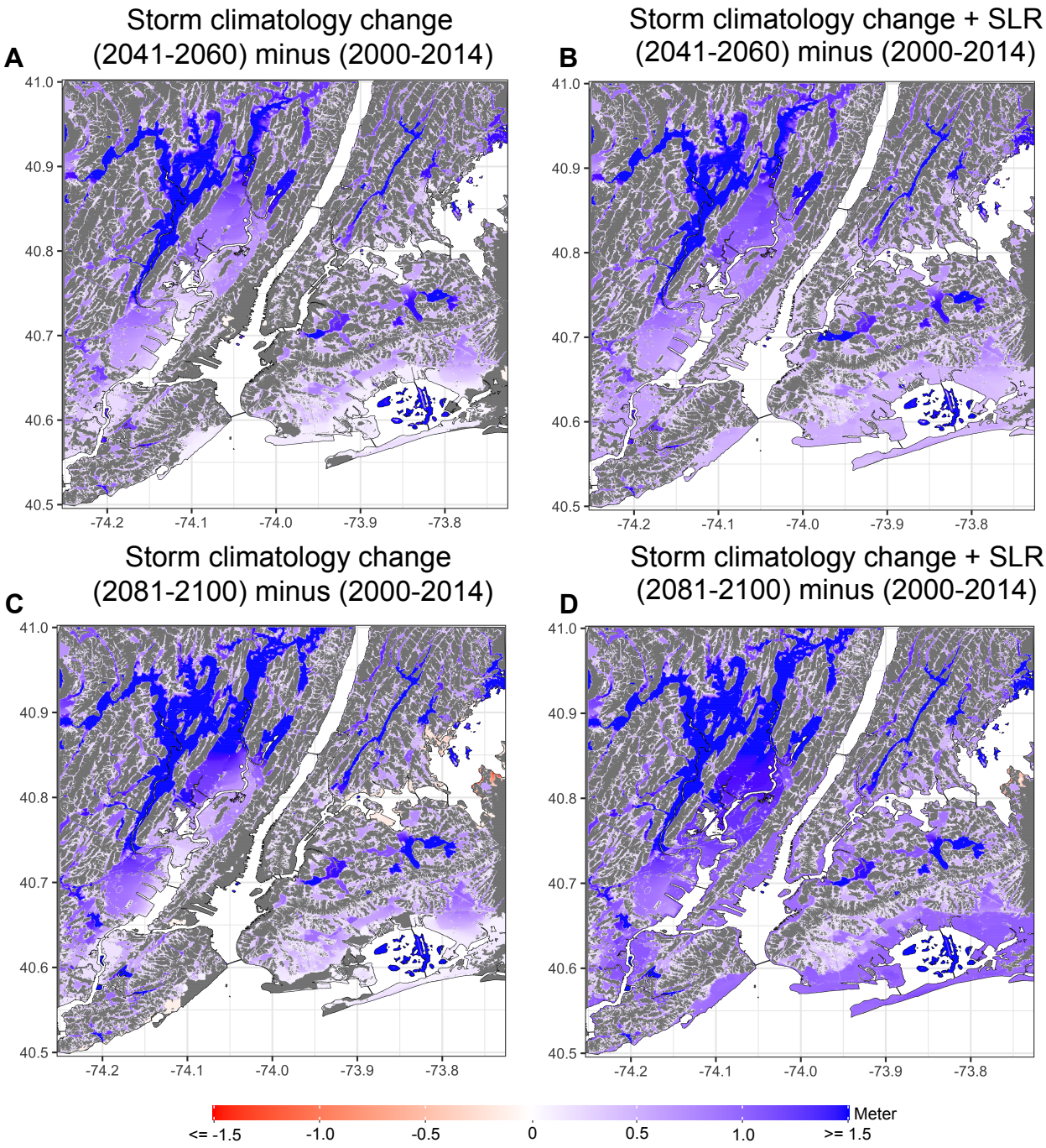

Figure 6: Similar to Fig. S4, but for 500 y return period.

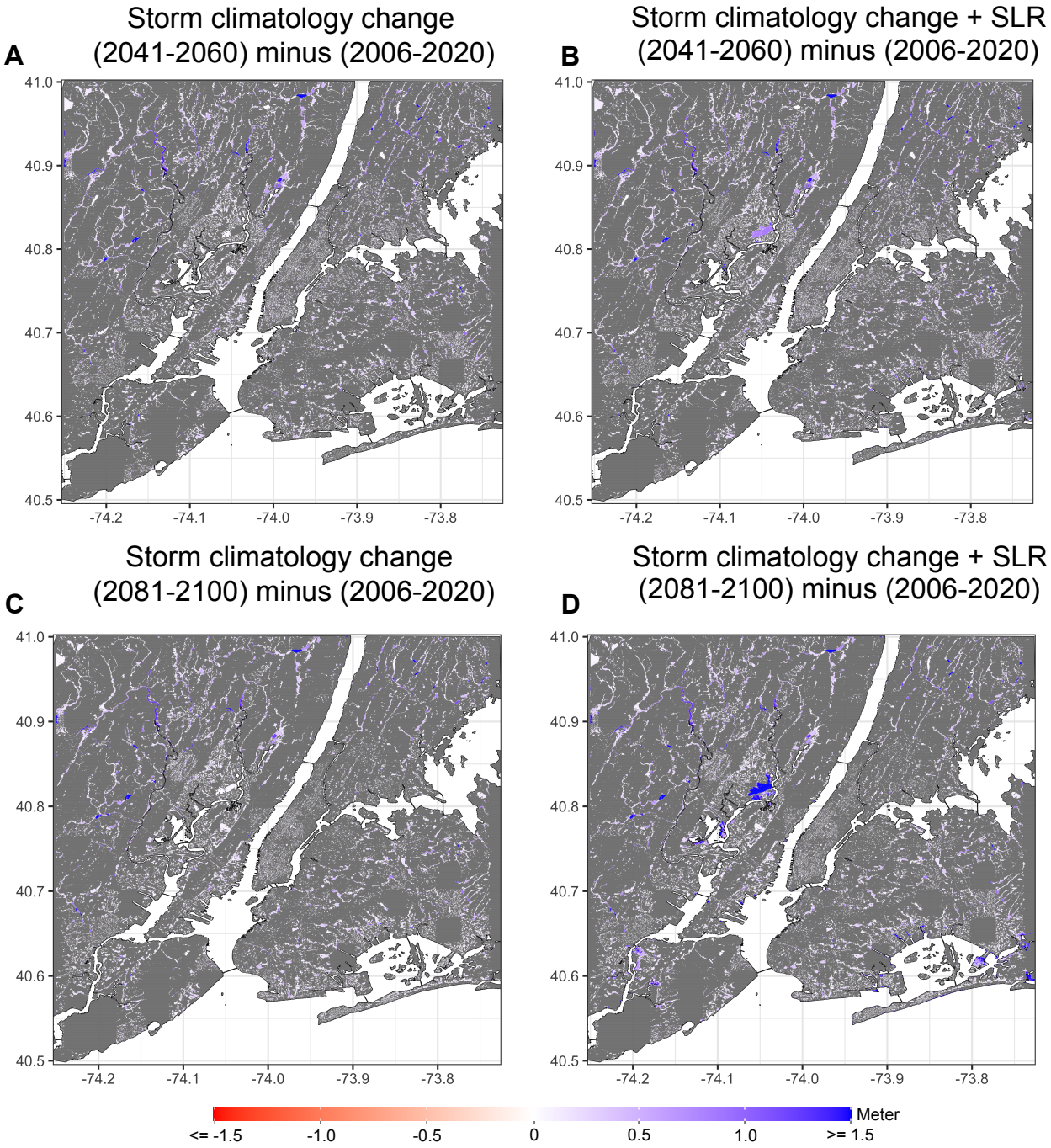

Figure 7: (A and B) Impact of storm climatology changes on the spatial risk of 5 y return period ETC compound flooding events by the middle of the century relative to the current climate (upper left) and by the end of the century relative to the current climate (upper right). (C and D) Impact of storm climatology changes and SLR on the spatial risk of 5 y return period ETC compound flooding events by the middle of the century relative to the current climate (lower left) and by the end of the century relative to the current climate (lower right).

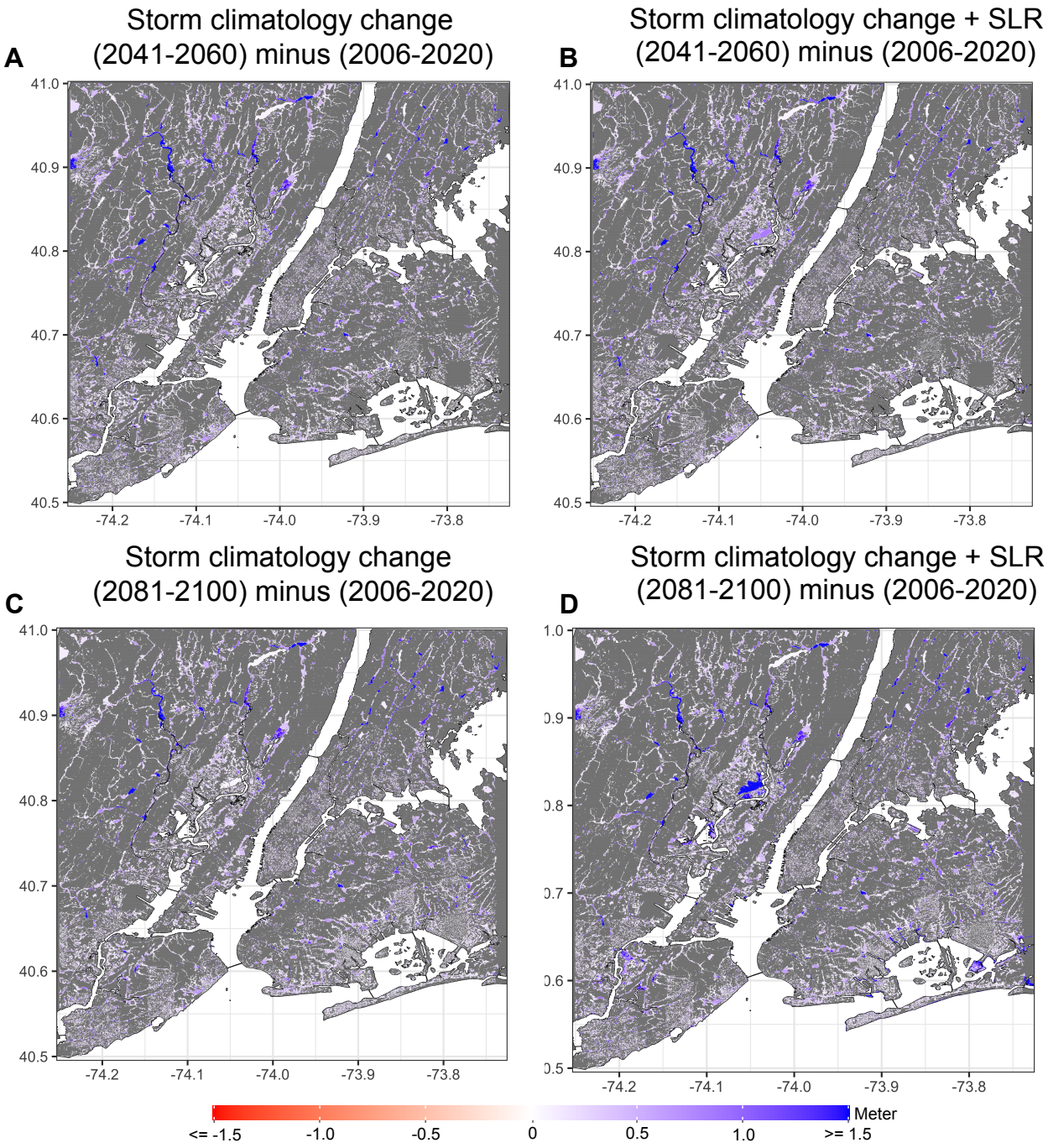

Figure 8: Similar to Fig. S8, but for 10 y return period.

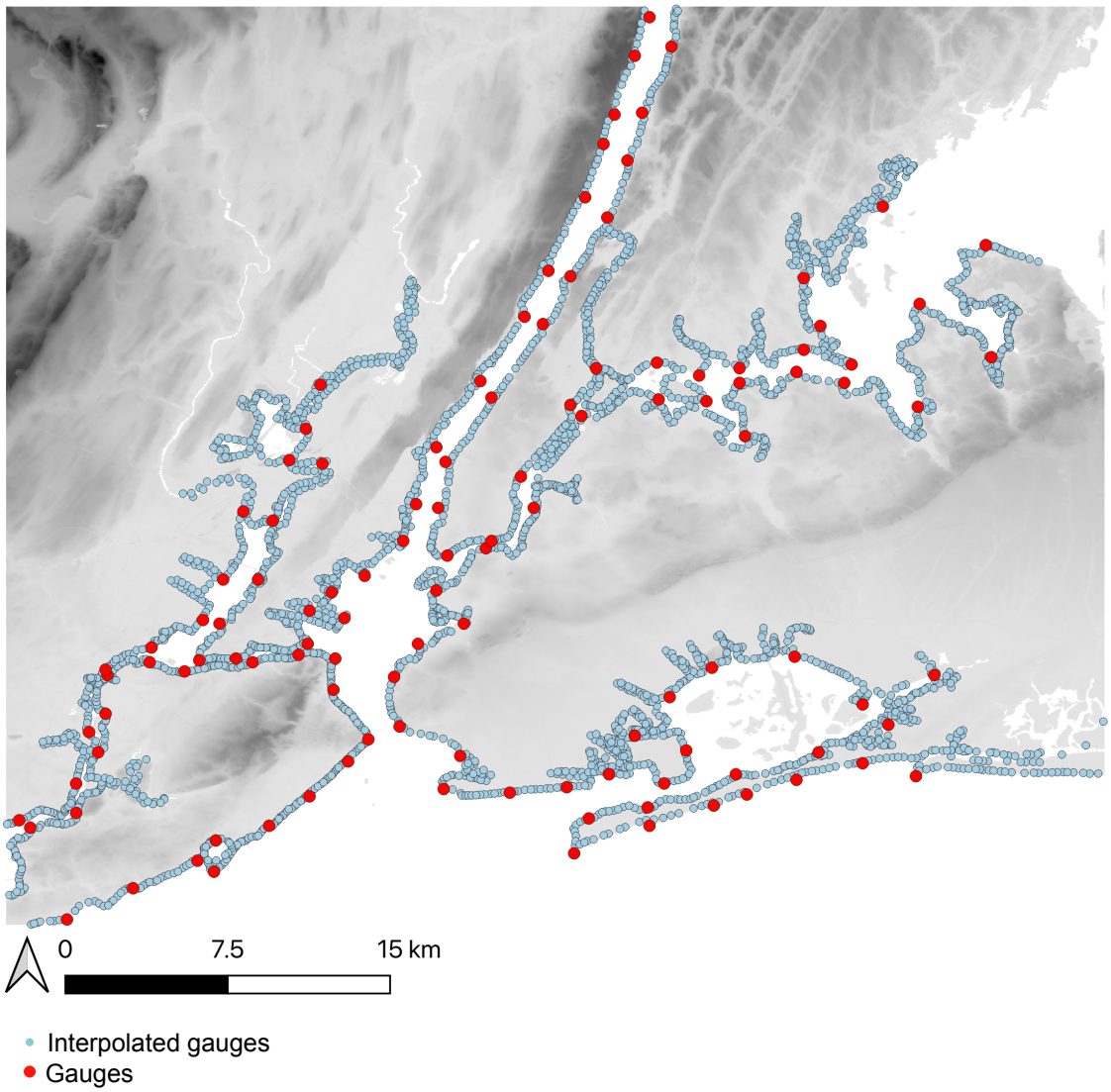

Figure 9: Location of synthetic gauges used for surge modeling of TC and ETC storms in NYC. Red points show the location of the main synthetic gauges (118 gauges) assigned across the coastline to record simulated surge heights by GeoCLAW. Blue points show the location of interpolated synthetic gauges (3113 gauges) assigned between the main synthetic gauges to cover the entire coastline.

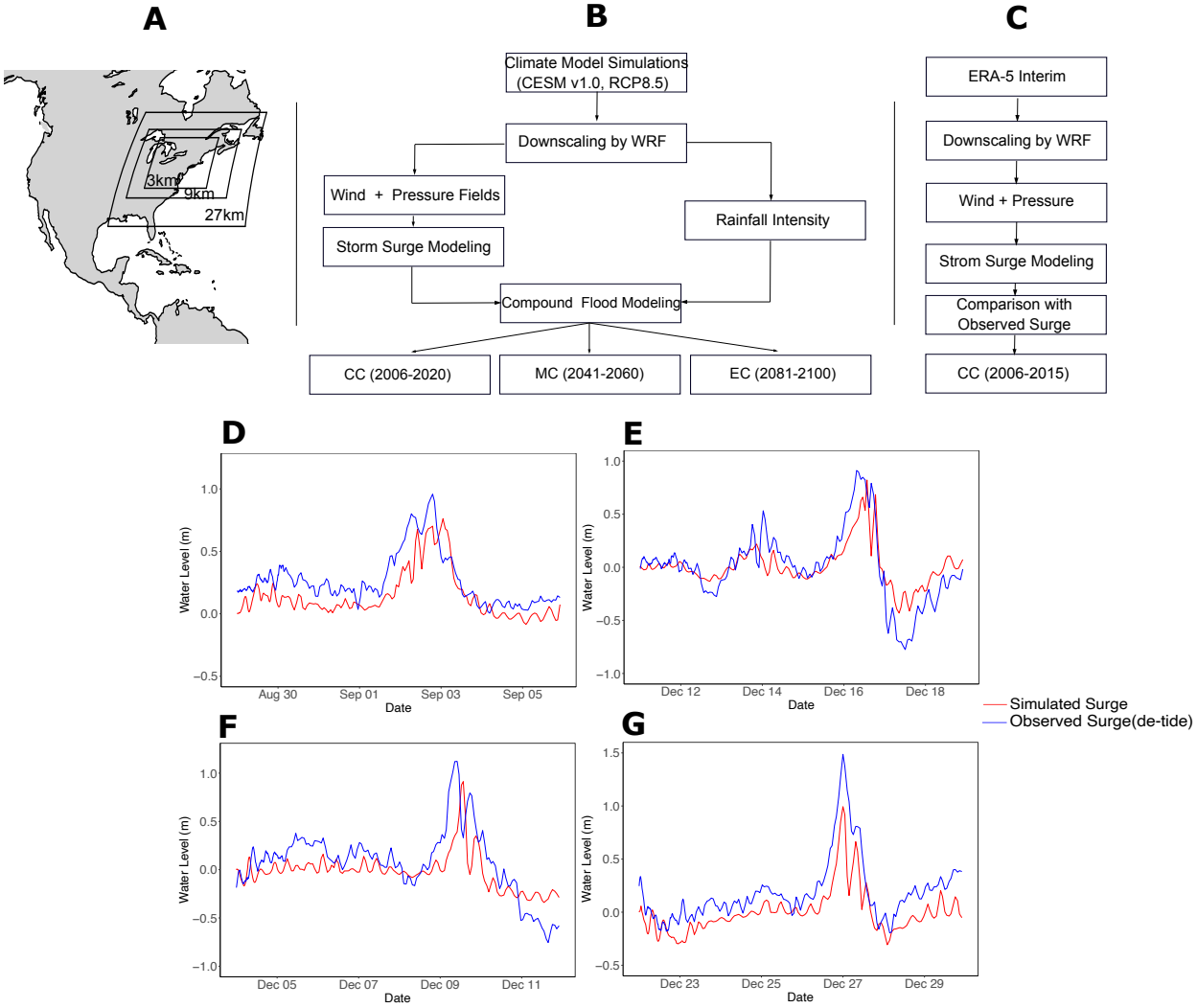

Figure 10: Process of downscaling and compound flood modeling from ETCs in historical and future climates. (A) Three nested grids of 27, 9, and 3-km spatial resolution used for dynamically downscaling WRF simulations (in this study we use downscaled WRF simulations of wind and rainfall within the 3-km spatial resolution domain). (B) Process of ETCs compound flood modeling in the current and future climates. (C) Evaluation process of surge modeling based on historical ETCs downscaled by WRF simulations driven by ERA-Interim reanalyses in the current climate. (D-G) Performance evaluation of GeoCLAW for historical ETC storms, which occurred in August 2006 (upper left), December 2007 (upper right), December 2009 (lower left), and December 2012 (lower right). Blue line represents observed surge heights during landfalling of the ETCs, calculated by de-tiding water levels (water elevation is subtracted from NOAA tide prediction at the Battery gauge). Red line represents surge heights simulated by GeoCLAW from WRF downscaled hourly wind and pressure fields driven by ERA-Interim reanalysis for the same historical events. Note that the temporal resolution in the x-axis is six minutes.

Report 2

Physics-based Risk Assessment of Compound Flooding from Tropical and Extratropical Cyclones in a Warming Climate in New Bedford, Massachusetts

1 Introduction

Tropical cyclones (TCs) are powerful storms characterized by strong winds, heavy precipitation, and storm surges. They predominantly affect tropical coastal areas, where they can cause significant annual damage, estimated at US$26 billion in the United States alone Bakkensen and Mendelsohn [2019]. However, recent scientific evidence indicates a notable poleward shift in TC distribution. This shift is attributed in part to global climate warming and ocean temperature rise, which create conducive conditions for the formation and propagation of TCs into higher latitudes Kossin et al. [2014], Kossin [2018]. As TCs extend into higher latitudes, they introduce new challenges and hazards. These areas are less accustomed to such extreme weather events, and their populations, infrastructure, and ecosystems may be poorly prepared to cope with them Studholme et al. [2022]. In addition to TCs occurring during warm seasons, extratropical cyclones (ETCs) develop in cold seasons in these regions. ETCs can experience slower movement as a result of atmospheric conditions, leading to an elevated likelihood of causing substantial damage Booth et al. [2021], Colle et al. [2015].

Damage resulting from TCs and ETCs is associated with various hazards inherent to these weather systems. Strong winds and low pressure accompanying these storms during landfall can induce storm surges in coastal regions, leading to coastal flooding. Heavy rainfall can result in inland freshwater flooding. At times, both forms of flooding can occur simultaneously, resulting in a compound event that combines storm surge and rainfall-driven flooding. The intricate interplay between these two sources of flooding often results in compound flooding events that exhibit greater destructive potential compared to individual occurrences of either surge or rainfall-driven flooding Wahl et al. [2015].

In a warming climate, several factors may contribute to changing potential for compound flooding events resulting from TCs and ETCs. It is well-established that the intensity of rainfall associated with these storms is likely to increase. This escalation is primarily driven by higher saturation vapor pressure of water, as dictated by the Clausius-Clapeyron equation Liu et al. [2019]. Furthermore, the movement of TCs toward higher latitudes, alterations in their translational speed, and modifications in the behavior of ETCs all contribute to the altered hazards associated with these storms Kossin [2018], Booth et al. [2021]. Additionally, rising sea levels further exacerbate the impact of compound flooding events, necessitating a comprehensive evaluation and mitigation of the associated risks Strauss et al. [2021], Marsooli et al. [2019], Lin et al. [2019, 2016]. It is important to gain a deeper understanding of how these alterations in storm characteristics, manifesting within a warming climate, may reshape the risk of compound flooding resulting from these storms. This is particularly vital in regions unaccustomed to such cyclonic activity, as this knowledge is essential for enhancing preparedness, facilitating adaptation, and formulating mitigation strategies aimed at reducing the potentially devastating damages and causalities associated with these events.

One significant challenge associated with TCs is the limited availability of comprehensive records of these storms. The most reliable records we can obtain date back only to the early satellite era, starting in the 1980s. However, for ETCs, reanalysis data provide a more extensive historical records, likely reliable back to 1900. This extended dataset allows for a more robust analysis of trends and patterns over a longer period for ETCs.

The timeframe for relibale TC dataset is relatively short, and for specific regions, some landfalling storms may not have been recorded, exacerbating the issue. Consequently, when attempting to employ historical records to quantify the risk of compound flooding from these storms, a significant degree of uncertainty arises due to the brevity of the dataset and the paucity of observations. Even if more extended records of these storms were available from the past, they may not be representative of today's climate, primarily due to the influence of climate change. It is important to emphasize that even contemporary climate records do not provide an accurate representation of future conditions, again owing to ongoing climate change. Therefore, any statistical risk assessment method relying solely on historical statistics may fail to accurately quantify the risk. Infrastructure or adaptation planning based on such methodologies can thus lead to vulnerabilities and significant damages. To address this data limitation and account for the evolving climate, we employ a physics-based risk modeling framework Sarhadi et al. [2024]. This framework is driven by the atmospheric and ocean climatology of reanalysis data and General Circulation Models (GCMs) Emanuel et al. [2006, 2008], Komurcu Bayraktar et al. [2018]. It enables the downscaling of TCs and ETCs across past, current, and future climate scenarios. This approach helps address the dearth of observations and provides insights into how these storms may evolve under a warming climate, consequently shedding light on how the risk of compound flooding in coastal areas at higher latitudes may change. Here, the term 'risk' is used to denote the statistical frequency of flood events as characterized by their return periods, which correspond to the inverse of the annual exceedance probability.

Compound flooding arises from the complex interplay between storm surge and heavy rainfall-driven inundation, manifesting across both spatial and temporal dimensions. It is important to meticulously model this intricate hydrodynamic interaction between the two sources of flooding, distinguished by their surge and rainfall characteristics, with a high level of temporal and spatial precision. In recent years, there has been a growing focus on modeling intricate coastal hydrodynamics. Commonly, statistical methodologies are used to assess flood hazard by establishing joint statistical distributions that capture interdependencies among various flooding drivers, often at localized or gauge scales Gori et al. [2020], Wahl et al. [2015], Moftakhari et al. [2017], Gori and Lin [2022], Zhang and Najafi [2020]. However, these methods have limitations, primarily stemming from their inability to account for the complex dynamic interactions between storm surge and rainfall-driven flooding. These approaches rely heavily on statistical measures of dependence, which can introduce uncertainties. Moreover, they often overlook hydraulic dynamics of compound flooding, which involves integrating surge height and rainfall intensity to determine flooding levels while considering their compounded effects. The prevailing statistical practices, which often treat the drivers of compound flooding (rainfall intensity and surge height) through joint distributions rather than considering the actual hydraulically driven flooding, result in imprecise compound flooding hazard and risk assessments. Numerous studies have explored coastal flooding stemming from TCs and ETCs through the utilization of physics-based modeling methodologies Marsooli et al. [2019], Gori et al. [2020], Emanuel [2017], Lin et al. [2019]. However, the majority of these studies have primarily focused on single hazard scenarios, such as rainfall- or surge-induced flooding, or on combining separate hazards. Therefore, these approaches may underestimate or overestimate flooding hazard frequency compared to models that account for the hydrodynamics of compound flooding. In our study, we employ an innovative approach designed to overcome the lim-

itations often associated with these conventional methodologies. Our method utilizes a physically-based numerical hydrodynamic model, allowing for the explicit simulation of compound flooding. This is accomplished by concurrently converting key driving factors, such as wind speed and rainfall intensity, into hydraulic-based flood simulations, providing a high level of temporal and spatial resolution to comprehensively capture the complex interplay between surge and rainfall-driven flooding during the landfall of TC or ETC storms.

By utilizing a state-of-the-art dataset of downscaled storms, combined with an understanding of the climatology of these storms and projected SLR in the current and future warming climate, we can evaluate the potential evolution of compound flooding risk in coastal areas. This approach also allows us to identify the primary drivers that may intensify the risk of compound flooding. Such information can furnish a detailed granular perspective on the risk of compound flooding in coastal regions, enabling authorities to enhance their preparedness and adaptation strategies for coastal cities and communities. This proactive approach is crucial for mitigating damages in the current and future climates.

2 Dataset and methodology

2.1 Synthetic Tropical Cyclone Model and Datasets

To comprehensively address the multiple hazards associated with TCs, we initiate the process by creating synthetic TC events using the methodology detailed in Emanuel et al. 2006, 2008. This method employs deterministic and numerical downscaling to generate synthetic TCs by introducing random seeding, both in terms of their spatial and temporal characteristics, across the entire Atlantic Ocean basin. The initial wind intensity of these seeded TCs is determined through a deterministic calculation, utilizing a high-resolution, coupled ocean-atmosphere TC model. This model is driven by the thermodynamic conditions of the ocean and atmosphere, taking into account various factors, including monthly mean sea surface temperature, atmospheric temperature, humidity, and daily interpolated horizontal winds at altitudes of 250 and 850 hPa Emanuel et al. [2008].

It's important to note that any storms failing to intensify to wind speeds exceeding 21 m/s (equivalent to 40 knots) are excluded from the dataset. In a natural selection process, only seed vortices encountering favorable large-scale environmental conditions intensify into TCs, with their development timing synchronized with environmental climatic patterns. The intensity of TCs is determined through the employment of the Coupled Hurricane Intensity Prediction System (CHIPS), which is an axisymmetric hurricane model coupled to a 1D ocean model Emanuel et al. [2004]. For the purposes of this study, we fix the initial condition of the TC outer radius at 400 km, however, apart from this, the structure of the vortex, including the radius of maximum winds, evolves by the model physics. The dynamic downscaling method enables the simulation of numerous synthetic TC events, driven by bias-corrected climate reanalysis or projections from CMIP6 GCMs. Throughout the entire lifespan of each synthetic TC, we consistently record key meteorological parameters, including maximum surface wind speed, central pressure, and the radius of maximum winds. These parameters are saved at 2-hour intervals. Subsequently, a hydro-

dynamic model known as GeoClaw Mandli and Dawson [2014] is employed to simulate wind-induced storm surges with high temporal resolution along the coastline near the study area during the landfall of each synthetic TC (further details on this modeling process can be found in the provided reference).

In addition to generating primary drivers for storm surges from synthetic TCs, we also generate high-resolution hourly rainfall intensity data at a spatial resolution of approximately 20 meters for the vicinity of the study area during the landfall of each synthetic TC using a Tropical Cyclone Rainfall (TCR) model Feldmann et al. [2019]. TCR, a physics-driven model, links convective rainfall in TCs to the TC vortex's vertical velocity, accounting for factors such as frictional convergence, topography, vortex stretching, baroclinic effects, and radiative cooling. Previous studies have applied TCR in hazard frequency assessments Emanuel [2017], Gori and Lin [2022] and validated it against observed TC-related rainfall in the United States Feldmann et al. [2019], Xi et al. [2020]. These studies demonstrated TCR's accuracy in replicating coastal rainfall patterns but noted limitations in inland and mountainous areas. To assess the accuracy of this rainfall dataset, Feldmann et al., 2019 conducted an evaluation by comparing it with observed rainfall data obtained from the NEXRAD radar network and rain gauges across the eastern United States. This high-resolution, hourly rainfall intensity data plays a critical role in quantifying the rainfall-induced hazard, a key component contributing to the compound flooding processes.

The downscaling process is implemented for six distinct CMIP6 climate model simulations: CESM2, CNRM-ESM2-1, EC-EARTH3, IPSL-CM6A-LR, MIROC6, and UKESM1-0-LL, all operating under the SSP3-7.0 scenario. Synthetic TC tracks are generated for two different time periods: the late 20th century, spanning 1971-2000, and the end of the century, from 2071-2100, using the climate model simulations. The whole dataset comprises approximately 46,800 synthetic storms, with approximately 3,900 synthetic storms generated from each climate model in each period. Furthermore, we repeat this process to generate 4,100 synthetic storms based on NCEP reanalysis data, representing the late 20th century (1979-1999) and current climates (2000-2020). In total, these datasets encompass a large set of synthetic TCs, with their centers passing within 300 km of the New Bedford city in the study area. The TC downscaling technique described here does handle some features of extratropical transition. Namely, the effects of increasing background flow and shear can contribute substantially to surface winds generated by the technique. On the other hand, there can be no feedback of the TC back onto the environmental flow, except indirectly as entailed in the beta-drift component of storm translation. Some, and perhaps most of our synthetic TC events might be considered by forecasters to be undergoing extratropical transition by the time they affect Buzzards Bay, Massachusetts. We here make no attempt to distinguish between such events and other events more nearly resembling classical TCs. Later, when we consider ETCs, we will attempt to filter out TCs by confining our attention to the colder months of the year.

2.2 Extratropical cyclone datasets

The method described above, which involves statistically and deterministically downscaling TCs, enables the simulation of a vast number of idealized synthetic TC events based on climate reanalysis or climate model simulations Emanuel et al. [2008]. This is possi-

ble, to a reasonable extent, because the feedback of TCs on the surrounding large-scale environment does not significantly impact their subsequent evolution. For example, TC tracks are primarily determined by the large-scale flow in which they are embedded (and, to a lesser extent, by the beta drift effect), which passively advects them Emanuel et al. [2006], irrespective of the TC's internal evolution. Additionally, this method employs analytical simplifications, such as assuming axisymmetry and moist slantwise-neutrality in the free troposphere, which reduces the downscaling model to a single radial dimension, making it computationally efficient, even at high radial resolution.

However, for ETC events, it is not feasible to neglect the effects of the storm on the large-scale environment. Therefore, it is not possible to generate additional synthetic ETCs within a given global climate model run. Only storms explicitly simulated in these runs can be dynamically downscaled. At present, there are no reduced-dimension models that can be used to dynamically downscale ETCs, so computationally expensive regional climate models like the Weather Research and Forecasting (WRF) model Komurcu Bayraktar et al. [2018] are required to provide high-resolution information on the behavior of ETCs for risk assessment. Due to the difficulty and computational cost associated with simulating a large number of downscaled ETC events, we do not attempt to do this ourselves. Instead, we utilize state-of-the-art WRF dynamical downscaling data described in Komurcu et al., 2018. These downscaling simulations were developed to support regional climate studies in the northeastern U.S. They downscale CMIP5, RCP8.5 projections by CESM v1.0, which have been bias-corrected to support climate research. The WRF data used here covers two different time periods: the 2006-2020 current climate period and the 2081-2100 end-of-the-century period, with hourly time resolution. Additionally, we use the output of a 2006-2015 WRF simulation to downscale ERA-Interim reanalysis data Dee et al. [2011], which aids in verifying our model. The WRF simulations employ nested domains on a Cartesian grid, with the innermost domain covering 1500 km by 1200 km and using uniform convection-permitting 3 km resolution. To simulate rainwater flooding and storm surge in the study area, we require downscaled precipitation rates, surface pressure, and surface winds, which must be transformed from the WRF Lambert conformal conic projection to the geographical coordinates used in the hydraulic and surge models. More detailed information can be found in Sarhadi et al. 2024.

To assess the hazard associated with compound flooding, we compile a catalog of potential freshwater and surge flooding events linked to ETCs for each downscaled period. To identify potential freshwater flooding events, we calculate time series of rainfall intensity averaged over the area extending from -71.2 to -70.5 W and 41.5 to 41.9 N for each historical and future period. Potential freshwater flooding events are selected iteratively by searching for rainfall intensity maxima in the time series in decreasing order, starting from the global maximum. Each event extends from four days before to one day after the selected local maximum. Once an event is defined, its full time-span is removed from the time series so that the next, slightly weaker event selected is the most intense remaining event in the time series. The total number of events selected in each downscaled period is equal to five times the number of years in the corresponding period. Similarly, to identify potential surge flooding events, we select maxima in a time series of the wind component oriented toward the coast averaged over a $2^\circ \times 2^\circ$ box off the coast of the western Buzzards Bay area. It's important to note that the instantaneous precipitation

intensity averaged over the study area and the average wind component oriented toward the coast are only rough predictors of freshwater and storm surge flooding. However, the number of selected rainfall and wind events is sufficient to ensure that all events capable of producing significant freshwater or surge flooding are included. To minimize the inclusion of TCs, our focus is on ETC events occurring from October to May. However, we acknowledge the potential for some overlap between TCs and ETCs in early October. Accurately differentiating ETCs from extratropical-transitioned TCs in dynamically downscaled simulations requires a nuanced understanding of atmospheric dynamics and storm structure. This area necessitates further exploration in future studies.

2.3 Storm surge modeling

Consistent with previous research Reed et al. [2015], Lin et al. [2016], Garner et al. [2017], we define a storm surge as the anomalous elevation of sea level above Relative Sea Level (RSL). This elevation results from the low atmospheric surface pressure and the high surface wind speed associated with TCs or ETCs. The combination of storm surge and RSL fluctuations characterizes the surge height in coastal regions caused by TCs and ETCs. Our RSL estimation is based on the local average of the total sea level throughout each climate period. RSL also serves as the key factor for distinguishing between land and water elevations. As a result, we disregard interannual sea level variations and the relatively minor nonlinear interactions between the surge and RSL, as outlined in prior studies Lin et al. [2016]. Furthermore, astronomical tides are not factored into our calculations. It is important to note that future studies should investigate the effects of tides and their nonlinear interactions with surges, particularly in light of potential changes due to SLR Müller [2011], Garner et al. [2017].

To simulate storm surges generated by synthetic TCs and ETCs, we utilize the GeoClaw numerical model, which relies on high-resolution shock-capturing finite volume methods. GeoClaw utilizes the classical shallow water equations enhanced with additional source terms to accommodate various physical processes, such as bathymetry effects, bottom friction, wind friction, non-constant surface pressure, and Coriolis forcing. Further details on the numerical modeling approach can be found in Mandli & Dawson 2014. Unlike finite-element unstructured hydrodynamic models Colle et al. [2008], Westerink et al. [2008], GeoClaw incorporates Adaptive Mesh Refinement (AMR) algorithms Berger et al. [2011], Mandli and Dawson [2014], enabling efficient computational solutions at high resolutions over large scales. We implement a broad domain, covering approximately 1000 kilometers, to better quantify the large-scale impact of various attributes of TCs and ETCs, including intensity, duration, size, and landfall location, on storm surges. GeoClaw, which conventionally employs the Holland wind field model tailored for TCs, computes near-surface winds based on specific parameters such as eye location, radius of maximum winds, and maximum wind speed. However, applying this model to ETCs, which exhibit more complex and asymmetric wind patterns, results in significant inaccuracies. To address this, we have bypassed the Holland model in favor of integrating wind speeds and surface pressures directly from dynamically downscaled WRF data into GeoClaw. This modification to the GeoClaw framework allows it to accurately process and simulate the meteorological data of ETCs, enhancing the model's accuracy and expanding its applicability to a broader range of cyclonic events.

In our study area along the coastline, we positioned synthetic gauges at intervals of approximately 20 meters to ensure comprehensive spatial coverage. This spacing was chosen with consideration for the complexity of the coastline and the desired level of detail. The selection of optimal spatial resolution was based on the need to accurately capture intricate interactions between storm surges from TCs and ETCs and land features, while also ensuring computational feasibility for analyzing a large dataset of events. Consequently, these coastal surge conditions are transformed into surge-driven flooding through a hydraulic model, allowing us to model the propagation of surges and their potential to cause surge-driven flooding in coastal areas. Furthermore, temporal resolution is less than a minute during landfall to enhance our simulation of the dynamic interaction between surge and rainfall-driven flooding. This surge simulation approach is applied to a broad set of synthetic TC and ETC events. It is worth noting that while the performance of GeoClaw in modeling TC surges has been evaluated in previous studies Miura et al. [2021], Mandli and Dawson [2014], Sarhadi et al. [2024], here we rigorously calibrated the GeoClaw model for the Buzzard Bay area, focusing specifically on adjusting the bottom friction coefficients and coastal features. The model's storm surge simulations were then evaluated against observed surge events recorded at the Woods Hole gauge. This evaluation process ensures that our model accurately reflects the local hydrodynamic conditions, providing reliable storm surge simulations for the area as discussed presently.

While the accuracy of dynamically downscaled ETCs was evaluated in a previous study Komurcu Bayraktar et al. [2018], here, we utilize the downscaled ETCs to assess their performance in surge modeling. Figure 1 illustrates the surge modeling process, which entails dynamically downscaled WRF simulations of primary surge drivers, including wind and pressure fields, forced by ERA-Interim reanalysis data. The simulation corresponds to an historical ETC event that occurred on December 27-28, 2012, within the study area. The calibrated model's performance accuracy is depicted in Figure 1. The simulated surge, using the modified GeoClaw model, demonstrates a robust agreement with observed surge levels. These observed surge values were obtained by de-tiding water levels, a procedure that involves subtracting water elevation from NOAA tide predictions at the Woods Hole gauge.

For modeling surges generated by TCs and ETCs during the late 20th century and in the current climate, we rely on RSL data obtained from NOAA gauge observations. However, in the context of future climate scenarios, we incorporate SLR projections derived from CMIP6 under the SSP3-7.0 scenario into GeoClaw using a 'bathtub' approach. The bathtub approach treats the water body as a static entity, where the sea level rises uniformly, akin to water filling a bathtub without any waves or currents. This approach calculates flood depths by modeling the impact of elevated water levels over complex topographical features Kasmalkar et al. [2024], Shepard et al. [2012]. Due to its simplicity, the bathtub approach is easier and faster to apply in predictive SLR modeling within hydrodynamic contexts and requires less computational power. We integrate this approach into the GeoClaw model, where we incorporate elevated water levels (from projected SLR) across the entire computational domain. This adjustment enables the hydrodynamic model to simulate storm surge along the coastline with these elevated sea levels. This integration allows us to assess the effects of rising sea levels on compound flood inundation caused by TCs and ETCs, as well as their associated hazard landscape under current and future climates. This approach provides a robust framework to quantify the evolving

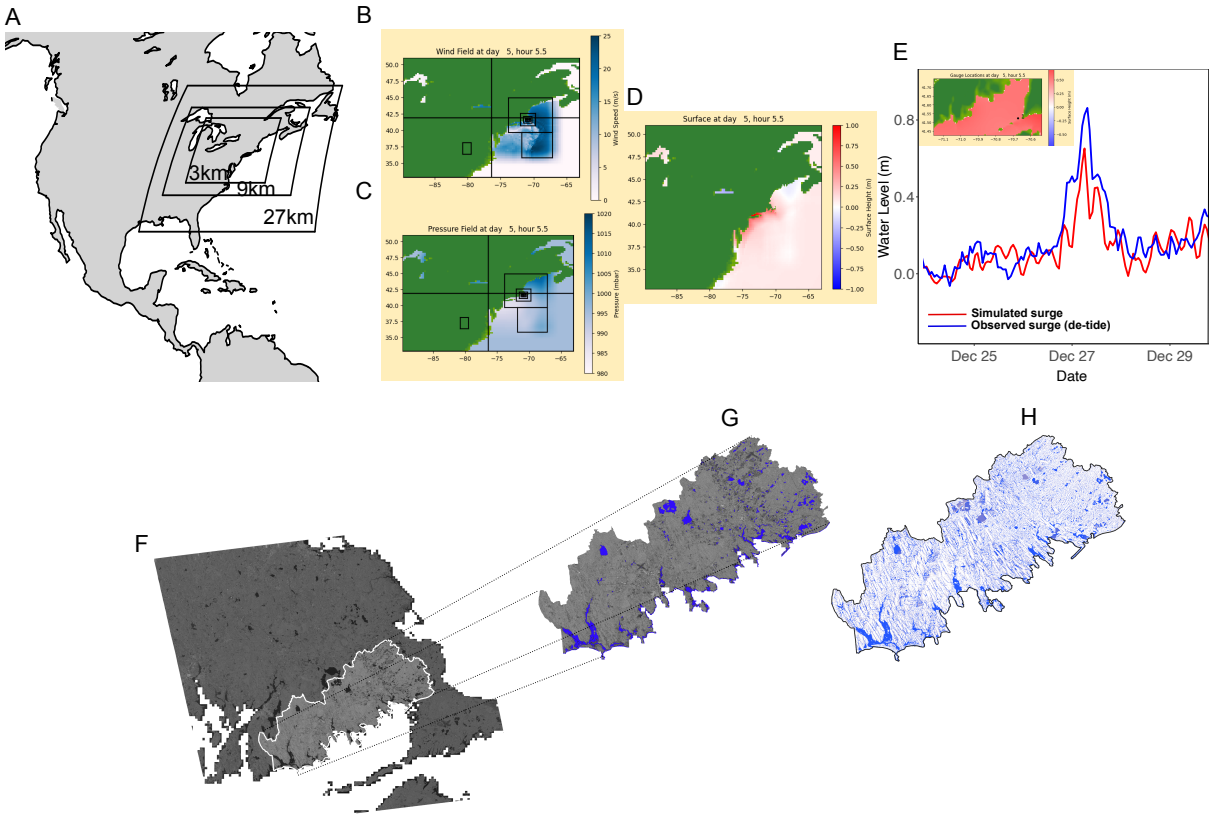

Figure 1: Surge simulation process for ETCs using dynamically downscaled WRF simulations of primary drivers (wind speed and sea level pressure fields) in the study area and evaluation of flood simulation from the LISFLOOD-FP model compared with detected flood inundation mapping from Sentinel-1 images during Hurricane Michael, 2018. (A) Three nested grids with spatial resolutions of 27, 9, and 3-km used for dynamically downscaling WRF simulations (in this study, we focus on the 3-km spatial resolution domain). (B-C) Hourly wind and pressure fields downscaled via WRF simulations driven by ERA-Interim reanalysis for an ETC event occurred on 27-28th December 2012. (D) Simulated surge height (in meters) from the ETC at the regional scale using modified GeoClaw. (E) Performance evaluation of GeoClaw for the ETC storm (the blue line represents observed surge heights during the landfall of the ETCs, calculated by de-tiding water levels, with water elevation subtracted from NOAA tide predictions at the Woods Hole gauge. The red line represents surge heights simulated by GeoClaw. Note that the temporal resolution on the x-axis is six minutes). (F) Sentinel-1 SAR image captured during Hurricane Michael, 2018, from the study area on 12 October, 2018. (G) Detected flood inundation (blue color) from Hurricane Mihael in the watershed of the study area after image corrections. (H) Simulated flood inundation map from the same hurricane using the LISFLOOD-FP model.

hazards of storm surges and compound flooding due to SLR. Future projected sea levels involve the ensemble mean of total SLR over future climate scenarios Fox-Kemper et al.. These projections encompass comprehensive considerations, including the contributions of Antarctic and Greenland ice sheets, glacier dynamics, thermal expansion of seawater, terrestrial water storage, vertical land motion, and the potential influences of marine ice cliff instability.

2.4 Numerical compound flood modeling

To simulate the intricate hydrodynamic interactions involved in compound flooding, a confluence of storm surges and heavy inland rainfall-driven flooding stemming from synthetic TCs and ETC events, we modified a version of the LISFLOOD-FP model. This two-dimensional hydraulic model, renowned for its high spatio-temporal resolution, is recognized for its computational efficiency. The two-dimensional base model, employs an explicit forward difference scheme on a staggered grid. The model is structured around two fundamental hydrodynamic equations: the continuity equation, which ensures mass conservation within each computational cell, and the momentum equation, which governs the flow dynamics between cells. This setup allows for the accurate simulation of fluid motion and mass transport in hydrological contexts. A detailed description of this model is provided in Neal et al. 2012. LISFLOOD-FP employs an explicit finite difference scheme to simulate shallow water waves, while deliberately omitting advection Bates et al. [2010]. The efficacy of the fundamental model's numerical scheme in simulating pluvial and fluvial flood dynamics has been substantiated by various studies Neal et al. [2012], Wing et al. [2022], Bates et al. [2021]. In our work, this model has been customized to incorporate high-resolution surge height data (simulated by GeoClaw) along the coastline, and simultaneously, it accommodates hourly rainfall intensity data from storm events in the inland regions as boundary conditions. In our simulations, the spatial resolution is approximately 20 meters, matching the resolution of the Digital Elevation Model (DEM) used. We conduct simulations at high temporal resolutions, less than a minute, similar to storm surge simulations, and perform mass conservation checks every 20 minutes. These frequent checks help maintain accuracy in mass flow and storage calculations throughout the simulation. This physically based approach empowers the model to replicate the dynamics of compound flooding in response to the rapid spatio-temporal fluctuations in surge and rainfall driven flooding during the landfall of each storm. The model ensures the conservation of mass within each grid cell and maintains the continuity of momentum of compound flooding between neighboring cells. The model recalculates the flow depth, taking into account the elevation of each cell, water surface slope, surface Manning's roughness coefficient, and acceleration due to gravity. More details about the methodology can be found in Sarhadi et al. (2024).

It is important to note that the geodetic datum of NAD83 is utilized to establish the spatial coordinates, while the vertical datum of NAVD88 is used for elevation values within the applied DEM. In our study, we utilize a LiDAR-based DEM, employing a geographic (Lat/Lon) projection to represent the area's geometry. The land-use of the study area Dewitz [2021] is employed to quantify surface roughness, and a map of available soil water storage for the topsoil layer (0-50 cm) with the same spatial resolution is used to account for the infiltration rate in non-constructed areas. The source of these input files is given in the data availability section.

We evaluated the accuracy of the LISFLOOD-FP model using calibrated input parameters to simulate rainfall-driven flooding in inland areas and compound flooding in coastal areas during Hurricane Michael, 2018. For these simulations, we incorporated observed hourly rainfall intensity from the NEXRAD radar data NCEI [2018] and the IBTrACS dataset Knapp et al. [2010, 2018] specific to Hurricane Michael to simulate the flood extent. Additionally, we utilized Sentinel-1 Synthetic Aperture Radar (SAR) satellite imagery during Hurricane Michael to detect the observed areas of flood inundation. SAR technology is advantageous as it can penetrate cloud cover and accurately identify inundated areas under any weather conditions, whether day or night. After applying multiple corrections, including orbital file corrections, radiometric and geometric calibrations, and the generation of backscatter images Navacchi et al. [2022], we detected the observed flood inundation extent during Hurricane Michael (Figure 1(F-H)). This enabled us to compare the simulated flood inundation from the calibrated LISFLOOD-FP model with the observed inundation extent detected from the SAR image captured during the hurricane's landfall for evaluation purposes. Comparisons between these observed flood extents and simulated flood extents (above 5cm) revealed more than 76% overlap. Given that the SAR image was not captured at the peak of the event, this high degree of overlap demonstrates that our calibrated hydraulic model exhibits robust performance and accuracy in simulating floods across both coastal and inland regions of the study area, as shown in Figure 1(G-H).

In this process, the hydrodynamics of compound flooding during the landfall of each storm are simulated in detail, capturing all relevant physical interactions and dynamics with high temporal and spatial resolution. We then store the maximum compound flooding level at each grid cell for every individual storm event. This process is iteratively conducted for a vast set of TCs and ETCs derived from reanalysis and climate models. These maximum flood records serve as a reflection of the compound flooding behavior over each defined time period for every grid cell. Subsequently, these records are fundamental in constructing a nonparametric empirical Cumulative Distribution Function (eCDF). This approach leverages the theory of nonexceedance probability to determine the return period of a compound flooding event at each grid cell. The calculation is expressed as:

$$T_H(h) = \frac{1}{P(H > h)} \tag{5}$$

In this equation, $P(H > h)$ signifies the annual probability that the compound flooding level of an event (H) exceeds a specific threshold (h), and $T_H(h)$ corresponds to the return period of that particular event. The ensemble mean of compound flooding levels for TCs and ETCs at various return periods is then computed by considering multiple climate models across distinct time periods. The assessment of expected changes in compound flooding levels at specific return periods is carried out by evaluating the disparities between the ensemble mean of flood levels in future climate scenarios and those in past or current climate conditions. To dissect the individual and collective influences of changes in storm climatology and SLR on the granular hazard of compound flooding, our approach involves running the hydraulic model twice for each individual storm. This includes one simulation with the incorporation of SLR and another without it. This approach allows us to discern and quantify the distinct and synergistic effects of variations in storm climatology and SLR on the hazard of compound flooding. To distinguish the contribution of each individual hazard (surge or rainfall-driven flooding) in compound flooding from

each storm, we can simply run the model with only one driver as the boundary condition.

3 Results and Discussion

3.1 Impact of primary driver severity on compound flooding

Here, we evaluate the influence of the primary drivers during the landfall of TCs on the magnitude and extent of inundation associated with compound flooding in the study area. This assessment is pivotal for gaining a comprehensive understanding of the intricacies inherent in flood hazards stemming from these meteorological phenomena. High wind speeds and low atmospheric pressure during the landfall of TCs lead to storm surge-driven flooding along coastal regions. Specifically, the greater the wind speed, the more intense and higher the storm surge becomes both before and during landfall. Concurrently, rainfall intensity during landfall contributes to rainfall-driven flooding. The interplay between these factors, as elucidated in this study, sheds light on the intricate mechanisms that underpin the devastating consequences of compound flooding induced by TCs. The severity and dominance of each primary driver determine the corresponding severity of the compound flooding hazard. Depending on which primary driver predominates, it may result in scenarios such as compound flooding with a dominant surge in coastal areas, a situation where rainfall-driven flooding in inland areas is more pronounced, or instances when both drivers are strong, leading to a severe compound flooding event characterized by both surge and rainfall-driven inundation.

By examining the magnitude of these primary drivers, our study offers essential insights into the dynamics of compound flooding, encompassing factors like magnitude and the extent of inundation. To illustrate this, we selected two TCs as case studies to demonstrate how the magnitude of primary drivers can affect the resulting compound flooding. Figure 2 (top panels) presents information on the primary drivers of these two synthetic TC storms, which were derived from downscaling NCEP reanalysis data for the current climate (2000-2020). These measurements are presented both prior to landfall and at the time of landfall.

In the first case, represented by synthetic track #1337 (Fig. 2, A and B), the primary drivers include strong wind speeds (knots) at the eye of the TC before and during landfall, with rainfall intensity reaching up to 90-120 mm/hr in certain grid cells and an average wind speed of 40 knots (though it's important to consider the duration of high wind speeds too). These primary drivers result in flooding depths of up to 3 meters in some low-land coastal and inland areas. In contrast, the second case, depicted by synthetic track #1339 (Fig. 2, C and D), exhibits lower rainfall intensity, with the upper tail reaching up to 10 mm/hr, and wind speeds at the eye barely reaching 40 knots in the upper tail. These conditions result in significantly lower flooding levels, particularly in inland areas, due to reduced rainfall intensity. Additionally, the extent and magnitude of compound flooding in coastal areas are diminished compared to the first case, attributable to lower wind speeds and rainfall intensity.

This understanding offers a comprehensive and scientifically robust exploration of the relationship between the magnitude of primary drivers—specifically, rainfall intensity and surface wind speed—and the resulting complex dynamics of compound flooding.

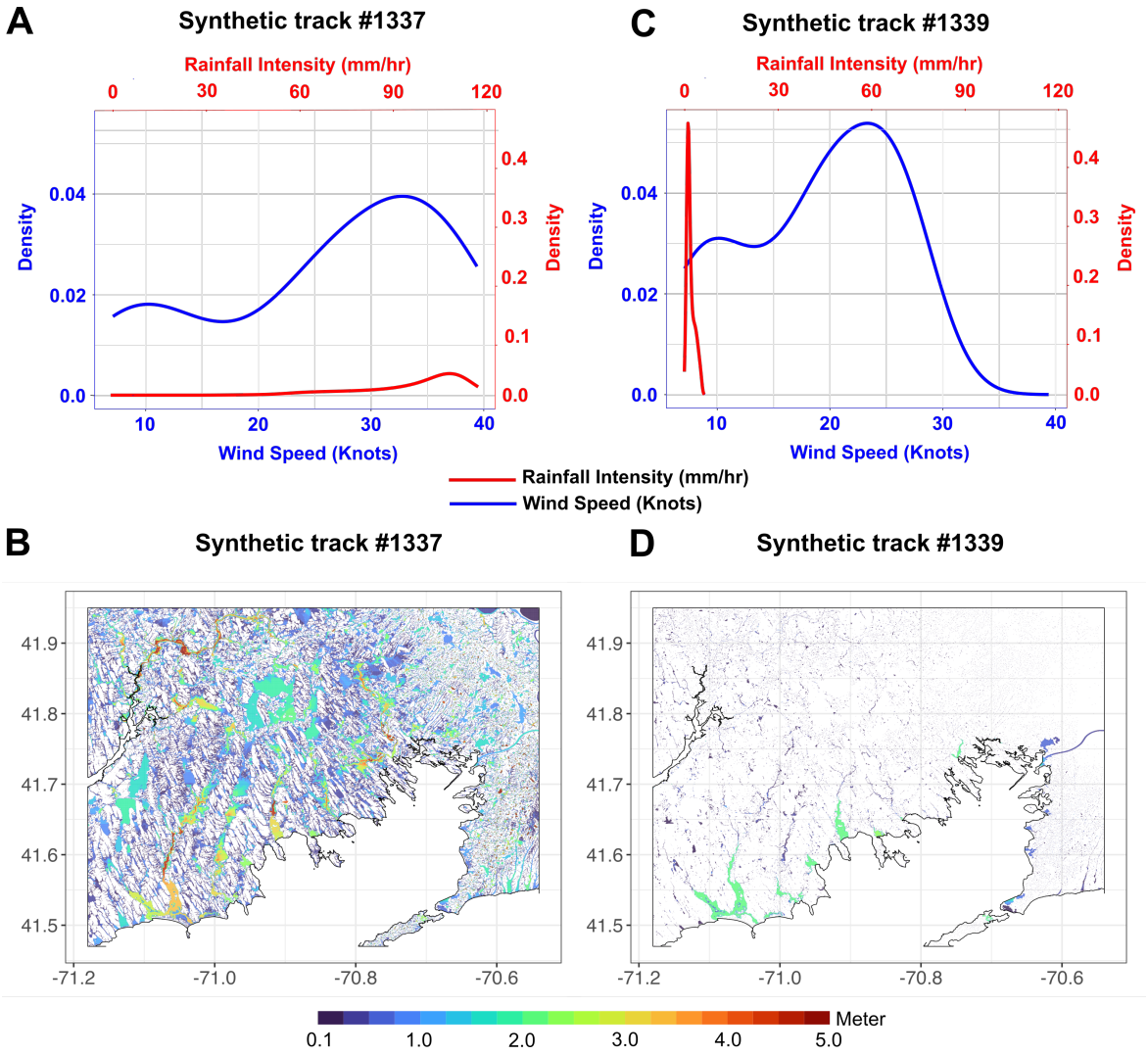

Figure 2: Impact of key drivers of compound flooding, such as rainfall intensity and surface wind speed. The top panels include the Probability Distribution Function of rainfall intensity (mm/hr) at each grid cell during landfall and the maximum surface wind speed (knots) at the eye of synthetic TC tracks, both before and at the time of landfall, for two selected synthetic TCs in the current climate downscaled by NCEP reanalysis data. The lower panels depict the corresponding compound flooding response for the two synthetic TCs. (A and B) show the drivers and compound flooding for TC track #1337, while (C and D) show the same results for synthetic TC track #1339.

These insights are invaluable for advancing our understanding of the multifaceted flood hazards associated with TCs, which, in turn, contribute to a more informed and resilient approach to disaster preparedness. Using this approach, one can easily quantify the proportion of each individual hazard and analyze the dynamic interplay between them in generating compound flooding, with high temporal and spatial resolution. Notably, the same methodology can be readily applied to ETC storms. This deeper understanding supports improved forecasting, risk assessment, and preparedness measures in vulnerable coastal regions, ultimately enhancing resilience against the impacts of these storms. In the subsequent section, we delve into the contribution of each individual and compound hazard to the risk assessment and emphasize the significance of a physics-based approach to compound flooding.

3.2 Assessing the effect of tropical cyclone compound flooding

In this section, we present a comparative analysis of compound flooding, delineating the individual contributions of surge and rainfall-driven flooding with a focus on coastal areas. The objective is to offer a clearer understanding of the effects and potential risks associated with compound flooding. Additionally, we examine how other approaches, such as singular hazards, surge, and rainfall-driven flooding considered individually, or a linearly additive hazards approach, may lead to the underestimation or overestimation of the hazard frequency. It is important to note that our comparisons are based on the results obtained from six climate models. This approach enhances clarity by visualizing differences in various sources of flooding within the models and accounting for uncertainties among them.

To conduct the analysis, we run our model under four distinct scenarios for each TC event. First, we modeled rainfall-driven flooding using only rainfall as the boundary condition. Second, we simulated surge-driven flooding using storm surge as the driver (SLR is incorporated). Third, to capture compound flooding, both primary drivers—rainfall and surge height—were applied simultaneously as boundary conditions, along with SLR, to account for the nonlinear dynamic interplays between these two flooding types during landfall of each event. Fourth, for comparative purposes, we also calculated a scenario where we simply summed the flood levels from the individual rainfall and surge-driven flooding for each event, deliberately ignoring any dynamic interactions between these two sources of flooding during landfall. To better comprehend the impact and importance of compound flooding in risk assessment for both the late 20th and 21st century climates, we selected a specific coastal area, which is also an urban area, as depicted in Figure 3 (A). This area was chosen to predominantly consist of non-tidal ground areas, with intertidal zones excluded, facilitating a comparative hazard frequency analysis. We evaluated the risk, defined by probability of occurrence or return period, associated with single hazards: surge-driven flooding (represented in green), rainfall-driven flooding (in blue), and compound flooding, which takes into account the complex hydrodynamic interplay between these hazards at high temporal and spatial resolutions (depicted in red). We also included a linear addition of individual flooding as a commonly used approach (in brown). This comparative analysis is essential in discerning the biases that arise when individual hazards are considered separately or when the two are simply linearly combined to assess flooding hazard, without accounting for the intricate hydrodynamic interplays across time and space inherent in compound flooding. Note that for the late 20th cen-

tury period, we applied a bias correction method using quantile mapping to the levels of different types of flooding, based on the corresponding levels from NCEP reanalysis data Gudmundsson et al. [2012].

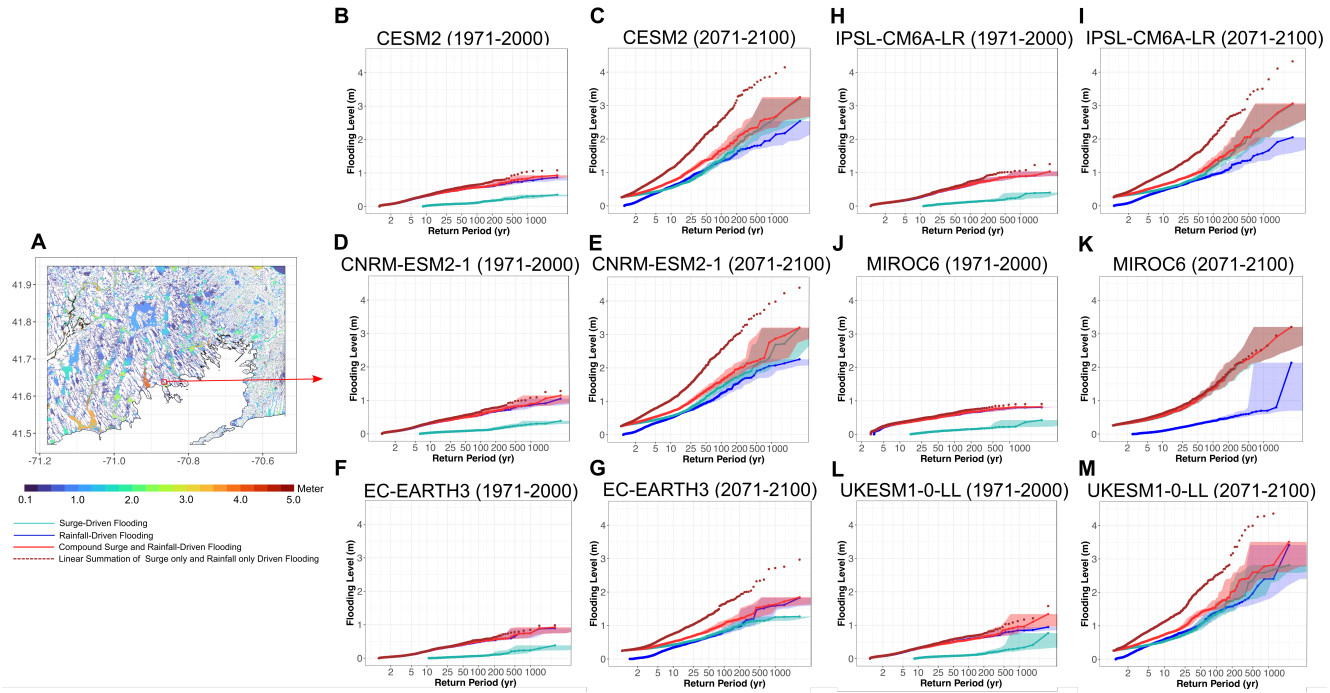

Figure 3: Comparison of compound flooding risk assessment relative to individual surge and rainfall-driven flooding, and linear addition of individual hazards. (A) Maximum compound flooding level from a randomly selected synthetic TC generated from the EC-EARTH3 model during the late 20th century, along with the location of a coastal area chosen for comparing different types of flooding. (B-C) Flooding levels as a function of the return period from various individual and compound flooding hazard sources for the selected coastal area, using synthetic TCs generated from the CESM2 model for the late 20th and 21st centuries, respectively. (D-M) Similar to (B-C) but using synthetic TCs generated from other climate models. The shaded areas in the plots represent sampling uncertainty bounds, calculated based on the 5th and 95th percentiles of a Poisson distribution within each climate model.

As depicted in Figure 3, during the late 20th century, a significant proportion of compound flooding contributions originated from rainfall-driven flooding rather than surge-driven flooding, for both high-frequency and low-frequency events in nearly all climate models. This emphasizes the hazard frequency underestimation resulting from relying solely on surge-driven flooding in this region. Conversely, the linear summation of the two individual hazards in each event, conducted in a simplistic manner and without accounting for the complex hydrodynamics of their interaction during landfall, typically results in an overestimation of compound flooding and risk across the majority of climate models. Therefore, relying solely on simple methods, such as hazard assessments based on either surge-driven or rainfall-driven flooding individually, as demonstrated here, leads to an underestimation of risk. Similarly, simply adding these two hazards together results in an overestimation of risk. Neither approach is adequate for accurately quantifying the actual level of compound flooding and the associated risk, especially in rare events. The appropriate method for assessing the hazard and the risk of compound flooding involves simulating the complex hydrodynamics between surge-driven and rainfall-driven flooding with high spatial and temporal resolution. This approach provides a comprehensive

understanding of the dynamics of compound flooding during landfall, and such detailed simulations should be the basis for any risk assessment of compound flooding in coastal areas.

Moving forward to assess the analysis at the end of the 21st century, a significant increase is observed in both individual and compound flooding hazard frequency, driven by alterations in storm climatology and SLR. Although, compared to the 20th century, the risk of both rainfall-driven flooding and surge-driven flooding increase significantly, surge-driven flooding (partially exacerbated by SLR) dominates and contributes more to compound flooding compared to rainfall-driven flooding in this area, especially for low-frequency events (with return periods above 50 years). For specific upper tail low-frequency events, there is a heightened prominence of surge-driven flooding, contributing to compound flooding, compared to rainfall-driven flooding. Additionally, the risk of compound flooding intensifies; events that previously occurred once every 100 years in the late 20th century may occur as frequently as once in 5 years by the end of the 21st century in almost all climate models. It is also worth noting that simply linearly summing the two single hazards together to assess compound flooding results in a significant overestimation of the future flood hazard frequency. For example, events that occur approximately every 500 years (factoring in the complex hydrodynamic interplay between surge and rainfall-driven flooding) are estimated to happen approximately every 75 years by the end of the century when individual hazards are simply added linearly, signifying a considerable bias and overestimation in risk assessment.

These results highlight the importance of employing a physics-based model for downscaling TCs in a future warming climate. This stands in contrast to relying solely on historical records, which do not accurately represent the characteristics of storms in a different climate, overlooking the profound impacts of climate change on TC behavior. The results also underscore the importance of considering the explicit complex hydrodynamical interplay between the individual flooding hazards in each event when assessing the hazard frequency; this interplay was neglected in previous studies Reed et al. [2015], Lin et al. [2016], Garner et al. [2017], Emanuel [2017], Marsooli et al. [2019], Lin et al. [2012]. It can lead to a severe underestimation of the actual risk in both current and future climates, with the discrepancy becoming more pronounced due to changes in climatology and SLR.

3.3 Sea level rise and tropical cyclone climatology impacts

SLR and changes in TC climatology are recognized as the primary drivers behind alterations in the risk of compound flooding in coastal regions. SLR, largely attributed to global climate change, raises the baseline water level, rendering coastal areas more susceptible to inundation. When coupled with anticipated shifts in TC climatology, including variations in cyclone tracks, intensification, frequency, and other relevant attributes, the potential for compound flooding becomes increasingly evident. In this section, we investigate the individual and compounding effects of SLR and changes in storm climatology, analyzing their influence on the risk of compound flooding during the late 20th century and the late 21st century. The late 20th century serves as a baseline for estimating historical trends, while the late 21st-century projection offers insights into warming scenarios.

Figure 4 shows the compound flooding level from a large set of synthetic tracks in the previously selected coastal area (depicted in Figure 3 (A)), both with and without SLR in the late 20th and 21st centuries, based on the output from six climate models. This analysis aims to better quantify the effect of SLR on changing the risk of compound flooding and associated uncertainty within and among different climate models. Note that compound flooding levels derived from multiple models at the end of the 20th century are bias-corrected based on compound flooding levels from the NCEP reanalysis. In the late 20th century, as depicted in Figure 4, SLR does not exhibit a discernible effect on the risk of compound flooding caused by TCs. During this baseline period, the risk of experiencing compound flooding with a 0.5-meter depth, for example, is approximately 1% per annum on average, based on the ensemble of the six climate models, both with and without SLR. As we progress towards the end of the century, changes in storm climatology, without considering the SLR effect, are projected to elevate the risk of compound flooding events. For example, this risk elevation for the same 0.5-meter compound flooding event is manifested with a 10% probability per annum, based on the CNRM-ESM2-1 model (Figure 4-D). This projection indicates that changes in TC climatology alone will escalate the frequency of such events tenfold compared to the late 20th century. However, when we consider the added contribution of SLR by the end of the century, the risk of the same compound flooding event will increase significantly. It is projected to occur approximately with a 20% probability per annum. This signifies that the combined impact of SLR and changes in storm climatology will amplify the risk twentyfold compared to the late 20th century. Furthermore, SLR alone will elevate the occurrence of such compound flooding events tenfold compared to the late 20th century and increase the annual probability of such an event to 10%. Similar intensification patterns are observed in other climate models. The intensification resulting from the combined impact of SLR and changes in storm climatology significantly amplifies the risk of low-frequency events in the late 21st century. For instance, events that historically had a return period of 1000 years in the late 20th century are projected to occur 40 times more frequently by the end of the century in the majority of the models. In terms of the depth of compound flooding events with a return period of 1000 years in the selected coastal area, the EC-EARTH3 model estimates it to be approximately 0.75 meters (ranging from 0.6 to 0.8 meters) in the late 20th century. However, by the end of the century, the depth of floods with the same return period is projected to be around 1.65 meters (ranging from 1.5 to 1.8 meters) due to the combined effects of SLR and changes in storm climatology.

Another noteworthy observation is that SLR is expected to significantly increase the risk of low-frequency events in the upper tail compared to other medium or high-frequency events by the end of the century. In a warming climate, all climate models (except EC-EARTH3 and UKESM1-0-LL) show that SLR is projected to intensify the risk significantly for upper tail events. For example, an extreme event that might occur almost once every 2000 years (based on the CNRM-ESM2-1 model) by the end of the century would have a depth of compound flooding without the impact of SLR at almost 2.4 meters. However, with SLR's impact by that time, the depth is projected to increase to around 3.3 meters in such a warming climate. This difference is smaller in medium to high-frequency events.

In addition to the impacts of storm climatology changes and SLR between the late 20th century and the late 21st century, we also analyze changes in other factors related to

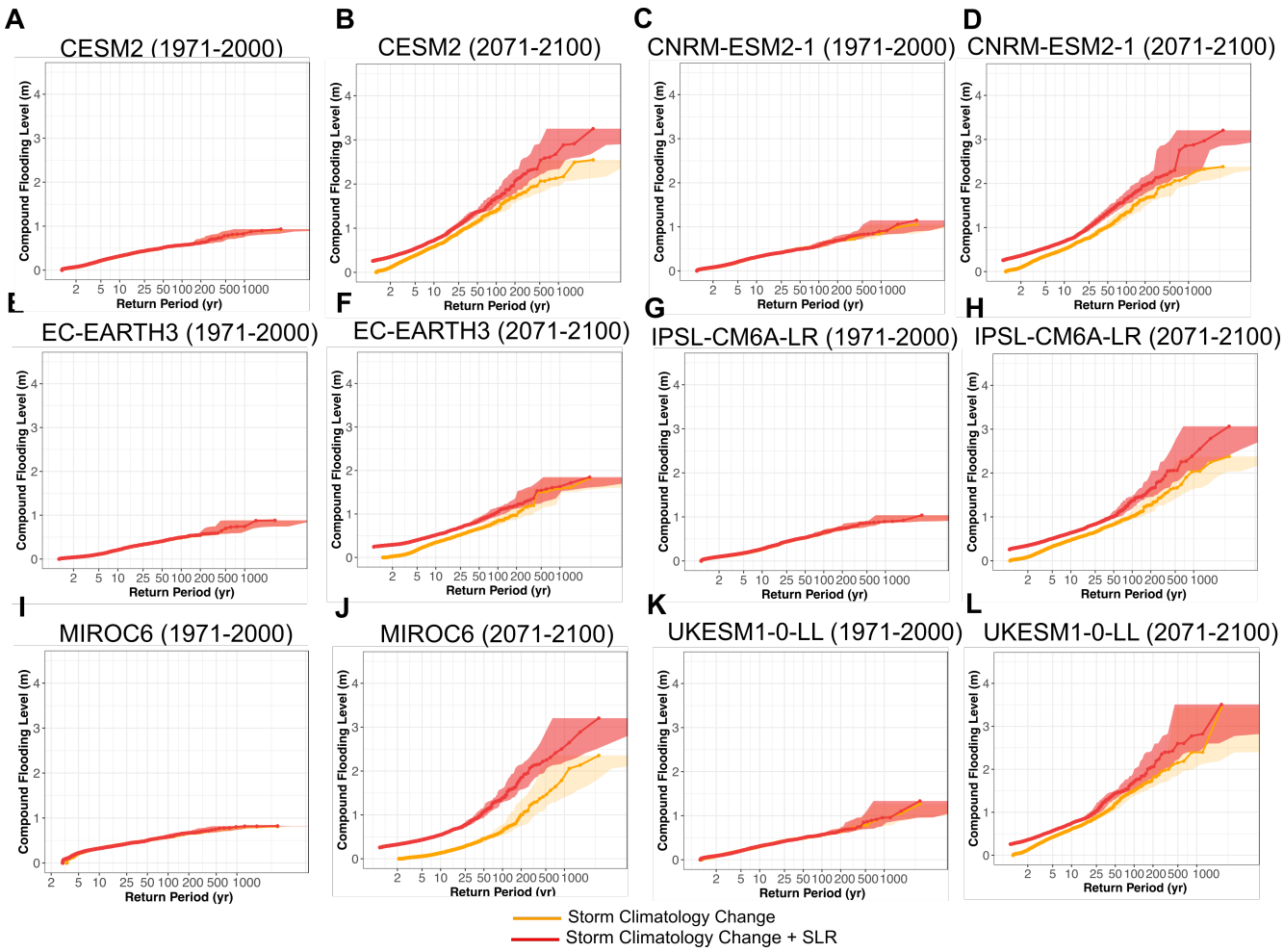

Figure 4: Assessment of the contribution of SLR and changes in TC climatology to the risk of compound flooding in the late 20th and 21st centuries, focusing on the selected location depicted in Figure 3 (A). Each line in the graph illustrates the simulated compound flooding levels derived from synthetic TCs downscaled from each of the six climate models. The shaded region represents the confidence interval, indicating sampling uncertainty, and is calculated based on the 5th and 95th percentiles of a Poisson distribution within each climate model.

TCs, including storm frequency, dynamics (upward motion), moisture, duration, and their contributions to changes in TC total rainfall. For this purpose, we employ the methodology introduced by Emanuel 2024. In this analysis, we define a 96-hour window centered on the time when the cyclone center is nearest to the point of interest (New Bedford, in this case) and calculate the total rainfall. For all storms whose exceedance frequency of total rainfall is less than a specified threshold (here, less than one in 200 years, defined as low-frequency events), we calculate the contributions of each aforementioned TC factor for both the late 20th century and the 21st century. For the late 21st century (future climates), we repeat this analysis under two scenarios: first, by maintaining the overall frequency at the late 20th century climate level, and second, by letting the overall frequency equal its value in the future climate. This process is applied to event sets from multiple climate models.

Figure 5 illustrates the contributions of different TC factors with low-frequency 200-year return periods from the late 20th century to the late 21st century. The results show that the increase in total rainfall is predominantly driven by these intensified cyclones, although there is considerable variation across the models. Another significant contribution to these future rare TCs comes from an increase in moisture, with less uncertainty across models due to their agreement on temperature increase. The contribution from changing TC frequency of these rare events tends to increase, albeit with variations among the climate models. The contributions of duration and vertical motion to total rainfall also increase, but are lesser in magnitude compared to other factors by the end of the century, with considerable uncertainty among the models.

Our methodology enables us to examine and elucidate how these interacting primary drivers may influence the risk of compound flooding in a warming climate, providing valuable insights into the adaptive strategies and mitigation measures required for the late 21st century to safeguard coastal communities and infrastructure in an evolving climate. These analyses furnish detailed granular information about which primary drivers are of greater concern and how adaptive strategies can be tailored for each specific area based on priorities.

3.4 Tropical cyclone compound flooding risk in today's climate

Here, we use our methodology to quantitatively assess the impact of anthropogenic warming that has already occurred on the risk of compound flooding, specifically through TC climatology and SLR, within the context of the current climate in the study area. To achieve this, we conduct simulations to determine the maximum compound flooding levels from 4,100 synthetic TCs. These TCs are downscaled from NCEP reanalysis data for two distinct climate periods: the late 20th century (1979-1999) and the early 21st century (2000-2020). Figure 6 (A) compares the levels of compound flooding events for different return periods between these two time frames, focusing on a selected location close to the shore, containing buildings and road networks.

Our results suggest no significant changes in the risk of high-frequency events (less than 50 years) in the current climate compared to the late 20th century. However, they suggest a slight increase in the magnitude of compound flooding, characterized by return periods exceeding 50 years, under today's climate compared to the late 20th century. However, it

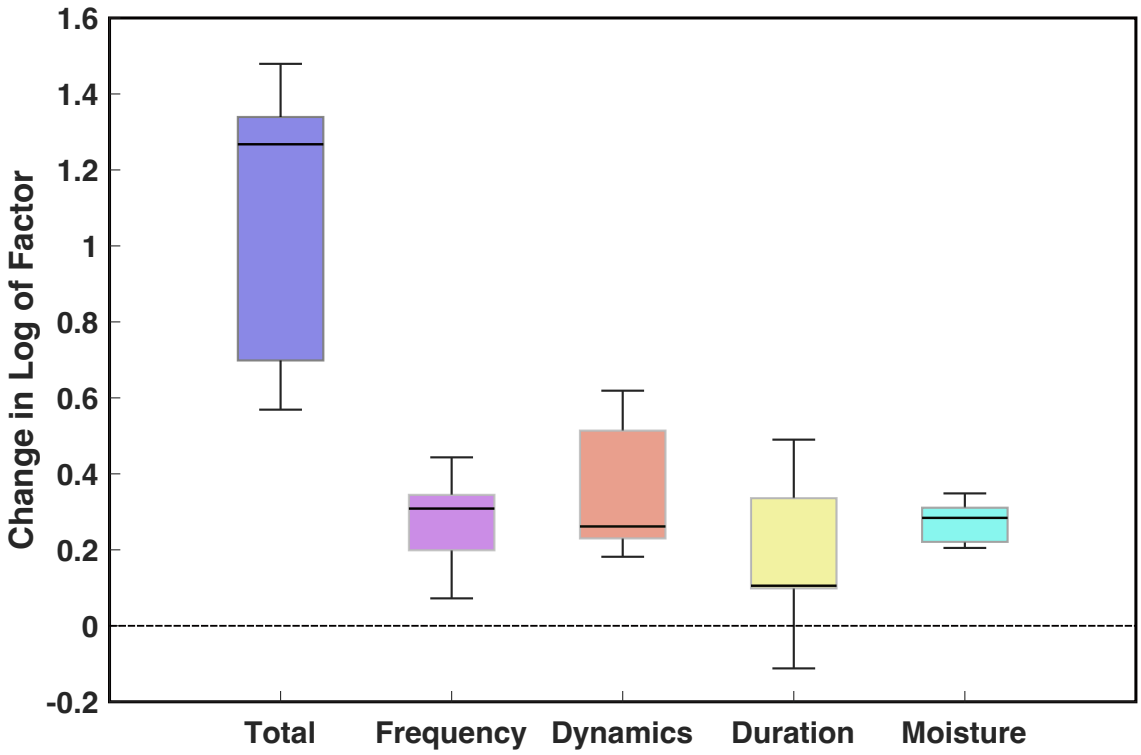

Figure 5: Changes in the logarithmic contributions of various factors to TC total rainfall at a 200-year return period, from the historical (late 20th century) to the future climate (late 21st century). The boxplots extend from the lower to the upper quantiles of the distribution across multiple climate models, with the horizontal line representing the multimodel median.

is important to note that distinguishing distinct trends for these events proves challenging due to sampling uncertainties.

In Figure 6 (B), we present the spatially distributed hazard of compound flooding events that occur once every 100 years, or with a 1% likelihood in any given year, across the entire study area. Notably, there is no observed decreasing trend in flooding levels for such events within the region. The results indicate that changes in TC storm climatology, particularly increased rainfall in the current warming climate relative to the late 20th century, have raised flooding levels by up to 0.4 m in low-lying coastal and inland areas, although this increase is not significant given the sampling uncertainty shown in Figure 6 (A). While SLR is also considered as a contributing factor, it does not have a significant impact on compound flooding levels. Therefore, the majority of changes, especially in inland areas, are primarily attributed to changes in TC climatology.

3.5 Tropical cyclone compound flooding risk in a warming climate

Here, we conduct a comprehensive analysis of compound flooding risk associated with TCs, focusing on how this risk may evolve in a warming climate. Our investigation considers changes in TC climatology and SLR across different time periods. To understand the temporal evolution of compound flooding risk in our study area, we center our analysis on a specific location near New Bedford City, as indicated in Figure 6 (A). Our aim is to illuminate the changing dynamics of compound flooding depths in this area, drawing insights from historical data, contemporary observations, and future climate projections.

We conducted a rigorous probabilistic analysis, employing advanced mixture modeling techniques to delineate the underlying probability distributions of compound flooding for each time period. Specifically, gamma and Weibull mixture models were applied to simulated compound flooding levels from each climate model, with model selection guided by the Akaike Information Criterion (AIC) Bozdogan [1987]. To comprehensively assess inherent uncertainty, we applied bootstrap resampling techniques, generating 3,000 samples per iteration for compound flooding level simulations from each climate model across each time period. Subsequently, confidence intervals at the 5% and 95% levels were derived for key parameters associated with the fitted distribution. The frequency of compound flooding in the specified regions, attributed to changes in storm climatology and SLR, is delineated in Figure 7 through aggregated simulations involving six CMIP6 climate models. In this figure, the bold line represents the frequency of compound flooding levels within the selected area for different return periods across distinct time periods, including simulations for the late 20th and 21st centuries, as well as reanalysis data from the NCEP dataset for the current climate (2000-2020). Furthermore, the colored envelope illustrates the ensemble mean within the 5th to 95th percentile range, calculated based on the outcomes derived from the six climate models. The results (based on the ensemble mean of the climate models) indicate that compound flooding events that previously occurred with a 1% probability in a given year, in the late 20th century in this particular location, have now increased in frequency. In the current climate, these events occur with an annual probability of 1.3 in any given year, and in the future, they are expected to occur with a probability of 3.3 in each year. Evidently, changes in storm climatology and SLR are leading to a significant increase in the risk of compound flooding in the selected

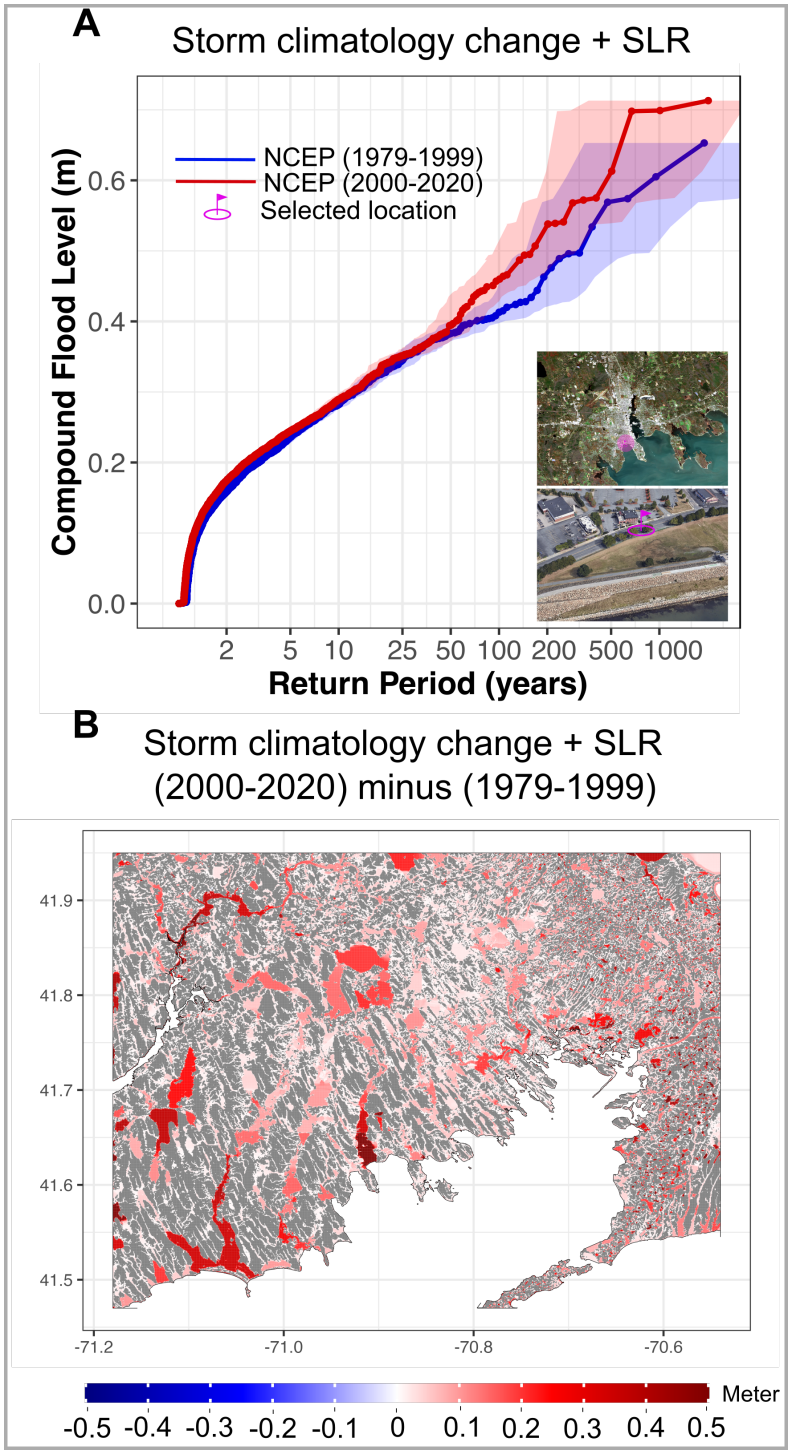

Figure 6: Impact of TC climatology change and SLR on the alteration of compound flooding risk during today's climate (2000-2020) in comparison to the late 20th century (1979-1999) in a selected coastal location. (A) representation of the compound flooding levels as a function of return period, comparing today's climate with the late 20th century. The results are derived from the depicted coastal location, excluding intertidal zones. Each line represents compound flooding outcomes produced through the generation of synthetic TCs based on reanalysis NCEP data for the respective time periods. The shaded areas in the figure indicate the sampling uncertainty margins, calculated using the 5th and 95th percentiles of a Poisson distribution. (B) Assessment of the impact of changes in TC climatology and SLR on the spatially-varying risk of 100-year return period compound flooding events in today's climate relative to the late 20th century. In this map, red color denotes an increasing trend, blue color represents a decreasing trend, and gray color signifies areas exhibiting no discernible trend or values close to zero.

area. Furthermore, in a future climate, the depth of compound flooding associated with low-frequency events from TCs will also substantially increase. For instance, for events with an annual probability of 0.2%, the depth of compound flooding in this specific area is projected to rise from approximately 0.5 meters in the current climate to 1.25 meters by the end of 21st century. Therefore, it is important that the design of infrastructure, housing, and other critical facilities takes into account the heightened risk of compound flooding from TCs, both in the present and in the face of future, intensifying storms and SLR.

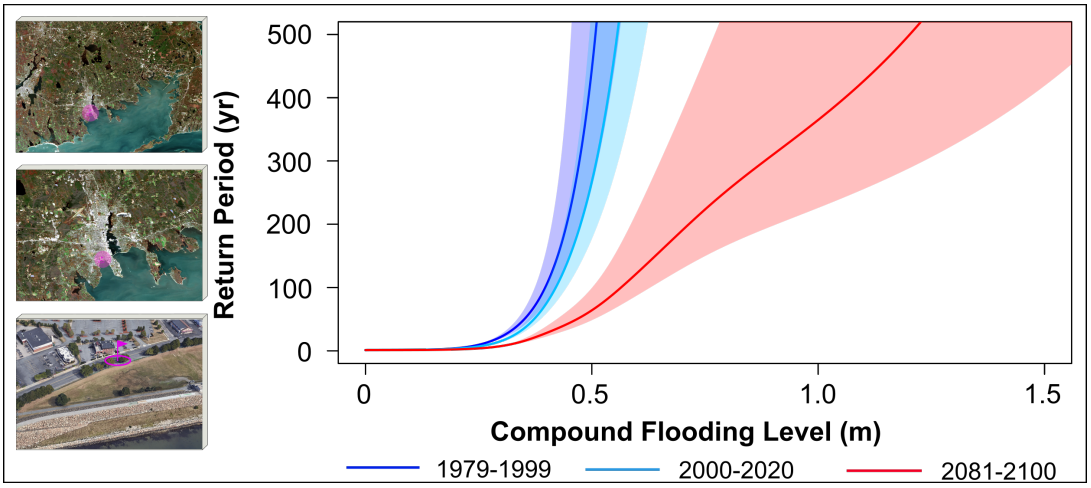

Figure 7: Impact of TC climatology changes and SLR on compound flooding in historical, present, and future climates in the selected coastal area (depicted in the left panels). Each line represents the outcomes derived from synthetic TCs downscaled from multiple climate models and reanalysis data for the three timeframes: historical (dark blue), present (light blue), and future climates (red). The shading in the figure represents confidence intervals (5% and 95%) derived through a bootstrapping approach for the ensemble of climate models. See text for details.

To gain a comprehensive understanding of the spatially distributed risk of compound flooding in the area, we have calculated the risk for each grid cell with a 20-meter spatial resolution, drawing from the extensive simulations of synthetic TCs. Figure 8 illustrates the results for different types of compound flooding events with return periods of 5, 50, 200, and 500 years. This spatial analysis provides valuable insights into the hazard frequency associated with both high-frequency and low-frequency compound flooding events from TCs. For each time period, including the late 20th century (Figure 8 A-D) and the 21st century (Figure 8 E-H), we assessed the depth of compound flooding for various high and low-frequency events at the grid cell level. To understand the role of changes in storm climatology and SLR in reshaping the risk landscape of compound flooding in a warming climate in the study area, we have used the late 20th century as a baseline for comparison. The ensemble mean of compound flooding for each return period was analyzed to discern trends and shifts in the occurrence and intensity of compound flooding from TCs. Figure 8 (I-L) reveals that, for high-frequency events, the level of compound flooding resulting from intensified TCs and SLR will increase by 0.5-1.0 meters in coastal areas and by 2.0-2.5 meters for low-frequency events in the same regions. In inland areas, the risk of flooding from intensified rainfall associated with TCs in a warming climate will increase significantly, with flooding levels rising by 1.5-2.5 meters for low-

frequency intensified TCs in the majority of areas.

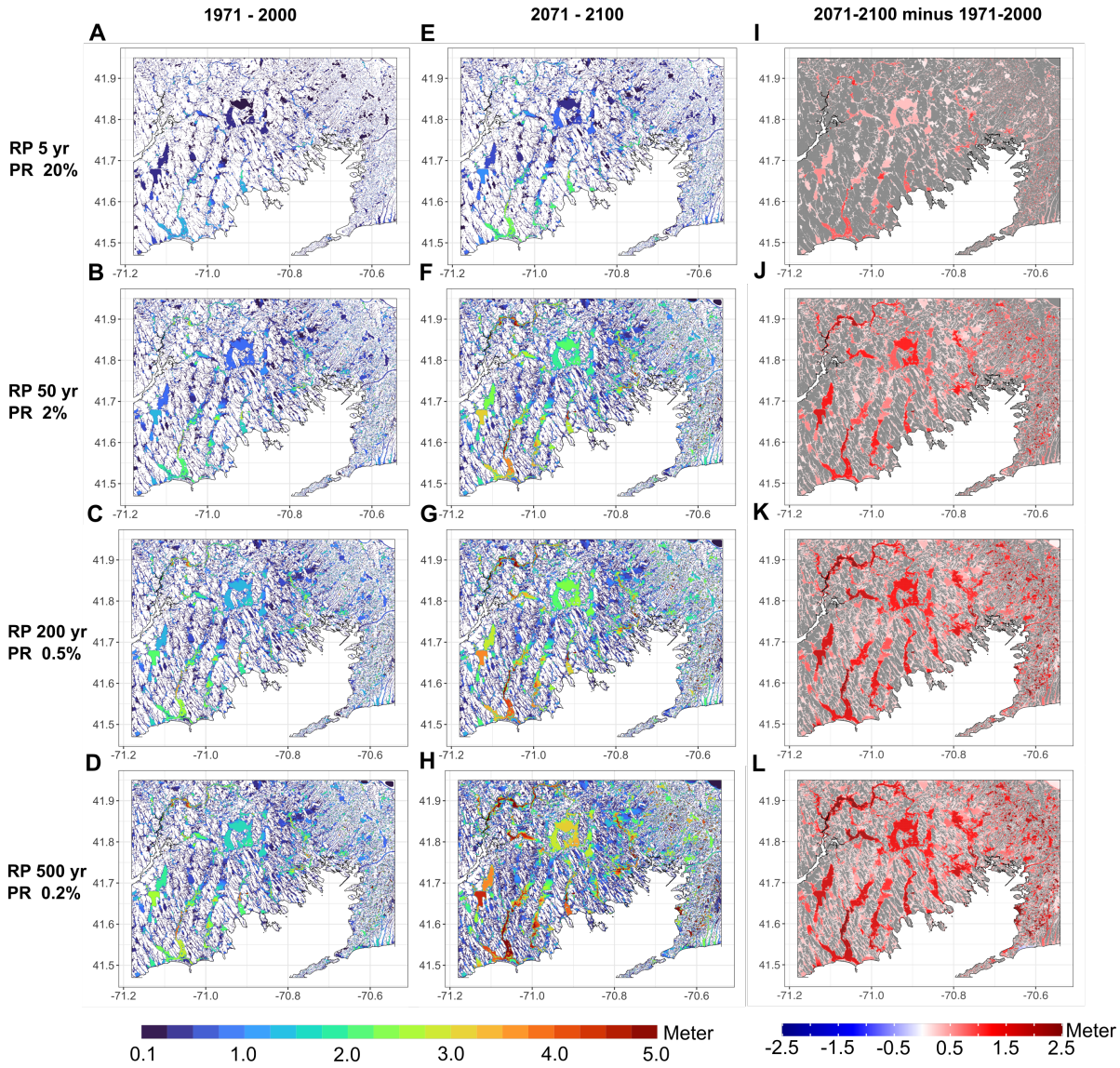

Figure 8: Spatially distributed granular risk of compound flooding from TCs in past and future climates. (A-D) Present the results of compound flooding for various return periods in the late 20th century. (E-H) Depict the same analysis for the late 21st century. (I-L) Illustrate the differences in compound flooding levels between the late 21st century and late 20th century for different return periods. Here, red indicates an increasing trend, blue indicates a decreasing trend, and gray signifies no clear trend or values close to zero. Note that these results are based on the ensemble mean of the six CMIP6 climate models.

The detailed, granular information provided in this section regarding compound flooding in the late 20th century and in a warming climate in the late 21st century is crucial for tailoring effective adaptation strategies in infrastructure design, as well as for the construction of buildings and critical infrastructure such as power plants. This information is also important for formulating policies and structuring insurance to discourage habitation in high-risk locations. Relying solely on historical risk assessments, even when extensive information is available, as depicted in Figure 8 (A-D), is insufficient. This is because the risk of compound flooding driven by TCs in future warming decades will surpass historical

risk due to changes in storm climatology and SLR (Figure 8 (E-H)). Our physics-based risk assessment methodology provides a comprehensive understanding of the compound flooding risk linked to TCs, spanning historical, current, and future scenarios. Through the comparative analysis of return periods across different temporal frames, our findings serve to inform and direct strategies for mitigating and adapting to the complex challenges presented by compound flooding in a continually evolving climate. Therefore, it is desirable to ground design decisions in physics-based risk assessment outcomes tailored to the future climate to establish resilience in infrastructure, urban development, and community preparedness.

3.6 Assessing compound flooding effect and risk from extratropical cyclones

In this section, similar to our approach with TCs, we conduct an analysis of compound flooding, highlighting the importance of the dynamics of compound flooding in the hazard analysis compared to other methods, such as assessing singular hazards, surge, and rainfall-driven flooding separately, or using a linear additive hazards approach—and how that might result in underestimating or overestimating the risk. To better understand the impact and importance of the complex dynamic of compound flooding in risk assessment in both the current and the later 21st century climates from ETC events, we selected a specific coastal area, which is also an urban area, as depicted in Figure 9 (A). This area was chosen to predominantly consist of non-tidal ground areas, with intertidal zones excluded, facilitating a comparative risk analysis.

We emphasize that our ETC risk analysis is very limited compared to our analysis of TC risk, owing to the great computational expense of downscaling ETCs, as discussed in section 2.2. We are here limited to using a single climate model run over limited spans of time and so considering only high frequency events, constrained as we are by the use of a previously generated ETC direct downscaling. We include this more limited risk analysis primarily to demonstrate that we can apply and learn from the same approach to compound flooding that we applied to TCs and in the hopes that we someday will do a more thorough analysis of ETC compound flood risk once suitable high-resolution data sets become available.

Figure 9 (B) illustrates that in the current climate, a substantial portion of the contributions to compound flooding in high-frequency events stems from rainfall-driven, rather than surge-driven, flooding. This highlights the potential for underestimating risks when solely considering surge-driven flooding in this region. Note that the lower values for surge-driven flooding are associated with the selected area that intentionally extends inland, specifically to exclude any intertidal zones. Conversely, the simplistic linear addition of these two individual hazards—without considering the complex hydrodynamics of their interaction during landfall—leads to an overestimation of risk for high-frequency ETC events (with a return period of 20 years or less). Looking ahead to the end of the 21st century, there is a notable increase in both individual and compound flooding risks, driven by changes in storm climatology and SLR. While risks from both rainfall-driven and surge-driven flooding show significant increases compared to the current climate, surge-driven flooding becomes more dominant and contributes more substantially to compound flooding than rainfall-driven flooding in this area for high-frequency ETC events. Ad-

ditionally, it is important to note that the mere linear combination of these two single hazards to assess compound flooding leads to biases and overestimates of the risk in the future climate scenario.

The results emphasize the need to account for the complex hydrodynamic interactions between individual flooding hazards for each event when evaluating the risk. Neglecting these dynamics, as seen in the previous studies Lin et al. [2019], Roberts et al. [2017] can result in an underestimation of the actual risk in both current and future climates. This discrepancy is likely to become more pronounced with changes in ETC climatology and SLR as depicted in Figure 9 (C).

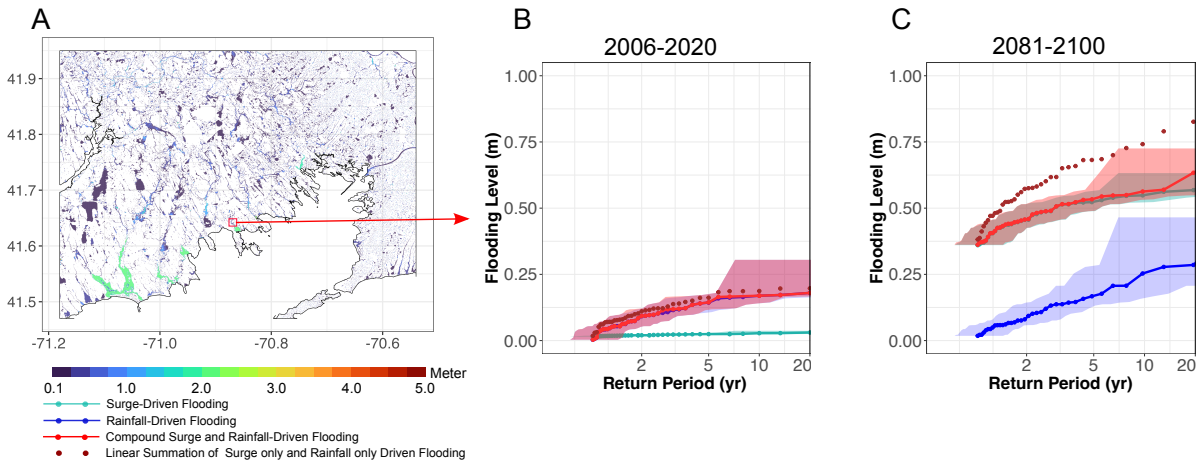

Figure 9: Comparison of ETC compound flooding risk assessment relative to individual surge and rainfall-driven flooding, and linear addition of individual hazards. (A) Maximum compound flooding level from a randomly selected dynamically downscaled ETC during current climate, along with the location of a coastal area chosen for comparing different types of flooding. (B) Flooding levels as a function of the return period from various individual and compound flooding hazard sources for the selected coastal area, in the current climate (2006-2020). (C) Similar to (B) but for the late 21st century (2081-2100). The shaded areas in the plots represent sampling uncertainty bounds, calculated based on the 5th and 95th percentiles of a Poisson distribution.

3.7 Sea level rise and extratropical cyclone climatology impacts

Here, we assess the impacts of individual and combined primary drivers—SLR and changes in ETC climatology—on the risk of compound flooding from high-frequency ETC events in both current and late-century climates. Figure 10 illustrates the levels of compound flooding in a previously selected coastal area (depicted in Figure 9-A), highlighting the effects due to changes in climatology (represented in orange) and the combined effects of climatology changes and SLR (represented in red) under two different climates.

In the current climate, SLR has a negligible impact on the risk of compound flooding from ETCs (Figure 10-A). However, by the end of the century, while changes in climatology may slightly increase the risk of compound flooding for events with a return period of 20 years or less, these changes are not significant when compared to the current climate (Figure 10-B). Conversely, the combined impact of ETC climatology changes and SLR

is projected to significantly alter the risk of compound flooding compared to the current climate, with the majority of changes attributable to SLR rather than to alterations in storm climatology. For instance, for ETC compound flooding events occurring once every 20 years, the level of compound flooding is approximately 0.35 m when considering only climatology changes; however, this level rises to about 0.63 m when SLR is also factored in. Therefore, compared to the current climate, the results suggest that SLR is likely to be the dominant factor increasing the risk of compound flooding, particularly for high-frequency ETC events in coastal areas in the coming decades. Once again, the limitations of the downscaled data set we used prevent us from a robust assessment of low frequency ETC events.

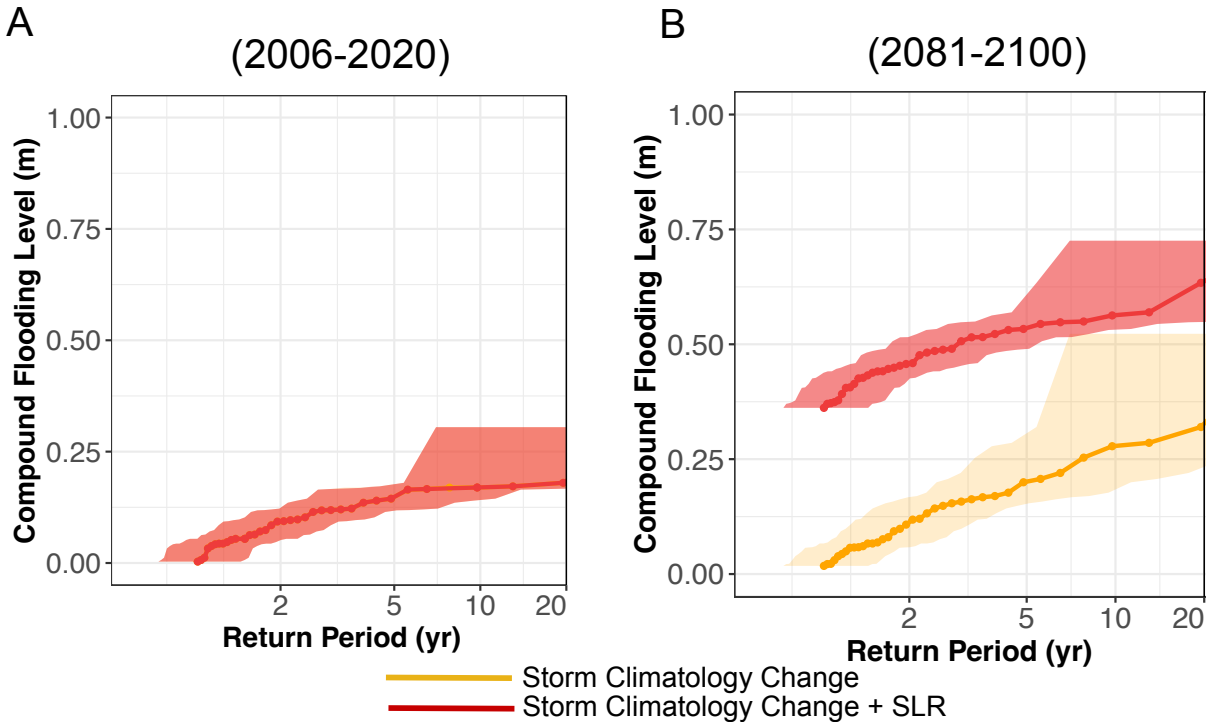

Figure 10: Assessing the contributions of SLR and ETC climatology changes to the risk of compound flooding in the current climate and the late 21st century, focusing on the location shown in Figure 9A. Each line in the graph represents simulated compound flooding levels from dynamically downscaled ETCs. The shaded region, representing the confidence interval that indicates sampling uncertainty, is calculated based on the 5th and 95th percentiles of a Poisson distribution.

3.8 Extratropical cyclone compound flooding risk in current and future climates

In Figure 11, we illustrate the contributions of ETC climatology changes and SLR to variations in the risk of compound flooding within the depicted area, encompassing both current and anticipated future warming climates. Our analysis is limited to high-frequency events, defined by return periods of 20 years or less, due to constraints associated with our downscaled dataset. The combined impact of ETC climatology changes and SLR is projected to lead to a nearly threefold increase in the likelihood of compound flooding by the end of the century in the selected coastal area. Specifically, compound flooding events with high-frequency occurrences, with a 5% annual probability, are expected to

occur with a 14% annual likelihood by the end of the century. These pronounced changes are primarily observed in the coastal areas. Similar high-frequency events stemming from TCs, as depicted in Figure 7, are projected to occur with an 11% annual likelihood by the end of the century. While the scenarios differ (RCP8.5 versus SSP3-7.0), the probability of such compound flooding events arising from ETCs is slightly, yet not significantly, higher under RCP8.5 (considered a high-end warming scenario). While it appears that the risk of high-frequency compound flooding will increase comparably for both TCs and ETCs, a consistent warming scenario is essential for a comprehensive comparison not only of high-frequency but also low-frequency compound flooding events from TCs and ETCs in the future climate.

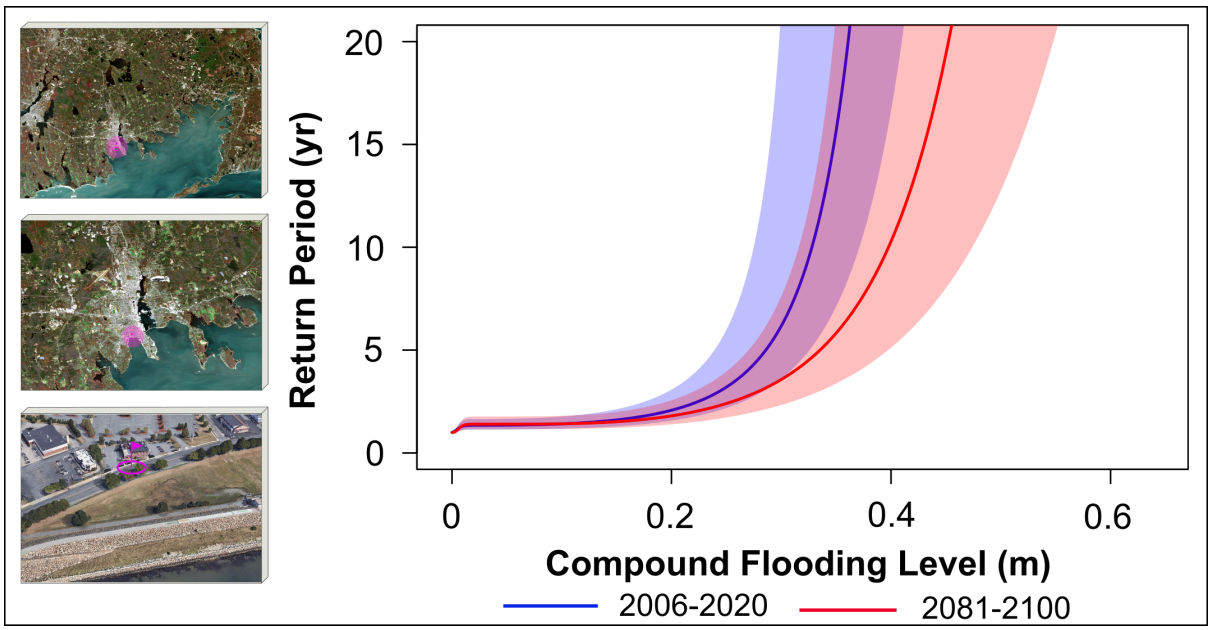

Figure 11: Impact of ETC climatology changes and SLR on the risk of compound flooding in the current and future climates in the selected coastal area (depicted in the left panels). Each line represents the outcomes derived from dynamically downscaled ETC events for two timeframes: the current climate (2006-2020, shown in blue) and future climates (2081-2100, shown in red). The shading in the figure represents confidence intervals (5% and 95%) derived through a bootstrapping approach.

To gain deeper insights into the effects of ETC climatology change and SLR, we also quantify the spatially varying risk of compound flooding events in the current and future warming climate. Figures 12 (A-D) depict the results for the current climate, while Figures 12 (E-H) display the projections for the end of the century. In Figures 12 (I-L), we highlight differences in flooding levels across different regions for the specified return periods. Evidently, coastal areas exhibit a pronounced intensification of compound flooding, attributed primarily to SLR within these regions. The magnitude of this intensification in compound flooding levels increases from events with return periods of 2 years to those with return periods of 20 years. However, unlike TC-driven compound flooding, the levels of flooding resulting from ETC events in inland areas display a distinct pattern for high-frequency ETC events. Our findings indicate no discernible trend in terms of flooding levels in inland areas at the end of the 21st century, relative to the current climate. In fact, some areas even exhibit a decreasing trend, with only some low-lying regions displaying an increasing trend, which is not statistically significant when compared to the current

climate. Therefore, our results suggest that rainfall-driven flooding from high-frequency ETC events will not intensify in inland areas from future ETC events relative to the ones in the current climate. The bulk of the intensification is expected to occur along coastal areas, driven primarily by SLR during high-frequency ETC events. These findings align with prior studies Lin et al. [2019], Booth et al. [2021], which indicate that the effects of climate change on ETC storms are relatively minor compared to the significant impact of SLR on storm surge intensification in northeastern U.S. coastal areas. To enhance our understanding and facilitate comparisons, it is imperative to include more dynamically downscaled ETC events over longer time periods, particularly focusing on low-frequency events. This would allow us to comprehensively assess the risk of compound flooding associated with these low-frequency ETC events, similar to the approach taken in our analysis of TC-driven compound flooding events.

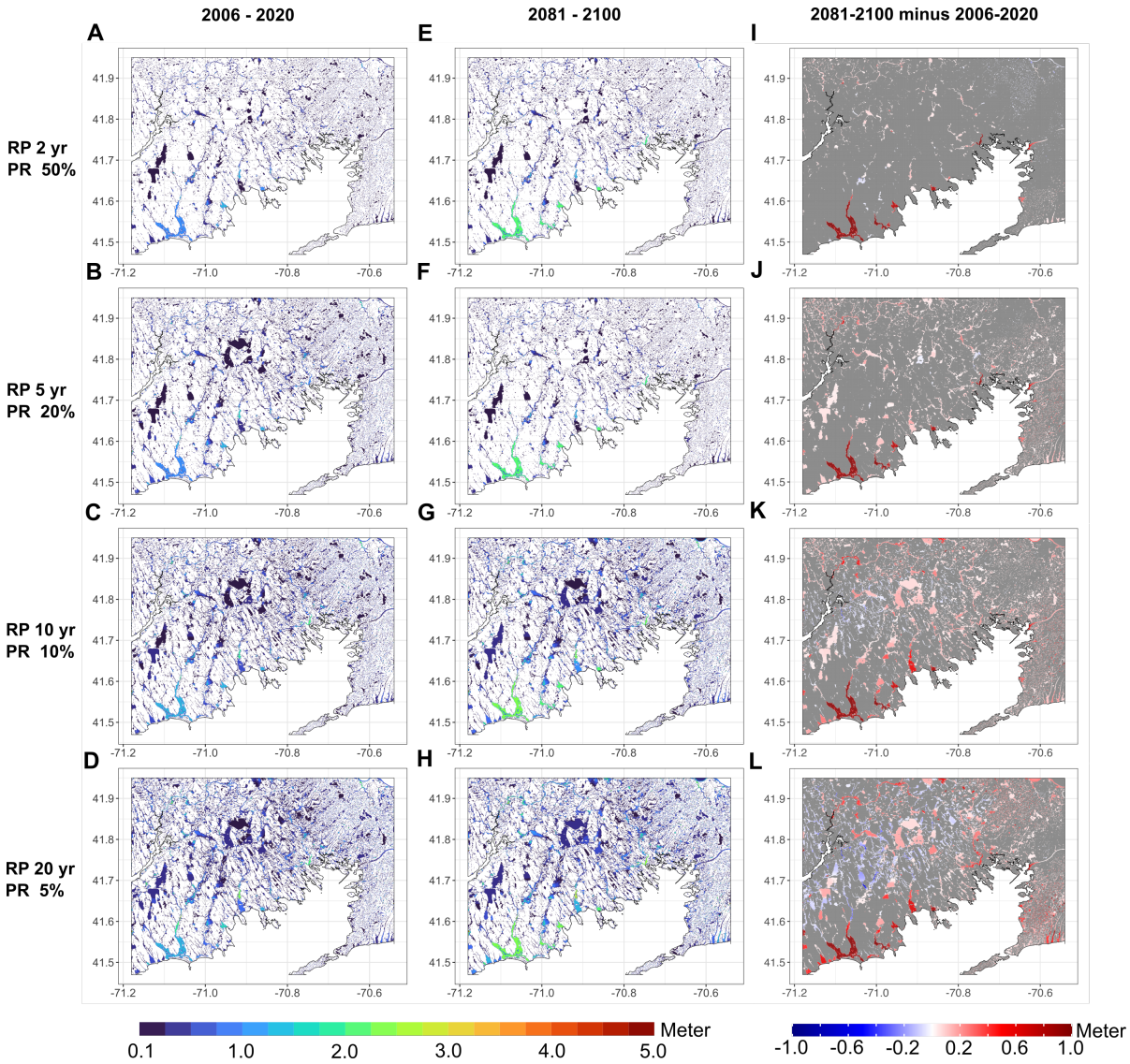

Figure 12: Spatially distributed granular risk of compound flooding from ETCs in the current and future climates. (A-D) Present the results of compound flooding for various return periods in the current climate. (E-H) Depict the same analysis for the late 21st century. (I-L) Illustrate the differences in compound flooding levels between the late 21st century and the current climate for various return periods. Note that red indicates an increasing trend, blue indicates a decreasing trend, and gray signifies no clear trend or values close to zero.

4 Conclusion

In this study, we employed a physics-based risk assessment methodology designed to quantify the frequency of compound flooding stemming from tropical and extratropical cyclones in coastal regions. We emphasize the virtues of a physics-based approach, which circumvents the severe limitations of historically based assessments, given the shortness of the records and the growing irrelevance of history in a changing climate. Such methods are essential for understanding the evolving landscape of compound flooding risk in coastal areas within the current and future climates. Our methodology offers a comprehensive means of assessing past, present, and future risks under the influence of changing storm

drivers and SLR, which amplifies coastal flooding.

To achieve our objectives, we employed a two-pronged approach. First, we downscaled from reanalyses and climate models comprehensive datasets of synthetic TCs using a statistical-deterministic method. Additionally, we assessed ETC compound flood risk using WRF-based downscaling of a single climate model, to demonstrate that our compound flood model can be applied to ETCs as well as to TCs. These simulations were informed by key climate statistics and reanalysis data, addressing the challenges associated with the scarcity of relevant datasets over varying time periods. Furthermore, this approach allowed us to account for the influence of climate change on the primary drivers of compound flooding. In order to quantify the hazard of compound flooding, our methodology explicitly considers the intricate hydrodynamics of this phenomenon. It takes into account the simultaneous interplay of surge-driven and rainfall-driven flooding across time and space during the landfall of each storm. This unique approach enables us to assess the contribution and magnitude of primary drivers, such as rainfall intensity, wind speed, and SLR, in amplifying compound flooding and backwater effects across both time and space at high resolution. It also facilitates the assessment of the contribution of each individual flooding type to the overall compound flooding risk assessment. Our results underscore the underestimation of both individual flooding hazards and the overall risk of compound flooding stemming from both TCs and ETCs, particularly in a warming climate. This underscores the significance of using numerical simulations that incorporate the complex hydrodynamics of explicit compound flooding caused by TCs and ETCs. This approach emphasizes the importance of moving away from reliance solely on statistical joint distribution of the drivers of compound flooding or conventional statistical or physical methods that focus exclusively on individual drivers or hazards Gori et al. [2022], Moftakhari et al. [2017], Lin et al. [2019, 2016], Garner et al. [2017], Reed et al. [2015].

Our methodology is essential for understanding the contribution of storm climatology changes and SLR to the evolution of compound flooding risk over time. We find that TC-driven compound flooding hazard is considerably higher than that of ETC-driven events, for high-frequency events in the Buzzards Bay area. The very limited ETC dataset available to us precludes such a comparison for low frequency events. Our results demonstrate an increased risk of TC-driven compound flooding in the present climate compared to the late 20th century, with significant intensification anticipated in warming climates. SLR emerges as a substantial contributor to this heightened risk. These results align with the findings of Gori et al. 2022 and Little et al. 2015, who demonstrated that SLR is the primary driver of increased risk of flooding from tropical cyclones in the northeastern U.S. for future scenarios. In the case of high-frequency ETC-driven compound flooding, we anticipate an amplified risk in coastal areas by the end of the century, primarily due to SLR. Although storm surge is only one component of compound flooding, Lin et al. 2019 demonstrated a slight increase in the risk of storm surge from high-frequency ETCs in the study area over the coming decades, based on projections using the CMIP5 RCP8.5 scenario. However, their analysis did not incorporate the significant impact of SLR, which our study shows is likely to further exacerbate this risk. Nevertheless, the risk in inland areas seems to remain relatively stable, with specific areas even experiencing a reduced risk of rainfall-driven flooding.

Our methodology for quantifying the risk of TC compound flooding is particularly effective, even for very low-frequency events, due to our ability to generate an almost unlimited number of synthetic cyclones. In contrast, our capacity to assess the risk associated with ETCs is significantly constrained by the limited number of events that can be simulated with complex, three-dimensional models such as WRF. This constraint is primarily due to the extensive computational resources required for such detailed simulations, which are necessary to accurately compare the risks of compound flooding from TCs and ETCs, especially for rare events. Future research should focus on developing more efficient techniques for downscaling ETCs. One promising approach involves running ensembles of high-resolution global climate models for both current and projected future climates. This strategy would allow researchers to derive ETC climatology directly from model outputs, providing a more comprehensive understanding of ETC behavior, especially for rare events under various climate scenarios. This approach facilitates a direct, like-for-like comparison of the risk of compound flooding from TCs and ETCs across various return periods. However, this method would require considerable computational power and data analysis capabilities, highlighting the need for substantial investment in high-performance computing resources. Though our study did not address the interaction of astronomical tides with storm surge and SLR, we acknowledge their importance and recommend their inclusion in future assessments of surge and compound flood hazards. Our methodology can be extended beyond the Buzzards Bay area and New York City Sarhadi et al. [2024] and can be applied as a scalable framework for vulnerable coastal regions worldwide that face the imminent threat of compound flooding from TCs and ETCs, even in the absence of historical records, regardless of their latitude. However, it is essential to tailor the methodology to incorporate region-specific factors, such as bathymetry, soil characteristics, coastal morphology, storm surge dynamics, and tidal influences. Customization helps ensure the accurate assessment and quantification of the compound flooding hazard by tailoring the approach to the specific characteristics and conditions of the region or scenario.

Our methodology also equips decision-makers with scientifically-informed insights to enhance preparedness and resilience of coastal areas. It enables authorities to estimate the likelihood of destructive storms in both current and future decades and quantify potential damages. Regional assessments empower authorities to customize adaptation strategies, allocate resources effectively, and safeguard critical infrastructure and coastal communities. Our study can serve as a cornerstone for proactive risk assessment, especially given the projected population increase within flood-prone coastal zones and megacities by 2050 Aerts et al. [2014], Neumann et al. [2015], Kulp and Strauss [2019]. Notably, despite the significant assets in coastal flood-prone areas, investments in protective measures often fall short. Our methodology provides a comprehensive guide to ensure that adaptation efforts are precisely tailored to address the unique challenges posed by compound flooding in coastal cities. In addition to localized adaptation measures, the need to reduce greenhouse gas emissions takes center stage in mitigating the increased risk and reducing associated damages within a warming climate.

In summary, our research significantly advances our ability to robustly assess the multifaceted risks associated with compound flooding, while concurrently providing decision-makers with a robust analytical framework and requisite resources to fortify the resilience of vulnerable coastal regions in response to the escalating influence of climate change.

Consequently, our study can serve as an essential foundation for the development and implementation of comprehensive strategies encompassing damage mitigation, strategic design, anticipatory planning, predictive forecasting, adaptive measures, and proactive mitigation interventions, all specifically tailored to address the complexities of coastal flooding caused by cyclonic storms.

The authors express their gratitude to Muge Komurcu, Matthew Huber, and Stanley Glidden for providing WRF dynamical downscaling data for ETC events. We also acknowledge the World Climate Research Programme, which, through its Working Group on Coupled Modelling, coordinated and promoted CMIP. We thank the leading research centers including the National Center for Atmospheric Research, the Centre National de Recherches Météorologiques, the EC-EARTH consortium, the Institut Pierre-Simon Laplace, the Atmosphere and Ocean Research Institute in collaboration with the National Institute for Environmental Studies and the Japan Agency for Marine-Earth Science and Technology, and the Met Office Hadley Centre. These institutions have contributed significantly by producing and making available their climate model outputs. Financial support for this work was provided by Homesite Insurance.

Data availability statement

For surge modeling, historical SLR data in the study area were obtained from NOAA (`https://www.tidesandcurrents.noaa.gov/sltrends/`). The CMIP6 SLR projections under the SSP3-7.0 scenario are also available at `https://sealevel.nasa.gov/ipcc-ar6-sea-level-p` `psmsl_id=12`. Additional data utilized in flood modeling, such as current bathymetry and coastal features, can be obtained from the following source, `https://www.ncei.noaa.gov/maps/bathymetry/`. The LiDAR-based Digital Elevation Model (DEM) with a computationally feasible spatial resolution of $\sim$ 20 m to represent the topography of the area is available at `https://coast.noaa.gov/dataviewer/`. The landuse map to quantify surface roughness is accessible at `https://www.mrlc.gov/`. A map showing soil available water storage, which is used to assess top-soil infiltration rates, can be found at `https://websoilsurvey.sc.egov.usda.gov/`. The NEXRAD radar-based rainfall intensity data for the study area is accessible from `https://www.ncdc.noaa.gov/nexradinv/chooseday.jsp?id=kbox`. The IBTrACS dataset for historical hurricanes in the Atlantic Basin is also available at `https://www.ncei.noaa.gov/data/international-best-track-archive-for-climate-stewardship-ibtracs/v04r00/access/csv/`. Sentinel-1 (SAR) images from Hurricane Michael can be accessed at `https://search.asf.alaska.edu/`. Synthetic TC tracks are based on the methodology described by Emanuel et al. 2006, and ETC event data are available from Komurcu et al. 2018.

Report 3

Hurricane Intensity Risk Assessment in a Warming Climate in the United States

1 Introduction

Hurricanes have profound and expansive impacts on human lives and the economy, inflicting an estimated annual economic toll of approximately $26 billion in the United States Bakkensen and Mendelsohn [2019]. Hurricanes present multiple hazards that can cause significant damage to both coastal and inland areas. These hazards include maximum sustained winds, freshwater flooding, and storm surge flooding driven by strong winds, which significantly affect vulnerable regions. Previous studies have indicated that tropical cyclone (TC)-related fatalities in the United States were primarily caused by coastal storm surges (49%), followed by flooding from torrential rains (27%), while wind-related fatalities accounted for 8% of the total mortality Rappaport [2014]. Among these hazards, insurance companies predominantly cover damages caused by wind, which occur in both coastal and inland areas.

Observed data indicate that property damage from wind storms escalates sharply with wind speed. Research linking wind intensity to destruction demonstrates a significant power-law relationship between damage and wind speed, as noted by Pielke (2007) Pielke Jr [2007]. For instance, Nordhaus (2010) Nordhaus [2010] found that in the United States, wind-related damage can increase exponentially, approximating the ninth power of wind speed. In practice, the construction standards in the United States and other vulnerable countries do not account for the rare but extreme wind speeds associated with major hurricanes. In recent decades, however, global warming has augmented the energy available for hurricane intensification, enhancing latent and sensible heat fluxes from the warming ocean and atmosphere Wehner and Kossin [2024]. This has led to an increased trend in the frequency of major hurricanes, accompanied by greater associated damages Meiler et al. [2022], Emanuel [2005], Meiler et al. [2022]. Therefore, it is of importance to understand how climate change is altering the risk associated with the maximum sustained wind speed of hurricanes in past, current, and future decades on local scale.

To improve the accuracy of projecting the impacts of global warming on tropical storm dynamics, especially in quantifying the risk of severe wind events, it is essential to overcome the limitations of current climate model simulations. These models frequently fail to resolve the crucial eyewall region of cyclones accurately, due to insufficient horizontal resolution, leading to the underestimation of maximum wind speeds—often significantly lower than those observed in reality. In this study, we employ a physics-based (statistical-deterministic) tropical cyclone model to create synthetic hurricanes for both historical and future periods, drawing on reanalysis data and climate model simulations. This approach aims to more accurately quantify the impact of climate change on hurricane risk. The model generates a large number of high resolution synthetic TCs employing methods outlined by Emanuel (2006, 2008) Emanuel et al. [2006, 2008], providing a robust framework for assessing hurricane risks in a changing climate. The method initiates synthetic TCs by randomly seeding the entire Atlantic basin in space and time. The initial wind intensity of these seeds is calculated deterministically using a high-resolution, coupled ocean-atmosphere tropical cyclone model, which is driven by the thermodynamic state of the ocean and atmosphere. Storms that intensify to wind speeds exceeding 21 m/s (40 knots) are retained, and the maximum surface wind speed throughout the lifetime of each track is recorded. The generated synthetic hurricanes are analyzed for their maximum wind speeds at high spatial resolution (approximately 16 km) over the ocean and after

landfall. However, this study focuses on the impact of maximum wind speeds of different hurricane categories on land. After generating a large dataset of storms and corresponding maximum wind speeds over historical and future periods using the CERA-20C reanalysis dataset and CMIP6 climate model simulations, we develop an innovative spatio-temporal varying Bayesian risk assessment methodology. This methodology quantifies the risk of strong winds from different hurricane categories after landfall over each county in vulnerable states. By considering the spatial and temporal dependencies between wind speeds in surrounding locations and using Bayesian Markov Chain Monte Carlo (MCMC) sampling from magnitude of wind speed of storms in each year, we address the risk and its uncertainties using this time-dependent risk framework. This approach enables to quantify how the risk of strong winds with potential economic damages has changed and will change in a warming climate at the county level for each hurricane category. Identifying which counties have been and will be more susceptible to the risks of different hurricane categories allows for more accurate financial damage assessments for current and future decades. These estimations can assist authorities in the Homesite insurance company in adjusting premiums in response to the escalating damages from intensifying hurricanes in the coming years and decades.

2 Dataset and methodology

In this study, we estimate the climatology and evolution of hurricanes across past, present, and future climates in the Atlantic basin using a physics-based, statistical-deterministic downscaling approach Emanuel et al. [2006, 2008]. This methodology entails the random seeding of synthetic TCs throughout the Atlantic Ocean basin, taking into account both spatial location and time of occurrence. Wind intensity is deterministically estimated using the high-resolution Coupled Hurricane Intensity Prediction System (CHIPS), which comprises an axisymmetric vortex model and a one-dimensional ocean model. The thermodynamic state of the ocean and atmosphere—including monthly mean sea surface temperature, atmospheric temperature, humidity, and daily interpolated horizontal winds at 250 and 850 hPa—guides the development of these randomly initialized vortices in both spatial and temporal dimensions. TCs that do not intensify beyond wind speeds of 21 m/s (40 knots) are excluded. Utilizing this approach, we generated numerous synthetic hurricanes aligned with the CERA-20C reanalysis for the late 20th and early 21st centuries (1901-2010). We further downscaled a comprehensive set of synthetic tracks from six bias-corrected General Circulation Models (GCMs) of the Coupled Model Intercomparison Project Phase 6 (CMIP6) to depict the evolution of TCs in the upcoming decades (2015-2100) under the SSP3-7.0 scenario. For each dataset, we produced 100 synthetic events annually to create a time series that more accurately addresses the uncertainty and risk associated with strong winds of various categories at each location (grid cell) with a spatial resolution of 0.15° (16 km) across the entire basin. Subsequently, we focused the study on a smaller area to quantify risk more precisely for each location, specifically excluding the Atlantic Ocean to concentrate on the risk posed by winds on land after hurricanes make landfall. The defined study area spans longitudes -99.4 to -66 and latitudes 22.0 to 49.0, covering states vulnerable to various hurricane categories

2.1 Spatio-temporal models for hurricane wind speed

In the context of hurricane wind speed analysis, we introduce X_{st}, representing the wind speed at location s and time t. Then, we assume that,

$$X_{st} = \begin{cases} 0, & \text{with probability } p_{st}, \\ \text{LN}(\mu_{st}, \sigma^2_{st}), & \text{with probability } (1 - p_{st}), \end{cases}$$

where the choice of a Lognormal distribution ($\text{LN}(\mu_{st}, \sigma^2)$) for positive wind speeds is predicated on its ability to naturally encapsulate the skewed distribution of wind speed data. This assumption allows us to model wind speeds in a manner that aligns closely with their empirical distribution, particularly the Gaussian behavior of the log-transformed positive wind speeds.

Due to the complex interdependencies among wind speed data across neighboring locations over space and time, we employ Bayesian spatio-temporal models to quantify the parameters p_{st}, μ_{st}, and σ^2. The Integrated Nested Laplace Approximation (INLA) method is chosen as our computational foundation, favored for its efficiency and effectiveness as an alternative to the traditional Markov Chain Monte Carlo (MCMC) methods. This selection is supported by the work of Blangiardo et al. (2013)Blangiardo et al. [2013], which highlights INLA's suitability for high-dimensional spatio-temporal modeling.

Here, we develop and compare two distinct versions of linear and non-linear Bayesian spatio-temporal models to quantify the given parameters:

2.2 Linear model

Our first approach utilizes a linear Bayesian spatio-temporal framework, expressed as:

$$\text{logit}(p_{st}) = \alpha^{(p)} + v_s^{(p)} + \nu_s^{(p)} + (\beta^{(p)} + \delta_s^{(p)}) \cdot t + \epsilon_{st}^{(p)} \tag{6}$$

in accordance with the methodology proposed by Bernardinelli et al. (1995) Bernardinelli et al. [1995]. This formulation models the log-odds of parameter p_{st}, integrating both spatial and temporal dimensions. Here, $\alpha^{(p)}$ denotes the global intercept, capturing the baseline log-odds across all locations and times. The model incorporates both spatially structured ($v_s^{(p)}$) and unstructured ($\nu_s^{(p)}$) components to capture spatial autocorrelation and locale-specific effects, respectively. Temporal dynamics are represented through a global linear trend ($\beta^{(p)}$) and location-specific slopes ($\delta_s^{(p)}$), facilitating the examination of temporal patterns both universally and at individual locations. The error term, $\epsilon_{st}^{(p)}$, follows an independent and identically distributed Gaussian distribution with mean zero and variance σ_ϵ^2, representing unexplained variability.

For the spatially structured residuals, we employ the Besag-York-Mollie (BYM) model, renowned for its aptitude in modeling spatial dependency through an intrinsic conditional autoregressive (iCAR) structure:

For the spatially structured residuals, $v_s^{(p)}$, we employ the Besag-York-Mollie (BYM) model Besag et al. [1991], where $v_s^{(p)}$ are defined by an intrinsic conditional autoregressive (iCAR) structure:

$$v_s^{(p)}|v_{r\neq s}^{(p)} \sim N\left(\frac{1}{\#N(s)}\sum_{r\in N(s)} v_r^{(p)}, \frac{\sigma_v^2}{\#N(s)}\right) \tag{7}$$

where $\#N(s)$ denotes the number of neighbors of site s.

The spatially unstructured component, denoted by ($\nu_s^{(p)}$, is assumed to be iid, following a normal distribution, $\nu_s^{(p)} \sim N(0, \sigma^2)$. The term $\delta_s^{(p)}$ represents the difference between the global trend $\beta^{(p)}$ and the specific trend at s. If $\delta_s^{(p)} < 0$, then the trend at s is less steep than the global trend and vice versa. It is assumed a priori that $\delta_s \sim \text{Normal}(0, 1/\tau_\delta)$. Selected hyper-priors for the model parameters include an improper distribution for the global intercept ($\alpha^{(p)}$), reflecting a non-informative prior approach, allowing the data to primarily inform its estimation. This approach ensures flexibility in modeling while incorporating prior knowledge where applicable.

Similarly, we may assume a linear model for μ_{st} and σ_{st}^2 as follows:

$$\mu_{st} = \alpha^{(\mu)} + v_s^{(\mu)} + \nu_s^{(\mu)} + (\beta^{(\mu)} + \delta_s^{(\mu)}) \cdot t + \epsilon_{st}^{(\mu)} \tag{8}$$

and

$$\log(\sigma_{st}^2) = \alpha^{(\sigma)} + v_s^{(\sigma)} + \nu_s^{(\sigma)} + (\beta^{(\sigma)} + \delta_s^{(\sigma)}) \cdot t + \epsilon_{st}^{(\sigma)} \tag{9}$$

2.3 Non-linear model

Our second model moves beyond the linearity assumption for δ_s, adopting the approach proposed by Knorr-Held (2000) Knorr-Held [2000]. This model is expressed as:

$$\text{logit}(p_{st}) = \alpha^{(p)} + v_s^{(p)} + \nu_s^{(p)} + \gamma_t^{(p)} + \phi_t^{(p)} \tag{10}$$

where $\alpha^{(p)}$, $v_s^{(p)}$, and $\nu_s^{(p)}$ are defined in the same manner as in equation (1). The term $\gamma_t^{(p)}$ denotes the temporally structured effect, which is dynamically modeled (e.g., using a random walk) to reflect temporal dependencies through a neighboring structure:

$$\gamma_t|\gamma_{-t} \sim \text{Normal}(\gamma_{t+1}, \tau_\gamma), \text{ for } t = 1, \tag{11}$$

$$\gamma_t|\gamma_{-t} \sim \text{Normal}\left(\frac{\gamma_{t-1} + \gamma_{t+1}}{2}, \frac{\tau_\gamma}{2}\right), \text{ for } t = 2, \ldots, T-1, \tag{12}$$

$$\gamma_t|\gamma_{-t} \sim \text{Normal}(\gamma_{t-1}, \tau_\gamma), \text{ for } t = T. \tag{13}$$

Finally, ϕ_t is specified by means of a Gaussian exchangeable prior,

$$\phi_t \sim \text{Normal}(0, \tau_\phi). \tag{14}$$

After running both linear and nonlinear models, we select the best-fitted version based on the Deviance Information Criterion (DIC). Our analyses reveal that, in the majority of cases, the nonlinear model outperforms the linear model. Therefore, for risk assessment, we employ the nonlinear version of the model.

2.4 Risk analysis across hurricane categories

Here, our objective is to quantify the risk associated with surpassing specific wind speed thresholds that define different hurricane categories at each site s and time (year) t. Each hurricane category is characterized by a unique wind speed threshold, denoted as x_0. Utilizing the parameters p_{st}, μ_{st}, and σ^2_{st}, and referring to Equation (5), we express the probability of exceeding a given threshold x_0 as follows:

$$\Pr(X_{st} > x_0 \mid p_{st}, \mu_{st}, \sigma^2_{st}) = (1 - p_{st}) \left(1 - F_{LN}(x_0; \mu_{st}, \sigma^2_{st})\right) \tag{15}$$

where $F_{LN}(x; \mu, \sigma^2)$ represents the cumulative distribution function (CDF) of a lognormal distribution with parameters μ and σ^2. This formulation accounts for the probabilistic nature of wind speeds exceeding threshold x_0 under the lognormal assumption.

To estimate the posterior distribution of this exceedance probability, we employ a Monte Carlo approximation method, integrating over the posterior distributions of the model parameters:

$$\begin{aligned} \Pr(X_{st} > x_0 \mid \text{data}) = &\int \Pr(X_{st} > x_0 \mid p_{st}, \mu_{st}, \sigma^2_{st}) \\ &\times f(p_{st}, \mu_{st}, \sigma^2_{st} \mid \text{data})\, d(p_{st}, \mu_{st}, \sigma^2_{st}) \\ \approx &\frac{1}{M} \sum_{m=1}^{M} \Pr(X_{st} > x_0 \mid p^{(m)}_{st}, \mu^{(m)}_{st}, \sigma^{2\,(m)}_{st}) \end{aligned} \tag{16}$$

where $p^{(m)}_{st}$, $\mu^{(m)}_{st}$, and $\sigma^{2(m)}_{st}$, for $m = 1, \ldots, M$ represent the m-th posterior sample of the model parameters, obtained via the INLA technique. This approach enables us to derive a comprehensive statistical summary of the risk, including posterior means, standard deviations, credible intervals, and histograms for the return periods of exceeding specific wind speed thresholds across hurricane categories.

3 Results

3.1 Historical changes in hurricane wind risk

After calculating the exceedance probabilities for each grid cell using the reanalysis CERA-20C dataset, we aggregated the average exceedance probability over time for each county. This approach allows us to estimate, for any given year within the 1901-2010 reanalysis period, the likelihood that a county might experience a hurricane with a specific intensity for each category. Subsequently, we assessed the temporal trends in exceedance probability for each hurricane category at the county level by applying Sen's slope estimator, which facilitates the calculation of change rates over time (per decade) across the historical period.

Figures 1-5 illustrate the temporal changes in risk, highlighting how the probability of experiencing hurricanes of specific categories has evolved at the county level in recent decades. Notably, Figure 1 reveals an increasing decadal risk that counties, particularly those identified as vulnerable, will encounter at least a category 1 hurricane or above. Among these, counties in southern Florida exhibit the most pronounced increase in risk. Moreover, coastal counties along the Gulf Coast demonstrate a greater escalation in risk over time compared to their more inland counterparts. This trend persists across higher hurricane categories, especially those above category 3, which are considered the most destructive. These increases in the risk of severe hurricane wind speeds pose significant threats of economic damage to the Homesite Insurance portfolio, affecting both vulnerable coastal and inland counties.

To elucidate the temporal evolution of these probabilities, we also present a case study for Miami-Dade county, illustrating the escalating risk and rate of change across different hurricane categories within this county. Our analysis provides time-dependent probabilities for each county, serving as an important metric for calculating insurance premiums. These probabilities account for the varied risk levels associated with different hurricane categories, offering valuable insights for risk assessment and management strategies in vulnerable regions.

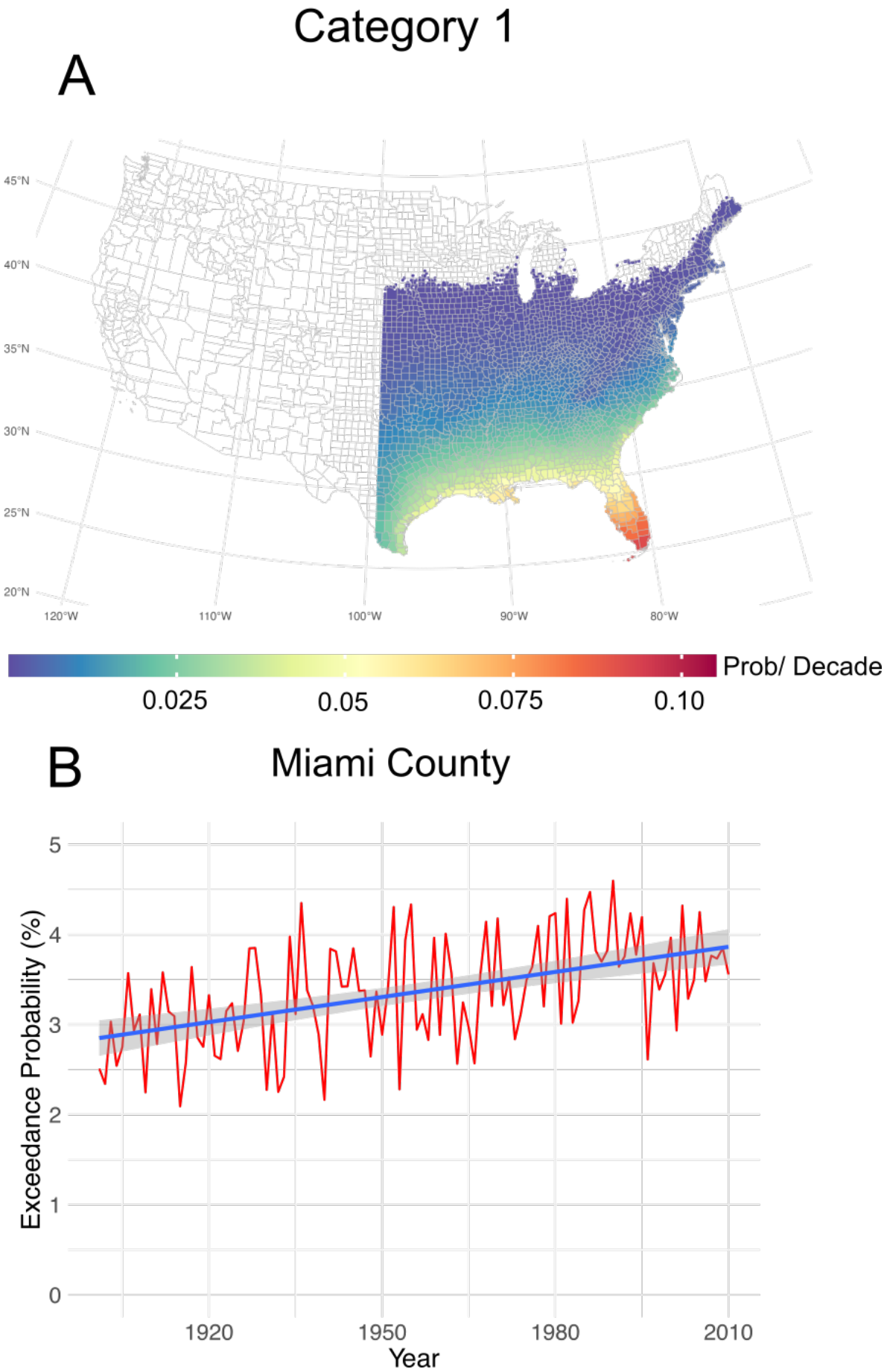

Figure 13: Changes in the probability of hurricanes of category 1 or higher from 1901 to 2011 using reanalysis CERA-20C data. A) Change rate in the probability of hurricanes with category 1 and higher at each location per decade (Note that locations with probability values less than 0.002 are removed). B) Exceedance probability of hurricanes of category 1 and higher in Miami County over time.

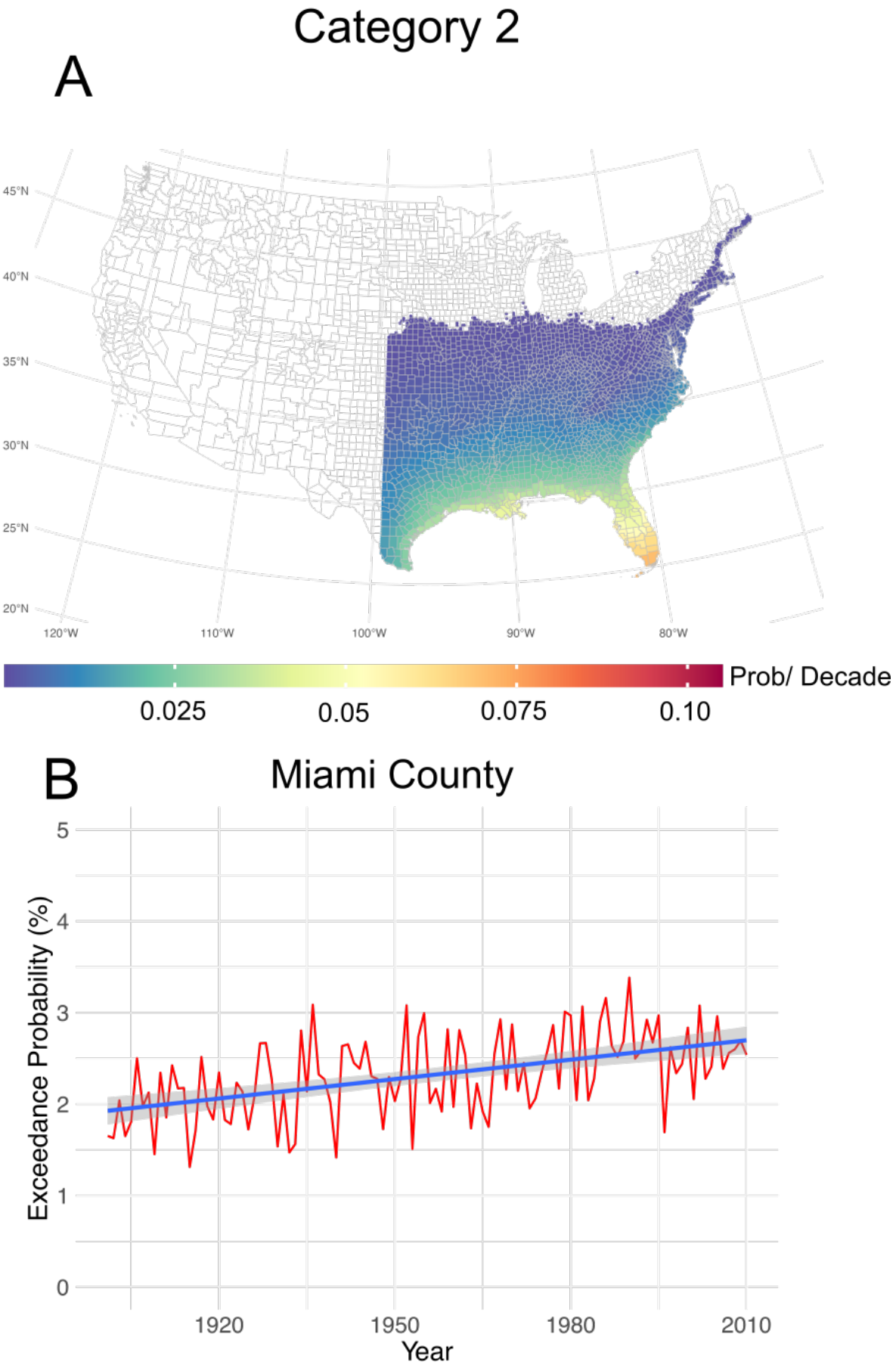

Figure 14: Similar to Figure 1, but for hurricanes of category 2 or higher

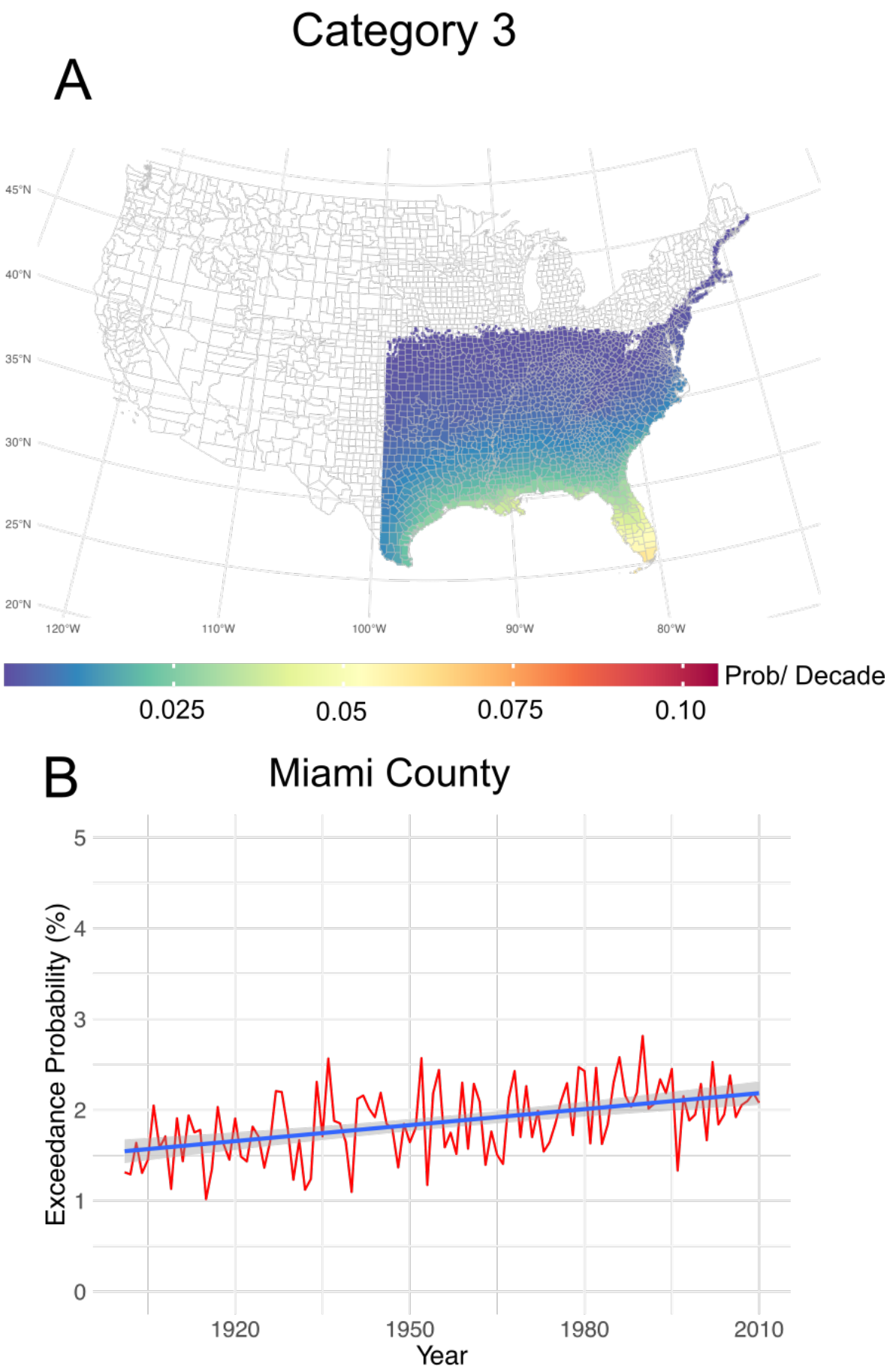

Figure 15: Similar to Figure 1, but for hurricanes of category 3 or higher

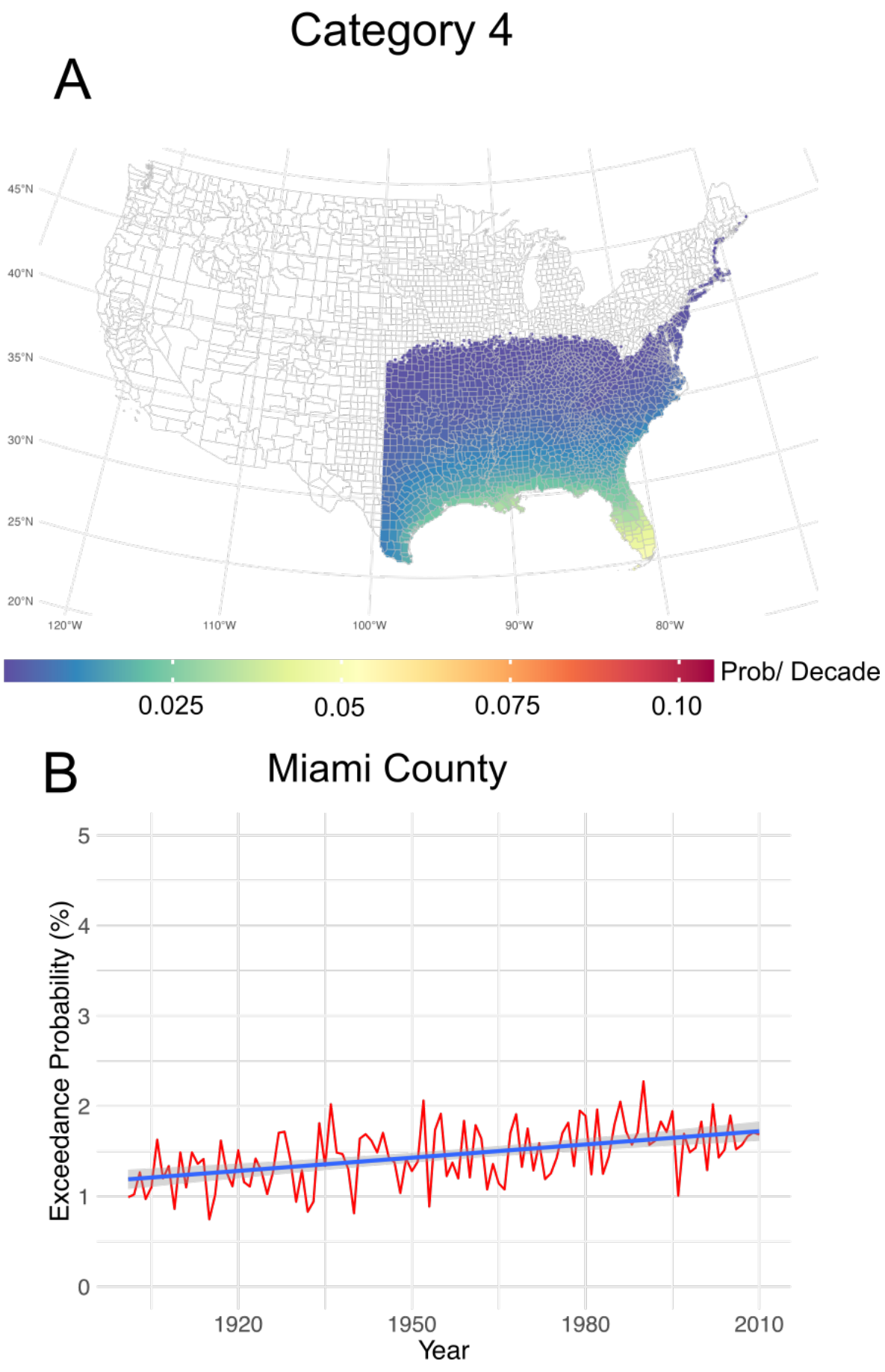

Figure 16: Similar to Figure 1, but for hurricanes of category 4 or higher

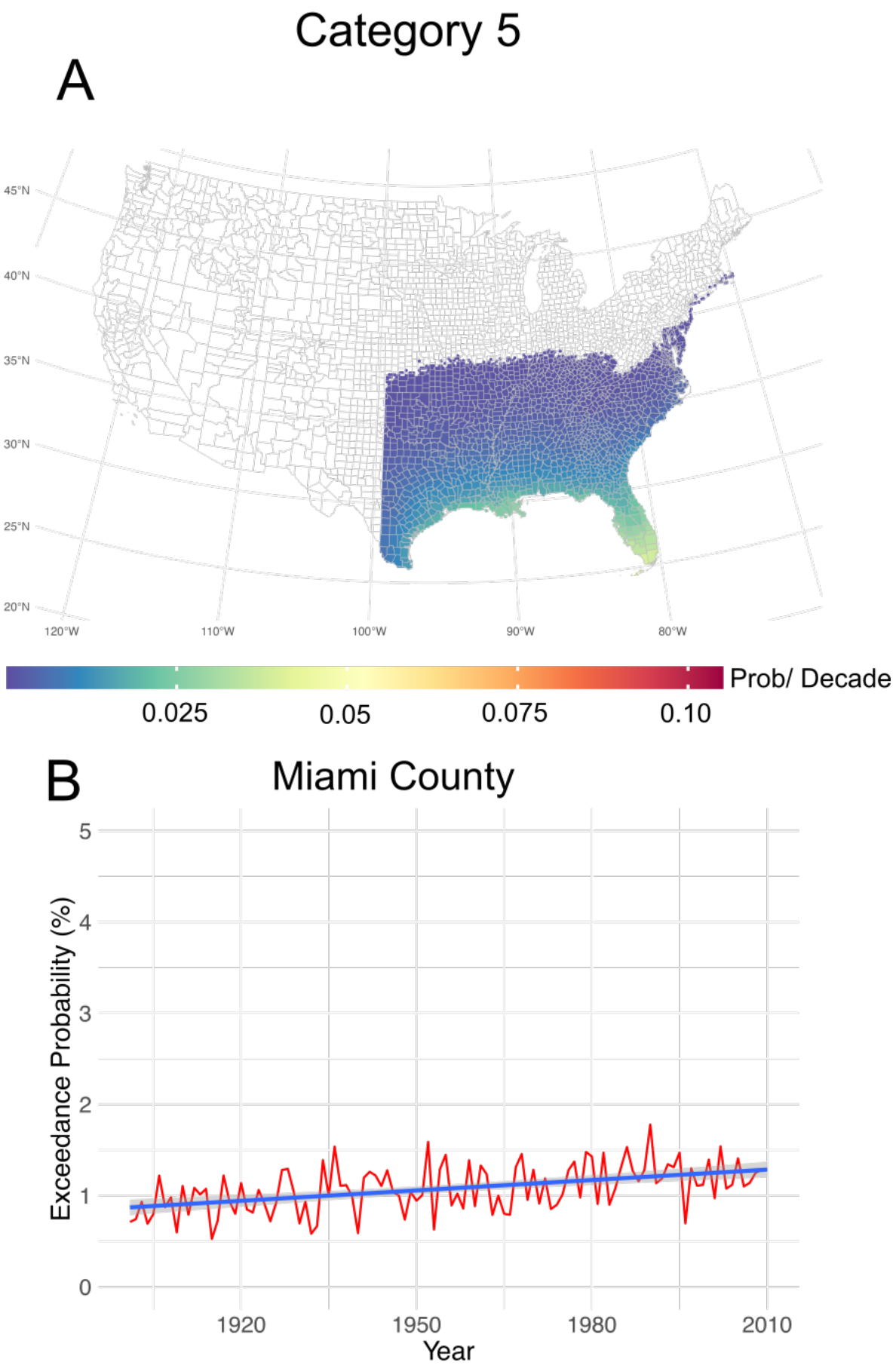

Figure 17: Similar to Figure 1, but for hurricanes of category 5 or higher

3.2 Historical changes in frequency of hurricanes

To assess the temporal evolution of hurricane frequency across different wind speed categories, we employed time-varying exceedance probabilities to calculate the changing return periods. This method allowes us to quantify alterations in the frequency of hurricanes surpassing specific wind speed thresholds. To illustrate these changes, we computed the average return periods for two distinct periods: the early 20th century (1901-1920) and the recent decades (1991-2010), utilizing the available reanalysis data. Figures 6-10 depict the variations in the return periods for different categories of hurricanes, emphasizing the frequency of events exceeding predetermined wind thresholds.

For instance, Figure 6(A-B) delineates the return periods for hurricanes of Category 1 and above during the selected intervals, with a breakdown by county. The analysis clearly indicates a discernible upward trend in the frequency of Category 1 or higher hurricanes over the decades. Moreover, there has been an increase not only in the frequency of such hurricanes in specific counties but also in the number of counties affected by hurricanes of Category 1 or higher. For example, for Category 1 hurricanes, there is a notable rise in the number of counties subjected to wind speeds of Category 1 or higher, with return periods once every 50-100 years, demonstrating a significant uptick in the current climatic conditions compared to the early 20th century. The same pattern exists with other high frequency (return period < 30 yr).

A detailed case study of Miami-Dade County, illustrated in Figure 6-C, exemplifies the significant increase in the occurrence of Category 1 and higher intensity hurricanes in recent decades. For instance, at the onset of the 20th century, this county experienced such hurricanes approximately once every 36 years, whereas, in recent decades, the frequency has escalated to once every 25 years by 2010. This specific analysis corroborates the broader evidence of increasing hurricane frequencies, underscoring the urgent need for improved preparedness and adaptive strategies to alleviate potential economic impacts.

Furthermore, to elucidate the temporal dynamics of hurricane frequencies for higher categories, we extended our analysis to include these intensities. Figures 6-10 show the results across various hurricane categories, revealing a consistent upward trend in both frequency and spatial extent along the coastal counties of the southern and eastern coasts. Notably, there has been a significant increase in the occurrence and geographic coverage of destructive hurricanes (category 3 and above), which have been associated with heightened economic damages in recent decades. This trend underscores the growing impact of such hurricanes on these regions, emphasizing the need for adaptation strategies to mitigate future economic losses.

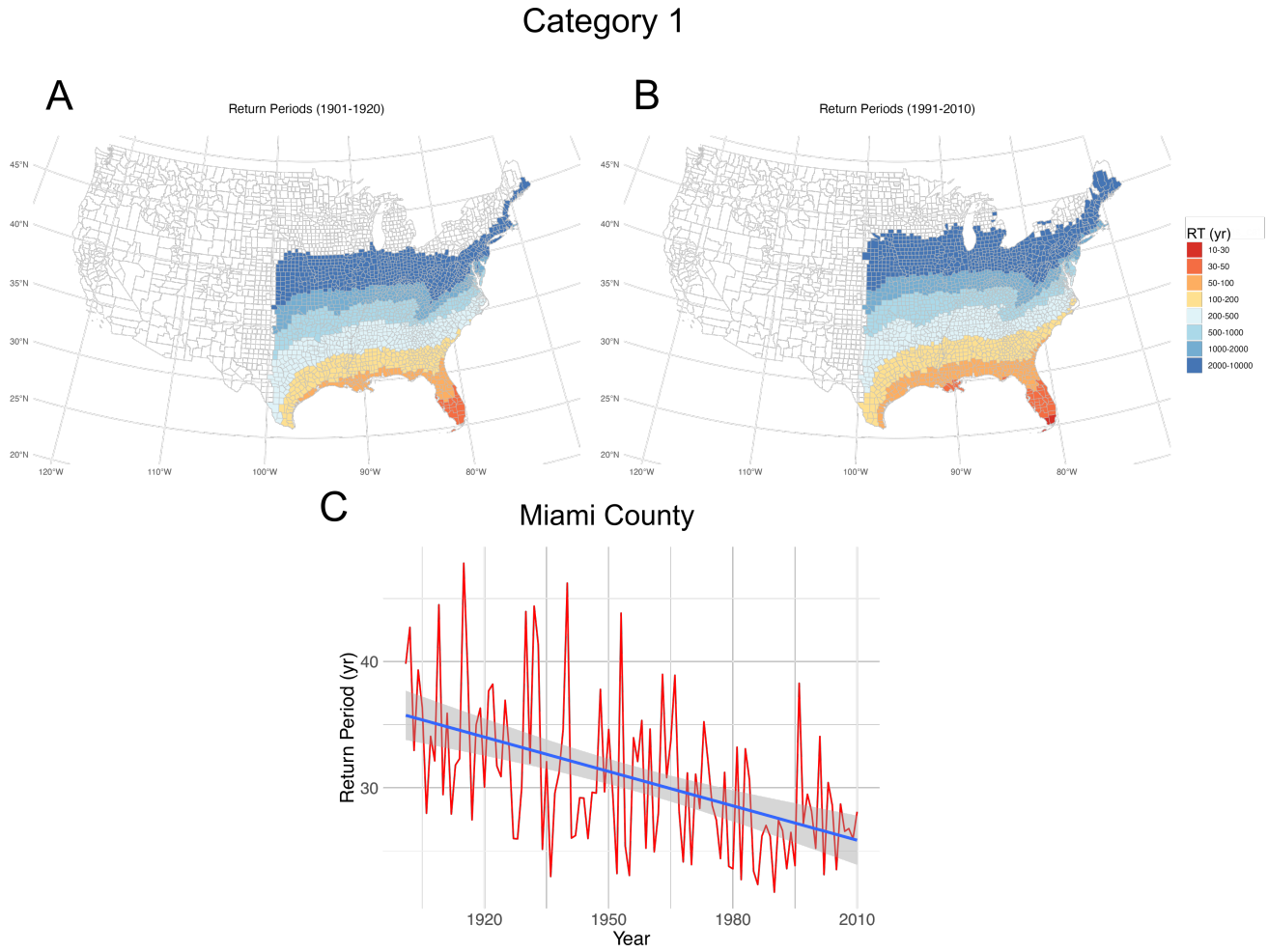

Figure 18: Return periods for hurricanes of category 1 or higher at the county level. A) Return periods for category 1 hurricanes and above in the early 20th century (1901-1920); B) Return periods for the same category of hurricanes in recent decades (1990-2010); C) Changes in the return periods for hurricanes of category 1 or higher in Miami County over time (1901-2010).

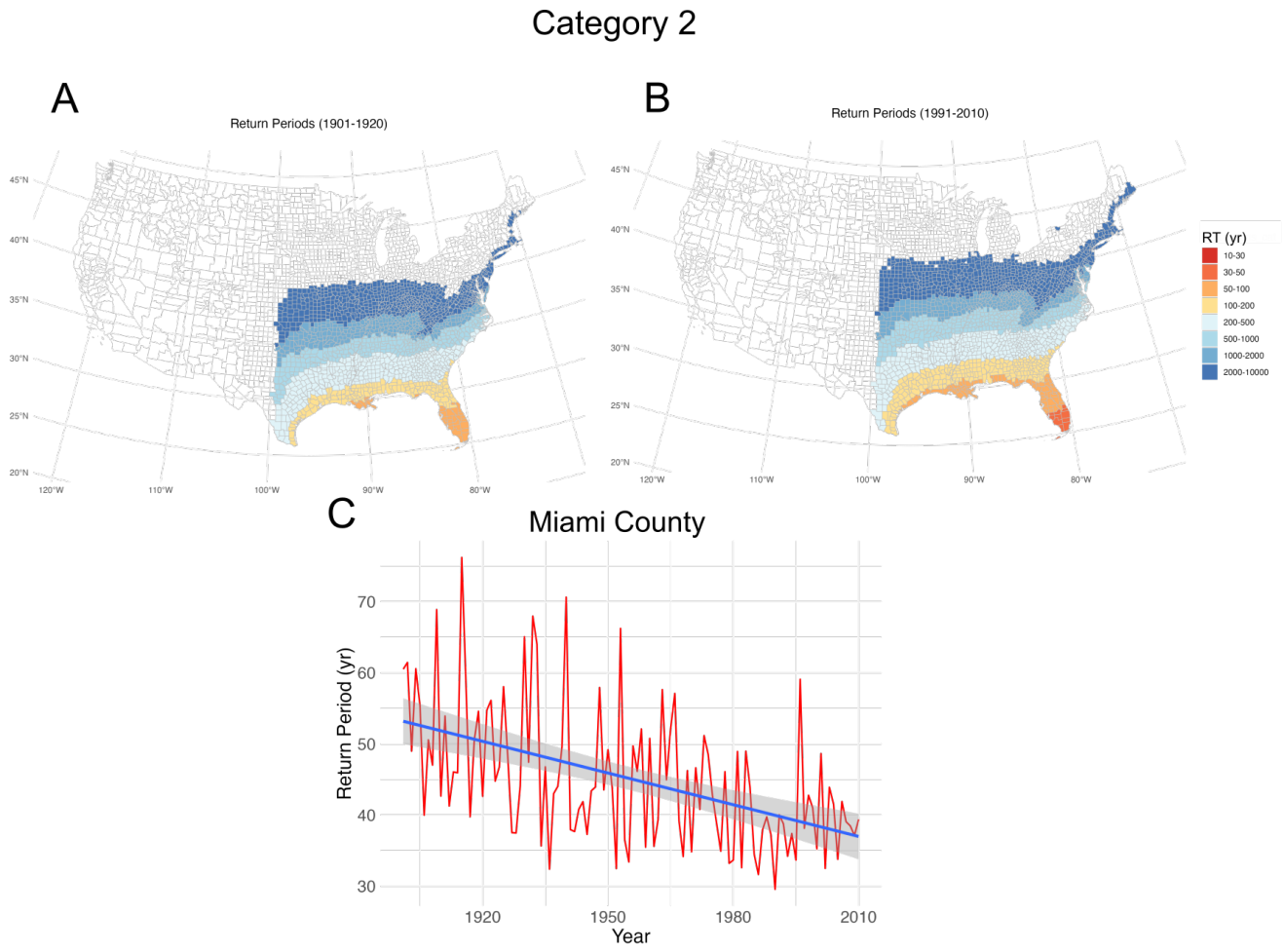

Figure 19: Similar to Figure 6, but for hurricanes of category 2 or higher

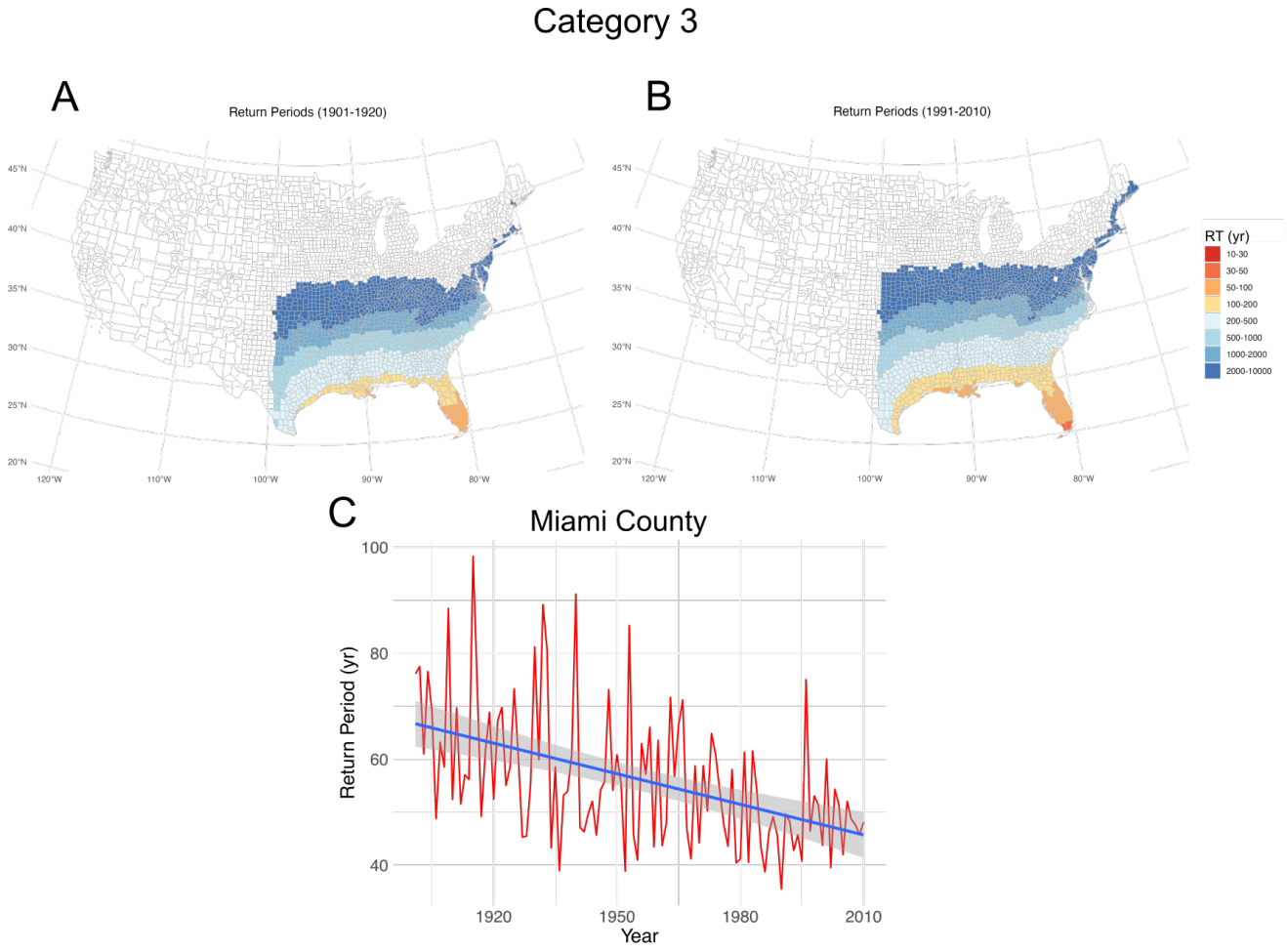

Figure 20: Similar to Figure 6, but for hurricanes of category 3 or higher

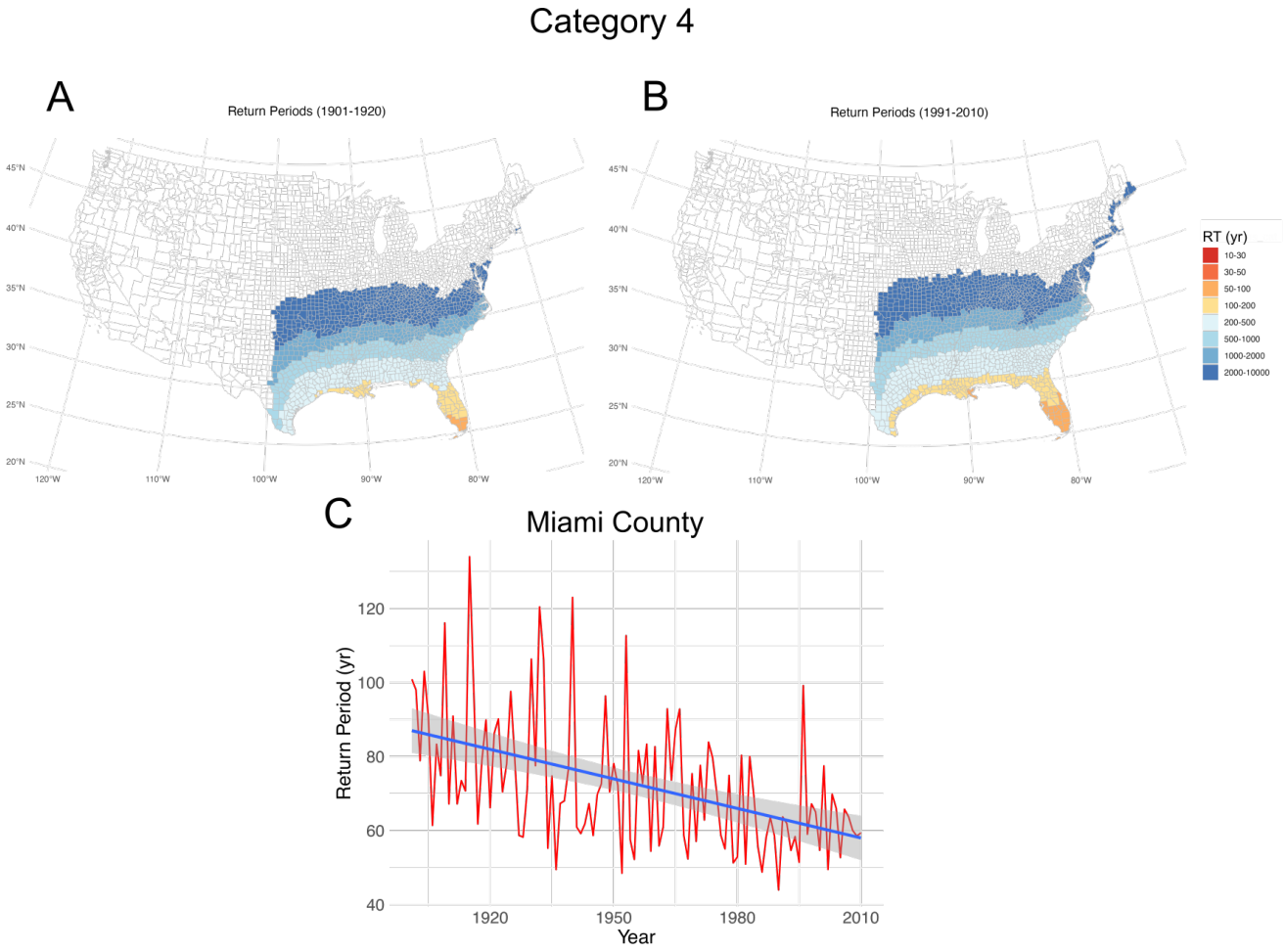

Figure 21: Similar to Figure 6, but for hurricanes of category 4 or higher

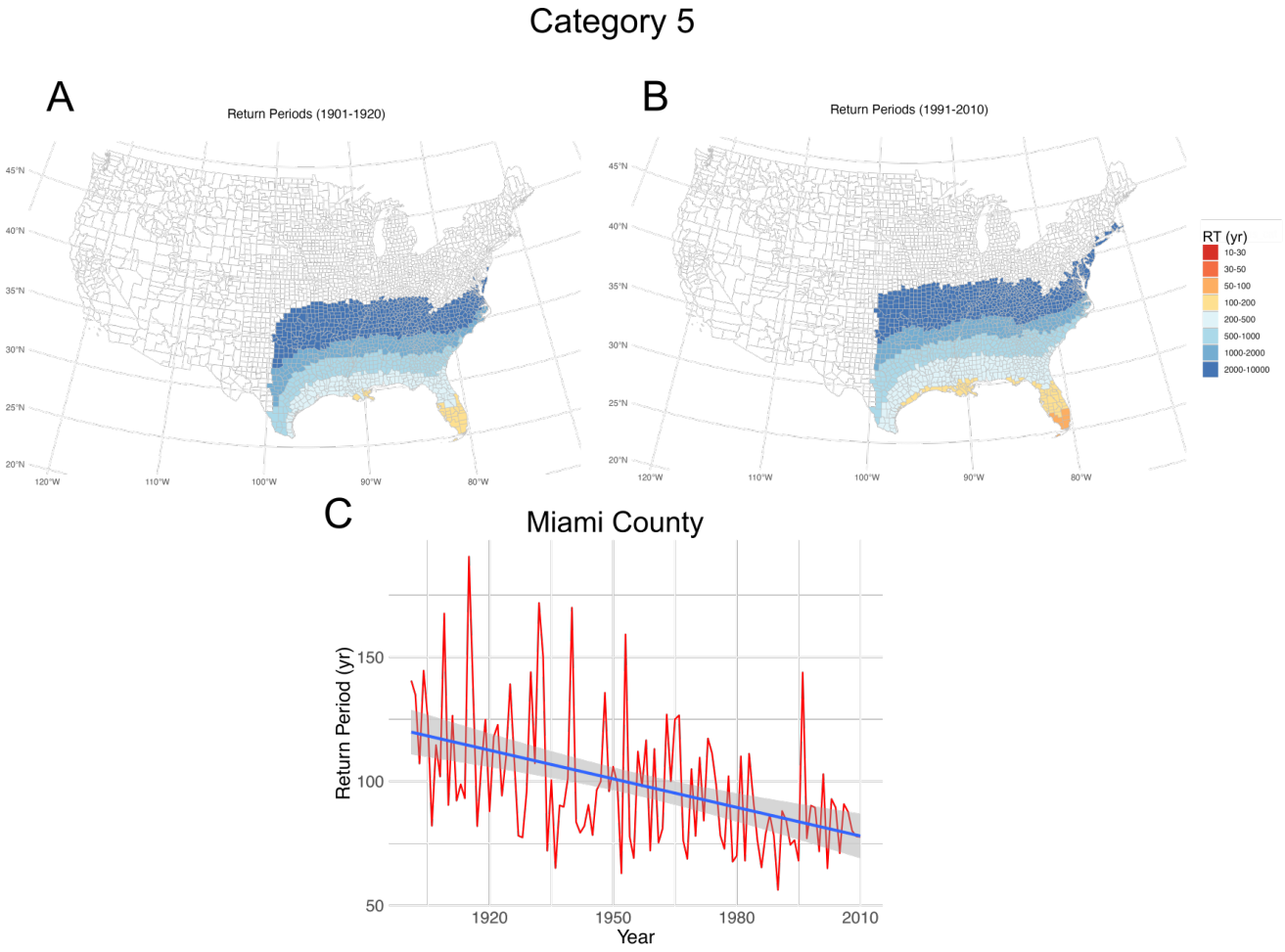

Figure 22: Similar to Figure 6, but for hurricanes of category 5 or higher

3.3 Future changes in risk of hurricanes

To assess the potential changes in the risk of strong winds from hurricanes of varying categories in the coming decades, we applied our methodology to simulated synthetic hurricane tracks derived from six CMIP6 climate models (CNRM, IPSL, MPI-M, ECEARTH, MIROC, and UKMO) under the SSP3-7.0 future scenario. This analysis spans the years 2015 to 2100, calculating time-dependent exceedance probabilities for each location and subsequently aggregating these to derive mean exceedance probability time series for every county. Utilizing Sen's slope estimator, we quantified the extent to which the exceedance probability for strong winds is projected to evolve annually in future decades across each county and hurricane category. Figure 11 illustrates the changes in the probability of experiencing Category 1 or higher hurricanes, as predicted by the simulated synthetic hurricanes from the six CMIP6 models. With the exception of lower values from the UKMO model, the findings predominantly indicate an upward trend in exceedance probability, especially within southern coastal and inland counties. Notably, the MPI-M model simulations show the steepest increase in the risk.

Beyond analyzing outputs from individual climate models, which elucidate the uncertainty inherent in different model projections, we aggregated these results to quantify the ensemble mean. This approach synthesizes the collective insights from the six CMIP6 climate models, providing a consolidated view of the anticipated changes in the risk of strong winds from Category 1 (or above) hurricanes. Figure 12 illustrates the ensemble mean changes in exceedance probability for Category 1 (or above) hurricanes on an annual basis throughout the forthcoming decades. This ensemble mean represents a comprehensive assessment of the risk evolution, factoring in the diverse perspectives offered by the multiple model simulations.

Consistent outcomes derived from individual climate models, as well as the ensemble mean, are given for the higher hurricane categories (2 - 5), as depicted in Figures 13 through 20. These results delineate the regions projected to be most susceptible to hurricane-induced damages in future years and decades. Furthermore, the analysis elucidates the anticipated evolution of the risk associated with hurricanes of varying categories within these identified vulnerable counties. Specifically, it quantifies the expected changes in frequency, intensity, and spatial distribution of hurricane impacts, thereby offering insights into the future dynamics of hurricane risk in these areas.

This methodology facilitates the determination of the annual rate of change in the likelihood of encountering hurricanes of different categories in the current and future decades at the county level. These rates can significantly contribute to quantifying the annual adjustments to insurance premiums by Homesite, reflecting the evolving risk landscape. Furthermore, this report presents the time series of these probabilities for each specific county, offering a detailed view of risk projections over time.

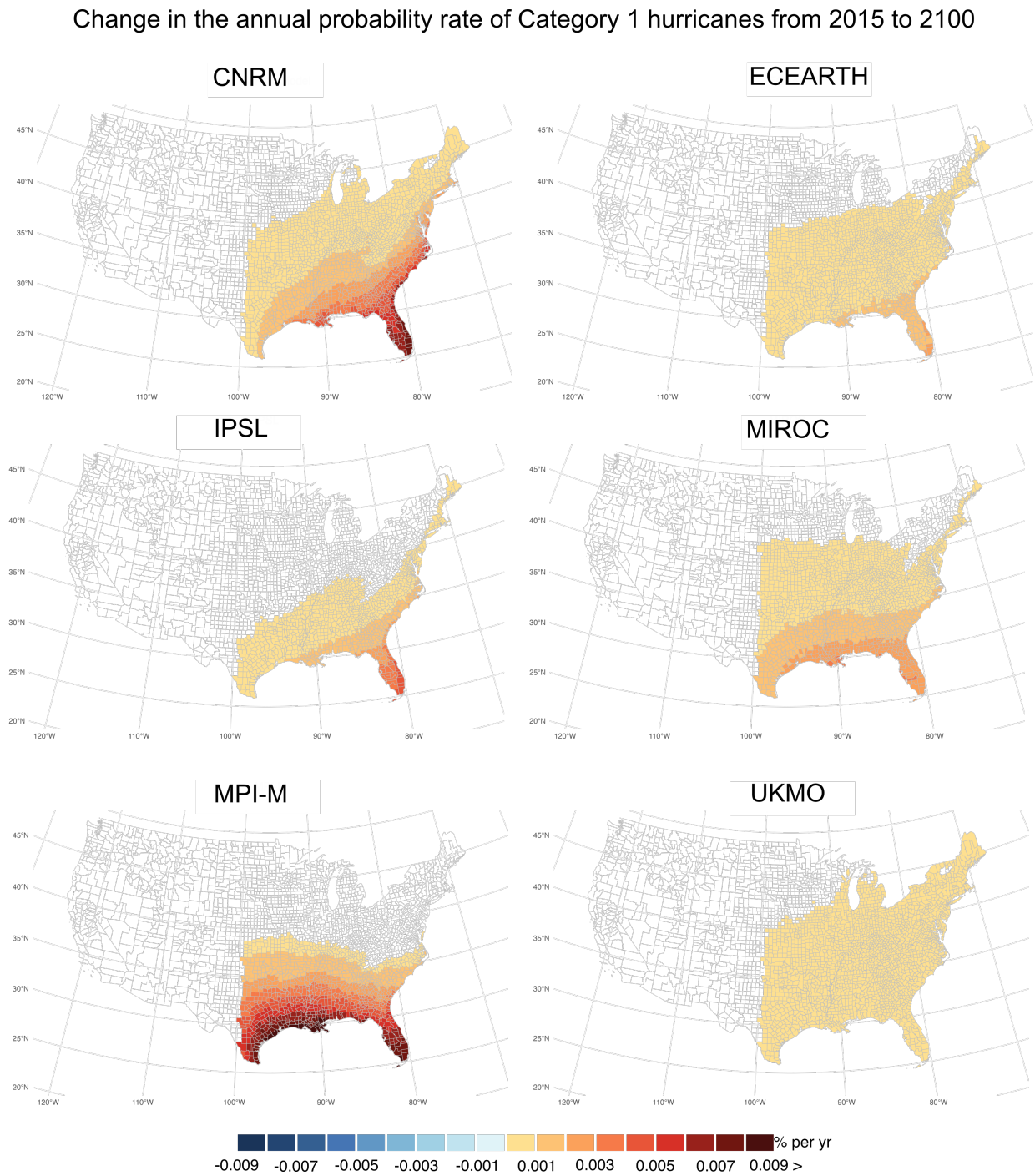

Figure 23: Changes in the annual probability rate (percentage per year) of hurricanes of category 1 or higher for each county from 2015 to 2100, based on six CMIP6 climate models using the SSP3-7.0 scenario. Note that these rates are calculated based on Sen's slope applied to averaged exceedance probability time series for each county from 2015 to 2100.

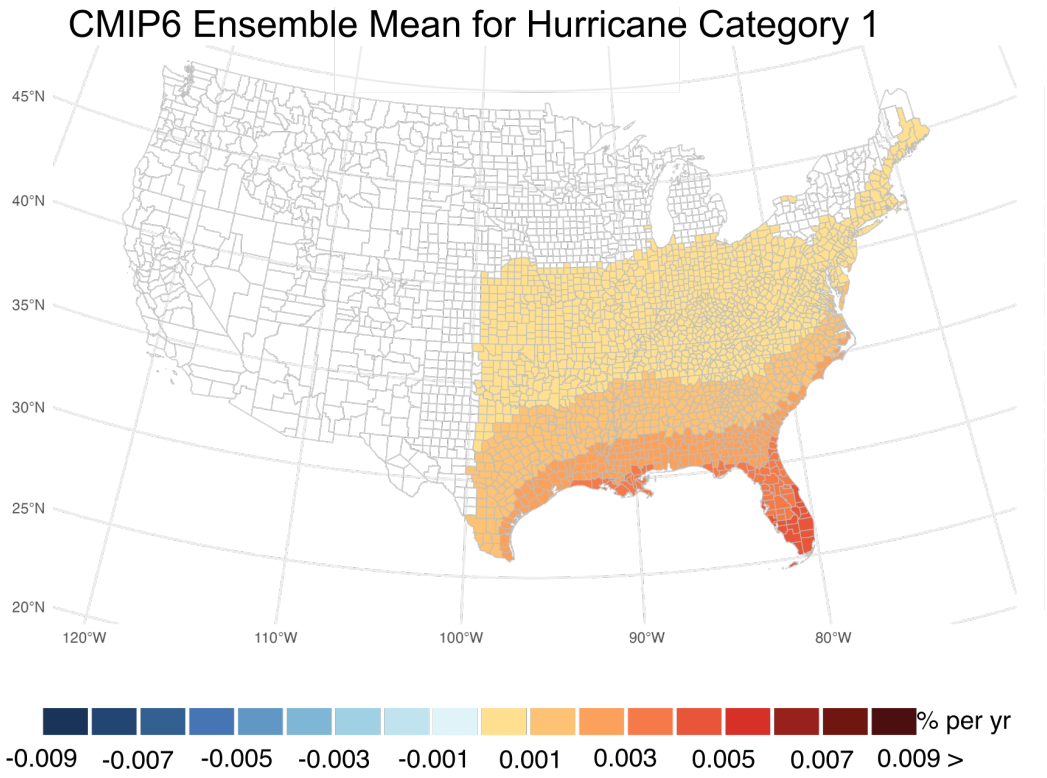

Figure 24: Changes in the annual probability rate (percentage per year) of hurricanes of category 1 or higher for each county from 2015 to 2100, based on the ensemble mean of six CMIP6 climate models using the SSP3-7.0 scenario.

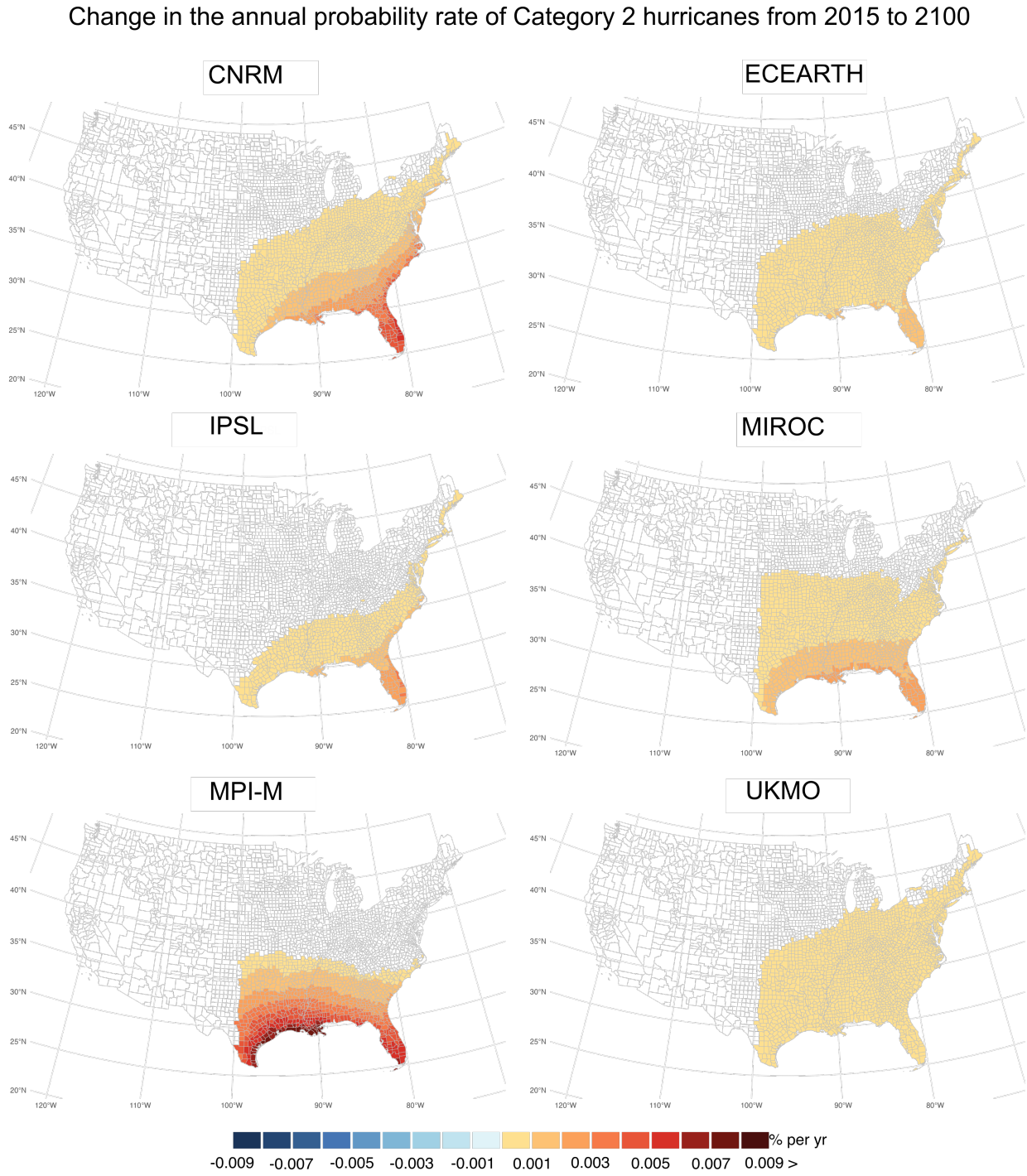

Figure 25: Similar to Figure 11, but for hurricanes of category 2 or higher

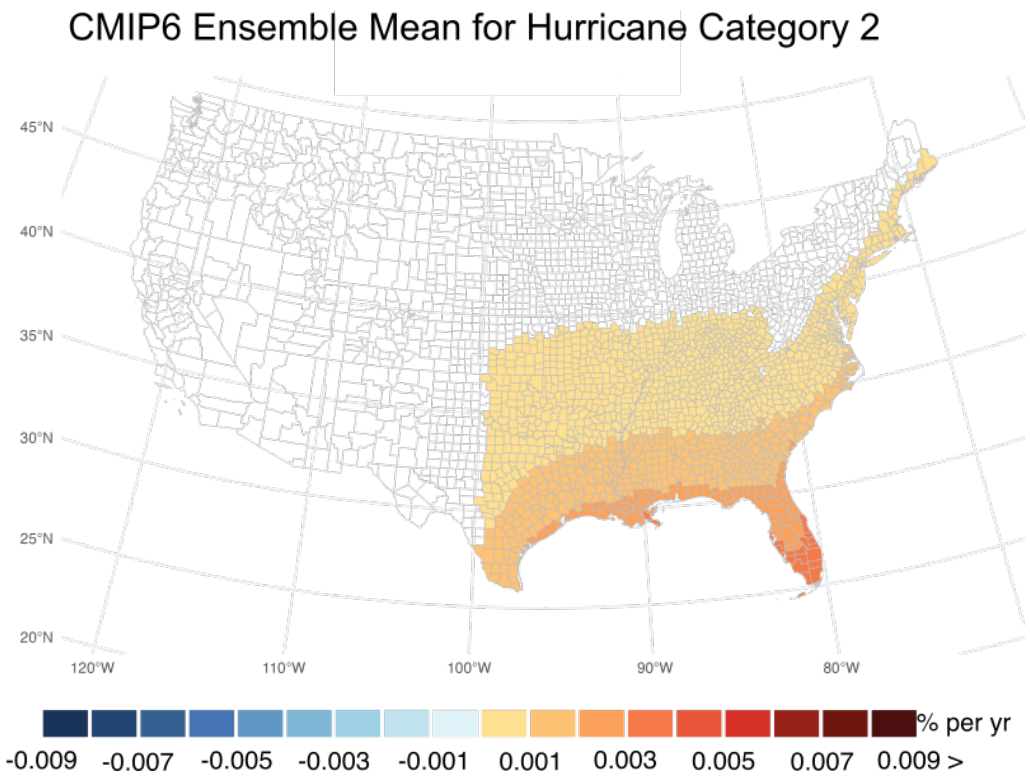

Figure 26: Similar to Figure 12, but for hurricanes of category 2 or higher

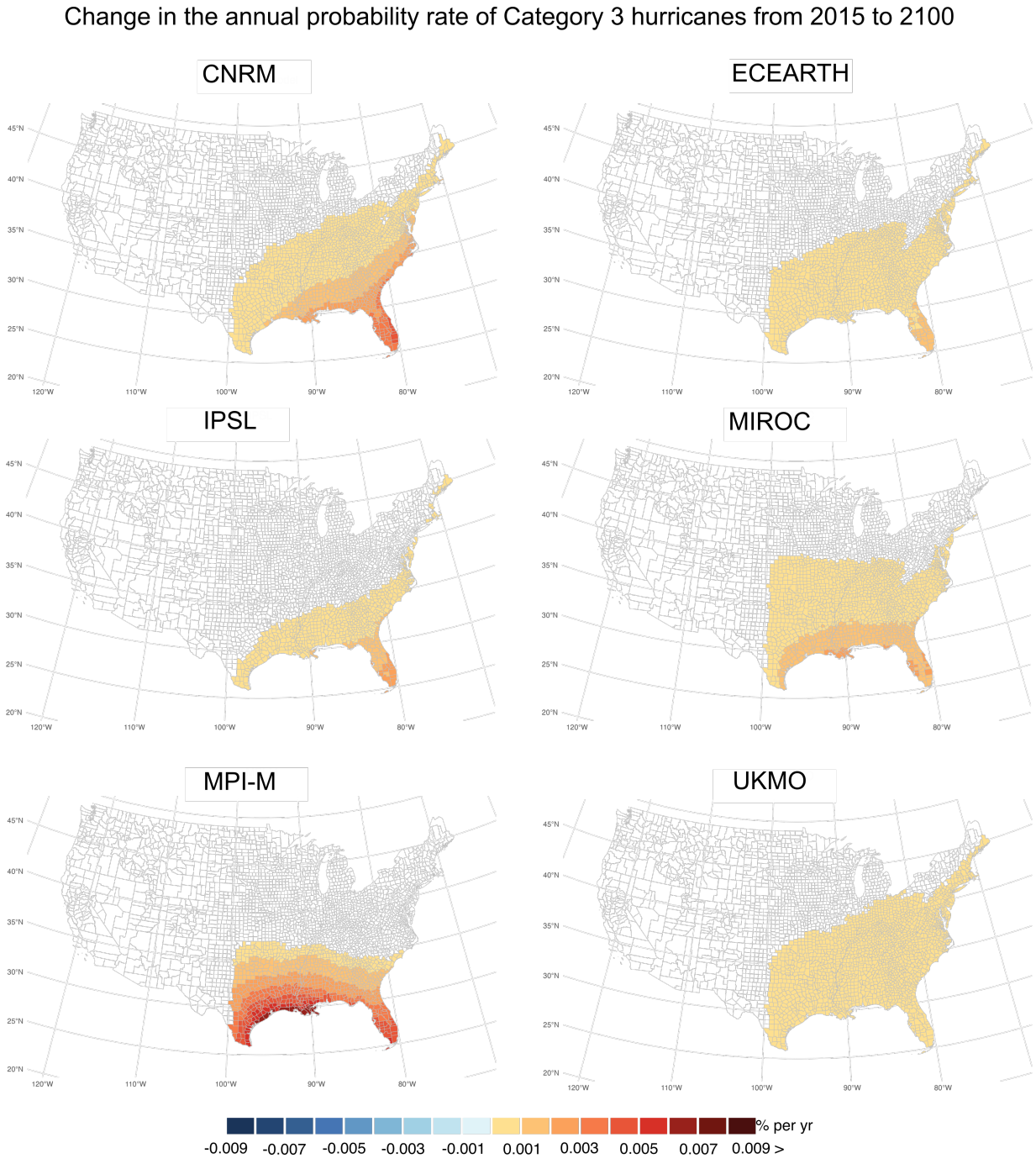

Figure 27: Similar to Figure 11, but for hurricanes of category 3 or higher

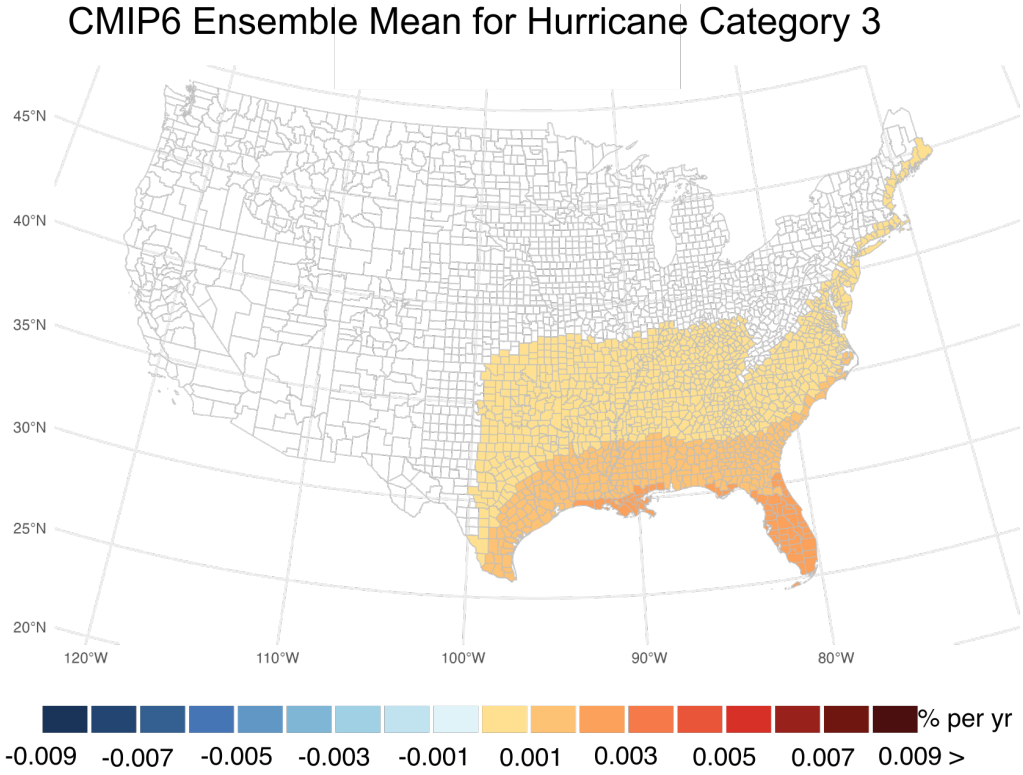

Figure 28: Similar to Figure 12, but for hurricanes of category 3 or higher

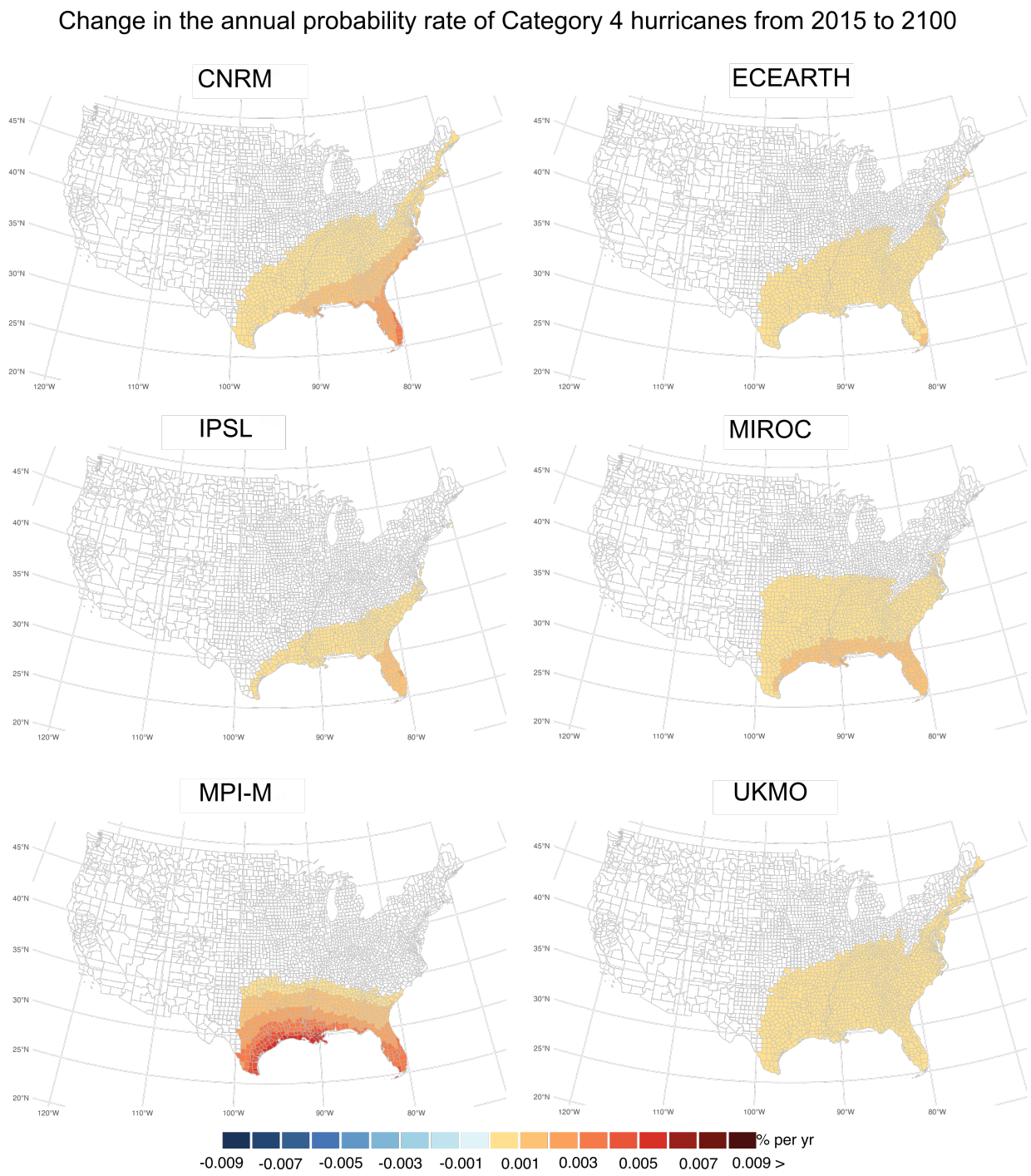

Figure 29: Similar to Figure 11, but for hurricanes of category 4 or higher

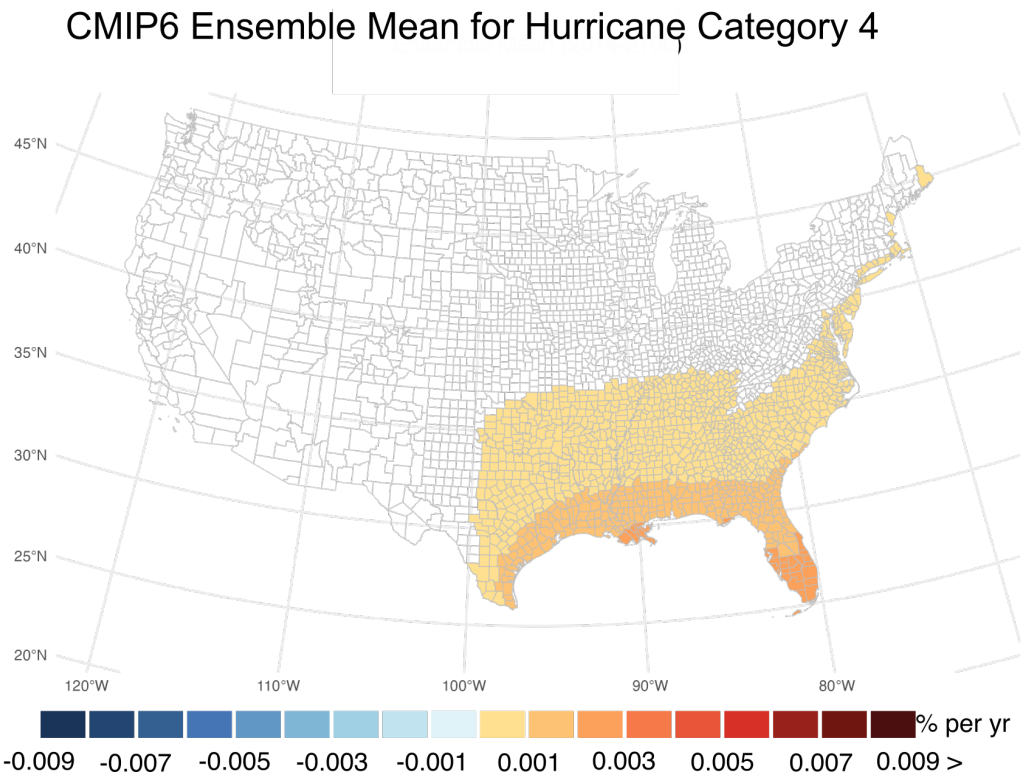

Figure 30: Similar to Figure 12, but for hurricanes of category 4 or higher

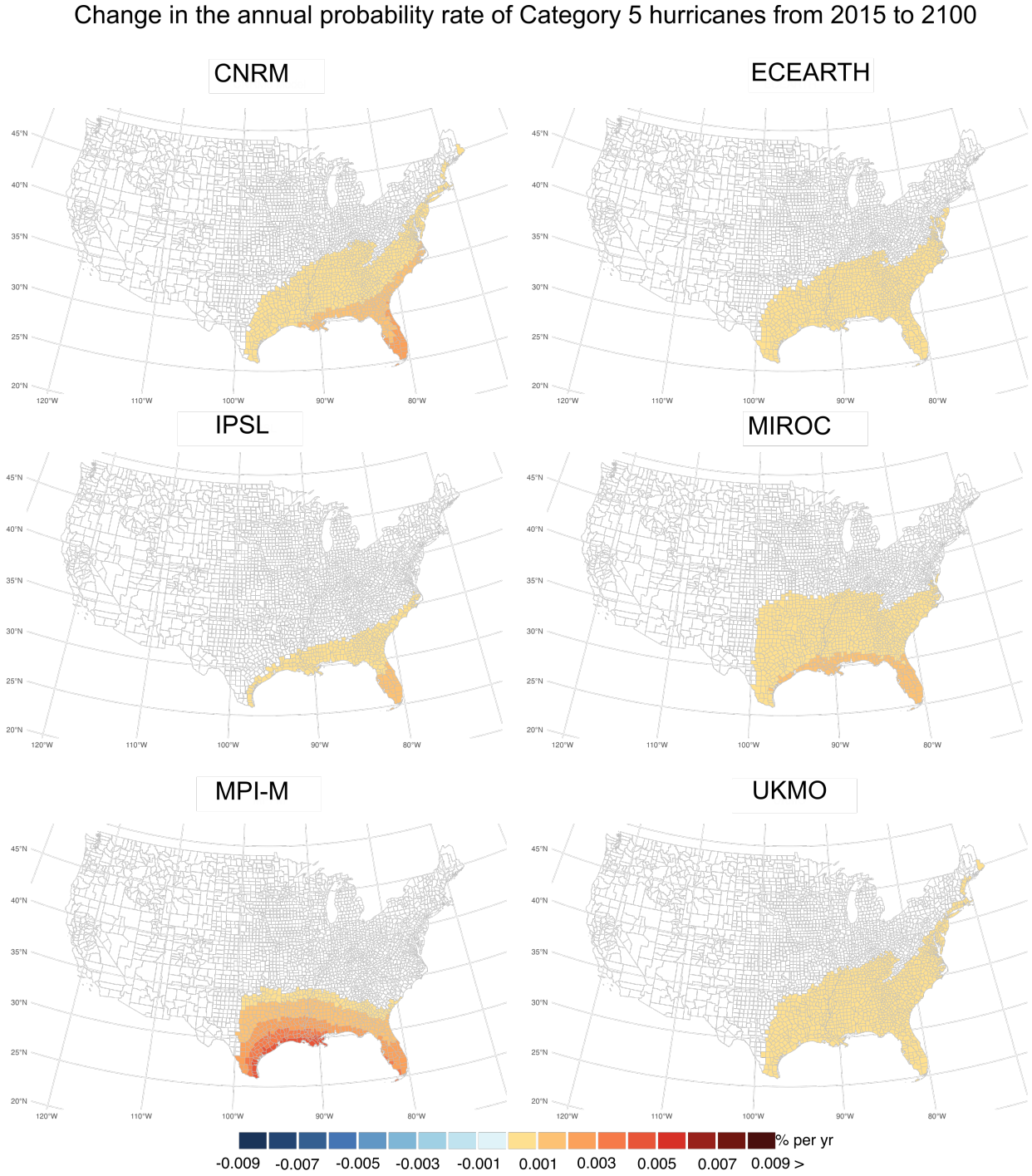

Figure 31: Similar to Figure 11, but for hurricanes of category 5 or higher

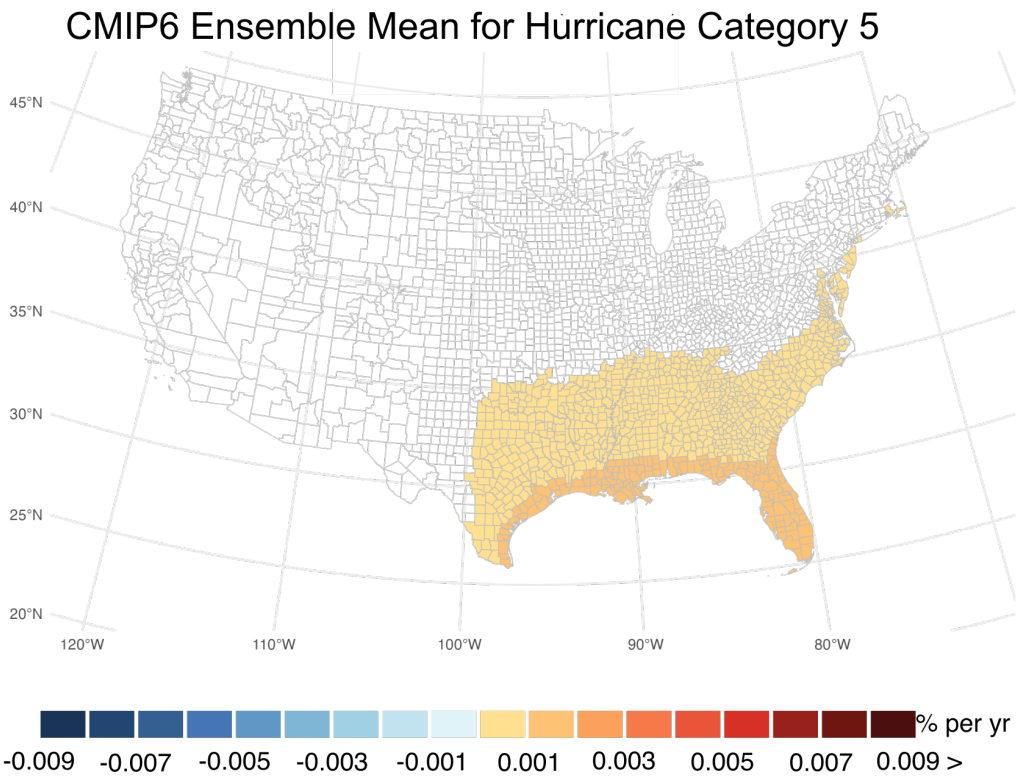

Figure 32: Similar to Figure 12, but for hurricanes of category 5 or higher

4 Conclusion

In this study, we employed a physics-based model to quantify the risk of strong winds across different hurricane categories in vulnerable regions of the U.S. for both current and future climates. Utilizing simulations of maximum wind speeds generated from a large set of synthetic hurricanes for each year in historical and current climates, we analyzed the reanalysis CERA-20C dataset, and projected future decades using multiple CMIP6 climate model simulations under the SSP3-7.0 scenario.

We developed a time-varying Bayesian risk assessment framework to quantify the extent to which the risk associated with maximum wind speeds of different categories has evolved over past decades and is expected to change in future decades at the county level within vulnerable states. Given the spatial and temporal dependencies observed in locations experiencing strong winds, we developed a sophisticated Bayesian spatio-temporal risk assessment model. This model accounts for these dependencies to quantify the time-varying exceedance probability that a storm with maximum wind of a specific category will occur in each county in both current and future decades.

Calculations of exceedance probabilities for different hurricane categories were performed for locations with a spatial resolution of 0.15 degrees (16 km) and aggregated at the county level for each year. The results span two time periods: historical (1901-2010) based on reanalysis data, and future projections (2015-2100) derived from the ensemble mean of six CMIP6 climate model simulations. These analyses identify counties most vulnerable to the risk of maximum wind speeds from different hurricane categories, both in the past/current climate and in future decades. Furthermore, rates of change in risk and return periods (frequency) were calculated and are available for each county for current and future decades.

These time-varying exceedance probability time series and rates of change serve as important factors in determining future insurance premiums for the Homesite Company, illustrating how the risk of different hurricane categories may evolve in a warming climate.

5 Data and code availability

All raw and processed data, including synthetic hurricane tracks and wind speeds, the outputs (exceedance probability time series), and rates of change in risk, as well as corresponding codes, are provided alongside this report to the Homesite Company.

6 Publications supported under this contract

Here is the list of publications supported for this research contract:

- Sarhadi, A., Rousseau-Rizzi, R., Mandli, K., Neal, J., Wiper, M. P., Feldmann, M., Emanuel, K. (2024). Climate change contributions to increasing compound flooding risk in New York City. **Bulletin of the American Meteorological Society**, 105(2), E337-E356. American Meteorological Society.

- Sarhadi, A., Rousseau-Rizzi, R., Emanuel, K. (2024). Physics-based risk assessment of compound flooding from tropical and extratropical cyclones in a warming climate. **Earth's Future**, under review.

- Sarhadi, A., Emanuel, K. (2024). Anthropogenic forcing and the intensifying spatio-temporal risks of major tropical cyclones in a nonstationary climate. **Proceedings of the National Academy of Sciences**, under preparation.

In addition, the results of this research were presented at different conferences. Here is the list of presentations:

- Ali Sarhadi, Kerry Emanuel, (2023), "Economic risk of intensifying compound hazards from Tropical Cyclones", *American Geophysical Union* , San Francisco.

- Sarhadi, A., Kerry Emanuel, 2022, "Climate change is increasing the risk of compound flooding by tropical cyclones in New York City", American Geophysical Union (AGU), Chicago.

- Sarhadi, A., Kerry Emanuel, 2022, "Future risk of compound flooding from Tropical Cyclones", Symposium on Hurricane Risk in a Changing Climate, Florida.

- Sarhadi, A., Kerry Emanuel, 2022, "Compound Flooding Risk from Tropical Cyclones Under A Warming Climate", American Meteorological Society (AMS) 102nd Annual Meeting, Houston, Texas.

- Sarhadi, A., Kerry Emanuel, 2021, "Tropical Cyclone Rainfall-driven Flooding Risk Under A Warming Climate", The AMS 34th Conference on Hurricanes and Tropical Meteorology Virtual Meeting.

- Sarhadi, A., Kerry Emanuel, 2021, "Inland Coastal Flooding Risk by Tropical Cyclone", European Geosciences Union (EGU) General Assembly, Vienna, Austria.

- Sarhadi, A., Kerry Emanuel, 2021, "Tropical Cyclone Rainfall-driven Flood Risk Assessment", NRC 6th Annual Probabilistic Flood Hazard Assessment Workshop.

References

Jeroen CJH Aerts, WJ Wouter Botzen, Kerry Emanuel, Ning Lin, Hans De Moel, and Erwann O Michel-Kerjan. Evaluating flood resilience strategies for coastal megacities. *Science*, 344(6183):473–475, 2014.

Laura A Bakkensen and Robert O Mendelsohn. Global tropical cyclone damages and fatalities under climate change: An updated assessment. *Hurricane risk*, pages 179–197, 2019.

Paul D Bates, Matthew S Horritt, and Timothy J Fewtrell. A simple inertial formulation of the shallow water equations for efficient two-dimensional flood inundation modelling. *Journal of Hydrology*, 387(1-2):33–45, 2010.

Paul D Bates, Niall Quinn, Christopher Sampson, Andrew Smith, Oliver Wing, Jeison Sosa, James Savage, Gaia Olcese, Jeff Neal, Guy Schumann, et al. Combined modeling of us fluvial, pluvial, and coastal flood hazard under current and future climates. *Water Resources Research*, 57(2):e2020WR028673, 2021.

Morris A Bender, Thomas R Knutson, Robert E Tuleya, Joseph J Sirutis, Gabriel A Vecchi, Stephen T Garner, and Isaac M Held. Modeled impact of anthropogenic warming on the frequency of intense atlantic hurricanes. *Science*, 327(5964):454–458, 2010.

Marsha J Berger, David L George, Randall J LeVeque, and Kyle T Mandli. The geoclaw software for depth-averaged flows with adaptive refinement. *Advances in Water Resources*, 34(9):1195–1206, 2011.

Luisa Bernardinelli, D Clayton, Cristiana Pascutto, Chiara Montomoli, Mauro Ghislandi, and Marco Songini. Bayesian analysis of space—time variation in disease risk. *Statistics in medicine*, 14(21-22):2433–2443, 1995.

Julian Besag, Jeremy York, and Annie Mollié. Bayesian image restoration, with two applications in spatial statistics. *Annals of the institute of statistical mathematics*, 43: 1–20, 1991.

Marta Blangiardo, Michela Cameletti, Gianluca Baio, and Håvard Rue. Spatial and spatio-temporal models with r-inla. *Spatial and spatio-temporal epidemiology*, 7:39–55, 2013.

James F Booth, Veeshan Narinesingh, Katherine L Towey, and Jeyavinoth Jeyaratnam. Storm surge, blocking, and cyclones: A compound hazards analysis for the northeast united states. *Journal of Applied Meteorology and Climatology*, 60(11):1531–1544, 2021.

Hamparsum Bozdogan. Model selection and akaike's information criterion (aic): The general theory and its analytical extensions. *Psychometrika*, 52(3):345–370, 1987.

Brian A Colle, Frank Buonaiuto, Malcolm J Bowman, Robert E Wilson, Roger Flood, Robert Hunter, Alexander Mintz, and Douglas Hill. New york city's vulnerability to coastal flooding: Storm surge modeling of past cyclones. *Bulletin of the American Meteorological Society*, 89(6):829–842, 2008.

Brian A Colle, James F Booth, and Edmund KM Chang. A review of historical and future changes of extratropical cyclones and associated impacts along the us east coast. *Current Climate Change Reports*, 1:125–143, 2015.

Dick P Dee, S M Uppala, Adrian J Simmons, Paul Berrisford, Paul Poli, Shinya Kobayashi, U Andrae, MA Balmaseda, G Balsamo, d P Bauer, et al. The era-interim reanalysis: Configuration and performance of the data assimilation system. *Quarterly Journal of the royal meteorological society*, 137(656):553–597, 2011.

Jon Dewitz. Us geological survey (2021). national land cover database (nlcd) 2019 products. *US Geological Survey data release*, 2021.

Kerry Emanuel. Increasing destructiveness of tropical cyclones over the past 30 years. *Nature*, 436(7051):686–688, 2005.

Kerry Emanuel. Global warming effects on us hurricane damage. *Weather, Climate, and Society*, 3(4):261–268, 2011.

Kerry Emanuel. Assessing the present and future probability of hurricane harvey's rainfall. *Proceedings of the National Academy of Sciences*, 114(48):12681–12684, 2017.

Kerry Emanuel. Atlantic tropical cyclones downscaled from climate reanalyses show increasing activity over past 150 years. *Nature communications*, 12(1):7027, 2021a.

Kerry Emanuel. Response of global tropical cyclone activity to increasing co 2: Results from downscaling cmip6 models. *Journal of Climate*, 34(1):57–70, 2021b.

Kerry Emanuel. Cyclone jasper's rains in the context of climate change. *Proceedings of the National Academy of Sciences*, 121(15):e2400292121, 2024.

Kerry Emanuel, Christopher DesAutels, Christopher Holloway, and Robert Korty. Environmental control of tropical cyclone intensity. *Journal of the atmospheric sciences*, 61(7):843–858, 2004.

Kerry Emanuel, Sai Ravela, Emmanuel Vivant, and Camille Risi. A statistical deterministic approach to hurricane risk assessment. *Bulletin of the American Meteorological Society*, 87(3):299–314, 2006.

Kerry Emanuel, Ragoth Sundararajan, and John Williams. Hurricanes and global warming: Results from downscaling ipcc ar4 simulations. *Bulletin of the American Meteorological Society*, 89(3):347–368, 2008.

Kerry A Emanuel. Downscaling cmip5 climate models shows increased tropical cyclone activity over the 21st century. *Proceedings of the National Academy of Sciences*, 110 (30):12219–12224, 2013.

Monika Feldmann, Kerry Emanuel, Laiyin Zhu, and Ulrike Lohmann. Estimation of atlantic tropical cyclone rainfall frequency in the united states. *Journal of Applied Meteorology and Climatology*, 58(8):1853–1866, 2019.

B Fox-Kemper, HT Hewitt, C Xiao, G Aalgeirsdóttir, SS Drijfhout, TL Edwards, NR Golledge, M Hemer, RE Kopp, G Krinner, et al. 2021: Ocean, cryosphere and sea level change.

Andra J Garner, Michael E Mann, Kerry A Emanuel, Robert E Kopp, Ning Lin, Richard B Alley, Benjamin P Horton, Robert M DeConto, Jeffrey P Donnelly, and David Pollard. Impact of climate change on new york city's coastal flood hazard: Increasing flood heights from the preindustrial to 2300 ce. *Proceedings of the National Academy of Sciences*, 114(45):11861–11866, 2017.

Avantika Gori and Ning Lin. Projecting compound flood hazard under climate change with physical models and joint probability methods. *Earth's Future*, 10(12): e2022EF003097, 2022.

Avantika Gori, Ning Lin, and James Smith. Assessing compound flooding from landfalling tropical cyclones on the north carolina coast. *Water Resources Research*, 56(4): e2019WR026788, 2020.

Avantika Gori, Ning Lin, Dazhi Xi, and Kerry Emanuel. Tropical cyclone climatology change greatly exacerbates us joint rainfall-surge hazard. 2021.

Avantika Gori, Ning Lin, Dazhi Xi, and Kerry Emanuel. Tropical cyclone climatology change greatly exacerbates us extreme rainfall–surge hazard. *Nature Climate Change*, 12(2):171–178, 2022.

Lukas Gudmundsson, John Bjørnar Bremnes, Jan Erik Haugen, and Torill Engen-Skaugen. Downscaling rcm precipitation to the station scale using statistical transformations–a comparison of methods. *Hydrology and Earth System Sciences*, 16 (9):3383–3390, 2012.

Ping Huang, I-I Lin, Chia Chou, and Rong-Hui Huang. Change in ocean subsurface environment to suppress tropical cyclone intensification under global warming. *Nature Communications*, 6(1):1–9, 2015.

Indraneel Kasmalkar, Dennis Wagenaar, Alina Bill-Weilandt, Jeanette Choong, Sonali Manimaran, Tian Ning Lim, Maricar Rabonza, and David Lallemant. Flow-tub model: A modified bathtub flood model with hydraulic connectivity and path-based attenuation. *MethodsX*, 12:102524, 2024.

Kenneth R Knapp, Michael C Kruk, David H Levinson, Howard J Diamond, and Charles J Neumann. The international best track archive for climate stewardship (ibtracs) unifying tropical cyclone data. *Bulletin of the American Meteorological Society*, 91(3):363–376, 2010.

Kenneth R Knapp, Howard J Diamond, James P Kossin, Michael C Kruk, Carl J Schreck, et al. International best track archive for climate stewardship (ibtracs) project, version 4. *NOAA National Centers for Environmental Information*, 10, 2018.

Leonhard Knorr-Held. Bayesian modelling of inseparable space-time variation in disease risk. *Statistics in medicine*, 19(17-18):2555–2567, 2000.

Muge Komurcu Bayraktar, Kerry Andrew Emanuel, M Huber, and RP Acosta. High-resolution climate projections for the northeastern united states using dynamical downscaling at convection-permitting scales. 2018.

James P Kossin. A global slowdown of tropical-cyclone translation speed. *Nature*, 558 (7708):104–107, 2018.

James P Kossin, Kerry A Emanuel, and Gabriel A Vecchi. The poleward migration of the location of tropical cyclone maximum intensity. *Nature*, 509(7500):349–352, 2014.

Scott A Kulp and Benjamin H Strauss. New elevation data triple estimates of global vulnerability to sea-level rise and coastal flooding. *Nature communications*, 10(1): 1–12, 2019.

Ning Lin, Kerry Emanuel, Michael Oppenheimer, and Erik Vanmarcke. Physically based assessment of hurricane surge threat under climate change. *Nature Climate Change*, 2 (6):462–467, 2012.

Ning Lin, Robert E Kopp, Benjamin P Horton, and Jeffrey P Donnelly. Hurricane sandy's flood frequency increasing from year 1800 to 2100. *Proceedings of the National Academy of Sciences*, 113(43):12071–12075, 2016.

Ning Lin, Reza Marsooli, and Brian A Colle. Storm surge return levels induced by mid-to-late-twenty-first-century extratropical cyclones in the northeastern united states. *Climatic change*, 154:143–158, 2019.

Christopher M Little, Radley M Horton, Robert E Kopp, Michael Oppenheimer, Gabriel A Vecchi, and Gabriele Villarini. Joint projections of us east coast sea level and storm surge. *Nature Climate Change*, 5(12):1114–1120, 2015.

Maofeng Liu, Gabriel A Vecchi, James A Smith, and Thomas R Knutson. Causes of large projected increases in hurricane precipitation rates with global warming. *npj Climate and Atmospheric Science*, 2(1):1–5, 2019.

Kyle T Mandli and Clint N Dawson. Adaptive mesh refinement for storm surge. *Ocean Modelling*, 75:36–50, 2014.

Reza Marsooli, Ning Lin, Kerry Emanuel, and Kairui Feng. Climate change exacerbates hurricane flood hazards along us atlantic and gulf coasts in spatially varying patterns. *Nature communications*, 10(1):1–9, 2019.

Simona Meiler, Thomas Vogt, Nadia Bloemendaal, Alessio Ciullo, Chia-Ying Lee, Suzana J Camargo, Kerry Emanuel, and David N Bresch. Intercomparison of regional loss estimates from global synthetic tropical cyclone models. *Nature Communications*, 13(1):6156, 2022.

Yuki Miura, Kyle T Mandli, and George Deodatis. High-speed gis-based simulation of storm surge–induced flooding accounting for sea level rise. *Natural Hazards Review*, 22 (3):04021018, 2021.

Hamed R Moftakhari, Gianfausto Salvadori, Amir AghaKouchak, Brett F Sanders, and Richard A Matthew. Compounding effects of sea level rise and fluvial flooding. *Proceedings of the National Academy of Sciences*, 114(37):9785–9790, 2017.

M Müller. Rapid change in semi-diurnal tides in the north atlantic since 1980. *Geophysical research letters*, 38(11), 2011.

Claudio Navacchi, Senmao Cao, Bernhard Bauer-Marschallinger, Paul Snoeij, David Small, and Wolfgang Wagner. Utilising sentinel-1's orbital stability for efficient pre-processing of sigma nought backscatter. *ISPRS Journal of Photogrammetry and Remote Sensing*, 192:130–141, 2022.

NCEI. Noaa next generation radar (nexrad) level 3 products. `https://www.ncei.noaa.gov/access/metadata/landing-page/bin/iso?id=gov.noaa.ncdc:C00708`, 2018. Accessed: 28 July 2018.

Jeffrey Neal, Guy Schumann, and Paul Bates. A subgrid channel model for simulating

river hydraulics and floodplain inundation over large and data sparse areas. *Water Resources Research*, 48(11), 2012.

Barbara Neumann, Athanasios T Vafeidis, Juliane Zimmermann, and Robert J Nicholls. Future coastal population growth and exposure to sea-level rise and coastal flooding-a global assessment. *PloS one*, 10(3):e0118571, 2015.

William D Nordhaus. The economics of hurricanes and implications of global warming. *Climate Change Economics*, 1(01):1–20, 2010.

Christina M Patricola and Michael F Wehner. Anthropogenic influences on major tropical cyclone events. *Nature*, 563(7731):339–346, 2018.

Roger A Pielke Jr. Future economic damage from tropical cyclones: sensitivities to societal and climate changes. *Philosophical Transactions of the Royal Society A: Mathematical, Physical and Engineering Sciences*, 365(1860):2717–2729, 2007.

Matthew DK Priestley and Jennifer L Catto. Future changes in the extratropical storm tracks and cyclone intensity, wind speed, and structure. *Weather and Climate Dynamics*, 3(1):337–360, 2022.

Edward N Rappaport. Fatalities in the united states from atlantic tropical cyclones: New data and interpretation. *Bulletin of the American Meteorological Society*, 95(3): 341–346, 2014.

Andra J Reed, Michael E Mann, Kerry A Emanuel, Ning Lin, Benjamin P Horton, Andrew C Kemp, and Jeffrey P Donnelly. Increased threat of tropical cyclones and coastal flooding to new york city during the anthropogenic era. *Proceedings of the National Academy of Sciences*, 112(41):12610–12615, 2015.

Keith J Roberts, Brian A Colle, and Nathan Korfe. Impact of simulated twenty-first-century changes in extratropical cyclones on coastal flooding at the battery, new york city. *Journal of Applied Meteorology and Climatology*, 56(2):415–432, 2017.

Ali Sarhadi, Raphaël Rousseau-Rizzi, Kyle Mandli, Jeffrey Neal, Michael P Wiper, Monika Feldmann, and Kerry Emanuel. Climate change contributions to increasing compound flooding risk in new york city. *Bulletin of the American Meteorological Society*, 2024.

Mark A Saunders and Adam S Lea. Large contribution of sea surface warming to recent increase in atlantic hurricane activity. *Nature*, 451(7178):557–560, 2008.

Christine C Shepard, Vera N Agostini, Ben Gilmer, Tashya Allen, Jeff Stone, William Brooks, and Michael W Beck. Assessing future risk: quantifying the effects of sea level rise on storm surge risk for the southern shores of long island, new york. *Natural hazards*, 60:727–745, 2012.

Adam B Smith et al. Us billion-dollar weather and climate disasters, 1980–present (ncei accession 0209268). *NOAA National Centers for Environmental Information*, 10, 2020.

Benjamin H Strauss, Philip M Orton, Klaus Bittermann, Maya K Buchanan, Daniel M Gilford, Robert E Kopp, Scott Kulp, Chris Massey, Hans de Moel, and Sergey Vinogradov. Economic damages from hurricane sandy attributable to sea level rise caused by anthropogenic climate change. *Nature communications*, 12(1):1–9, 2021.

Joshua Studholme, Alexey V Fedorov, Sergey K Gulev, Kerry Emanuel, and Kevin Hodges. Poleward expansion of tropical cyclone latitudes in warming climates. *Nature Geoscience*, 15(1):14–28, 2022.

Charles Sutton, Andrew McCallum, et al. An introduction to conditional random fields. *Foundations and Trends® in Machine Learning*, 4(4):267–373, 2012.

Kevin E Trenberth, Lijing Cheng, Peter Jacobs, Yongxin Zhang, and John Fasullo. Hurricane harvey links to ocean heat content and climate change adaptation. *Earth's Future*, 6(5):730–744, 2018.

Thomas Wahl, Shaleen Jain, Jens Bender, Steven D Meyers, and Mark E Luther. Increasing risk of compound flooding from storm surge and rainfall for major us cities. *Nature Climate Change*, 5(12):1093–1097, 2015.

Kevin JE Walsh, Suzana J Camargo, Gabriel A Vecchi, Anne Sophie Daloz, James Elsner, Kerry Emanuel, Michael Horn, Young-Kwon Lim, Malcolm Roberts, Christina Patricola, et al. Hurricanes and climate: The us clivar working group on hurricanes. *Bulletin of the American Meteorological Society*, 96(6):997–1017, 2015.

Charles C Watson Jr and Mark E Johnson. Hurricane loss estimation models: Opportunities for improving the state of the art. *Bulletin of the American Meteorological Society*, 85(11):1713–1726, 2004.

Michael F Wehner and James P Kossin. The growing inadequacy of an open-ended saffir–simpson hurricane wind scale in a warming world. *Proceedings of the National Academy of Sciences*, 121(7):e2308901121, 2024.

Joannes J Westerink, Richard A Luettich, Jesse C Feyen, John H Atkinson, Clint Dawson, Hugh J Roberts, Mark D Powell, Jason P Dunion, Ethan J Kubatko, and Hasan Pourtaheri. A basin-to channel-scale unstructured grid hurricane storm surge model applied to southern louisiana. *Monthly weather review*, 136(3):833–864, 2008.

Oliver EJ Wing, William Lehman, Paul D Bates, Christopher C Sampson, Niall Quinn, Andrew M Smith, Jeffrey C Neal, Jeremy R Porter, and Carolyn Kousky. Inequitable patterns of us flood risk in the anthropocene. *Nature Climate Change*, 12(2):156–162, 2022.

Dazhi Xi, Ning Lin, and James Smith. Evaluation of a physics-based tropical cyclone rainfall model for risk assessment. *Journal of Hydrometeorology*, 21(9):2197–2218, 2020.

Wei Zhang, Gabriele Villarini, Gabriel A Vecchi, and James A Smith. Urbanization exacerbated the rainfall and flooding caused by hurricane harvey in houston. *Nature*, 563(7731):384–388, 2018.

Ying Zhang and Mohammad Reza Najafi. Probabilistic numerical modeling of compound flooding caused by tropical storm matthew over a data-scarce coastal environment. *Water Resources Research*, 56(10):e2020WR028565, 2020.